CHALCOGENIDE MICRO AND NANOSTRUCTURES AND APPLICATIONS

A DISSERTATION
SUBMITTED TO THE DEPARTMENT OF PHYSICS
AND THE GRADUATE SCHOOL OF ENGINEERING AND SCIENCE
OF BILKENT UNIVERSITY
IN PARTIAL FULFILLMENT OF THE REQUIREMENTS
FOR THE DEGREE OF
DOCTOR OF PHILOSOPHY

By
Ozan Aktaş
August, 2014

I certify that I have read this thesis and that in my opinion it is fully adequate, in scope and in quality, as a thesis of the degree of Doctor of Philosophy.

…….

Prof. Dr. Mehmet Bayındır (Advisor)

I certify that I have read this thesis and that in my opinion it is fully adequate, in scope and in quality, as a thesis of the degree of Doctor of Philosophy.

…….

Assoc. Prof. Dr. Ceyhun Bulutay

I certify that I have read this thesis and that in my opinion it is fully adequate, in scope and in quality, as a thesis of the degree of Doctor of Philosophy.

…….

Assoc. Prof. Dr. Selçuk Aktürk

I certify that I have read this thesis and that in my opinion it is fully adequate, in scope and in quality, as a thesis of the degree of Doctor of Philosophy.

…….

Assist. Prof. Dr. Ali Kemal Okyay

I certify that I have read this thesis and that in my opinion it is fully adequate, in scope and in quality, as a thesis of the degree of Doctor of Philosophy.

…….

Assist. Prof. Dr. Aykutlu Dana

Approved for the Graduate School of Engineering and Science:

…….

Prof. Dr. Levent Onural

Director of the Graduate School

ABSTRACT

CHALCOGENIDE MICRO AND NANOSTRUCTURES AND APPLICATIONS

Ozan Aktaş
Ph.D. in Physics
Supervisor: Prof. Dr. Mehmet Bayındır
August, 2014

Chalcogenides, which are glasses consist of S, Se and Te elements, are promising materials for photonics as silicon for modern electronics, due to their extraordinary material properties such as high nonlinearity and wide mid-IR transparency. However, the biggest barrier before their full extend technological exploitation is the difficulty in utilization of these unique material properties within photonic devices with various forms of desired geometries including nanowires, microspheres, and microdisks as necessitated by unique optical functionalities for specific applications, some of which are optical microresonators, modulators, and photodetection devices.

In this study, the author explore new routes for the fabrication of on-chip photonic elements with chalcogenides and consider a low cost high-yield production method with a compatible and extendable integration phase. The study illustrates production of chalcogenide optical cavities embedded in a polymer fiber, on-chip integration of the cavities having spherical, spheroidal, and ellipsoidal boundaries, and results of their optical characterizations. Besides the fabrication of active photonic devices with electro-optical capabilities, tapered chalcogenide fibers are also considered as evanescent couplers for the resonators of high index materials.

In addition, a large area chalcogenide nanowire based photodetection device is demonstrated including fabrication of photoconductive pixels, design of an electronic readout circuit, development of a custom software for a pattern detection application.

Keywords: Chalcogenides glasses, nanowires, optical microresonators, asymmetric resonant cavities, electro-optical Kerr effect, modulators, whispering gallery mode resonators, photonics, fiber drawing.

ÖZET

KALKOJEN MİKRO VE NANOYAPILAR VE UYGULAMALARI

Ozan Aktaş

Fizik, Doktora

Tez Yöneticisi: Prof. Dr. Mehmet Bayındır

Ağustos, 2014

S, Se ve Te elementlerinin bileşiminde yer aldığı camlardan olan kalkojenler, yüksek doğrusal olmayan kırılma indisleri ve geniş orta-enfraruj geçirgenliği gibi sıra dışı malzeme özellikleri sayesinde, silikonun modern elektronikte oynadığı rol gibi fotonik için gelecek vadeden malzemelerdir. Fakat ileri teknolojik kullanımlarının önündeki en büyük engel, bu malzeme özelliklerinin fotonik aygıtlarda mikrotel, mikroküre veya mikrodisk gibi özel uygulamalar için eşsiz optik işlevselliklerin gerektirdiği biçimlerde kullanılmasındaki zorluklardır. Optik resonatörler, modülatörler ve ışık algılama aygıtları bu uygulamaların bazılarıdır.

Bu çalışmada, yazar kalkojen tabanlı bütünleşmiş fotonik elemanların üretimi konusunda yeni yollar arayışındadır ve bu yolda diğer teknolojiler ile uyumlu ve genişletilebilir bütünleşme aşamaları olan düşük maliyetli çok verimli bir üretim yöntemini ele almaktadır. Çalışma, kalkojen optik kavitelerin bir polimer fiber içerisinde üretimlerinden devre üzerine küresel, küremsi ve elipsoidal şekillerde bütünleştirilmesine ve optik özelliklerin değerlendirilmesi kadar yapılanları göstermektedir. Elektro-optiksel özellikleri olan aktif fotonik elemanların üretiminin yanında bir de yüksek kırılma katsayılı resonatörlere ışık eşlemek için inceltilmiş kalkojen fiberlerin üretilmesini ele almaktadır.

Bunlara ilaveten, geniş alanlı kalkojen nano tel tabanlı bir ışık algılama aygıtının gösterimi yapılmıştır. Bu gösterim fotoiletken algılama hücrelerinin fabrikasyonunu, okuyucu elektronik devre tasarımını ve bir şekil algılama uygulaması için geliştirilen özel amaçlı yazılımı içermektedir.

Anahtar kelimeler: Kalkojen camlar, nanoteller, optik çınlaçlar, asimetrik kaviteler, elektro-optik etki, modülatörler, fısıldayan galeri modları, fotonik, fiber çekimi.

Acknowledgement

First and foremost I would like to thank my academic advisor, Prof. Mehmet Bayındır, not only for the support and guidance he has provided me throughout my dissertation, but also for motivation and understanding he provided during the course of my Ph.D., enabling me to fulfill my full potential in succeeding this thesis. I always admire him and see him as an idol for an academic career.

I would like to thank, in particular, my team mates Erol Özgür, Ersin Hüseyinoğlu, and Pelin Toren not only for their technical support but also kind friendship. We together overcame too many difficulties regarding technical or scientific problems we faced. I am very lucky to have friends like them in my life time. Without them nothing would be as enjoyable as it is.

I also particularly thank another dear friend, Mehmet Kanık. I enjoyed sleepless nights we spent in lab and his cheerful conversations.

I like to study with smart and dedicated people. Being a member of Bayındır Research Group gave me that chance with an unforgivable experience, thanks to the Bayındır Research Group members. I want to express my gratitudes to: Adem Yıldırım, Bihter Dağlar, Emre Öztürk, Muhammad Yunusa, Tamer Doğan, Urandelger Tuvshindorj, Tural Khudiyev, Bekir Turedi, Pınar Beyazkılıc, Girayhan Say, Gökçen Birlik Demirel, Osama Tobail, Mostafa M. El-Ashry, İbrahim Yılmaz, Emel Gürbüz, Murat Dere, Dilara Oksüz, Hale Nur Çoloğlu, Seyit Ali Yaşar, and Nese Özgür. And also, I would like to thank all faculty members, students and engineers of UNAM-National Nanotechnology Research Center, where I feel like to be a part of a family.

And of course, I would like to thank my mother, father and little sister. Without their constant support and patience in my depressed times, nothing would be possible.

I would like to express my gratitude to The Scientific and Technological Research Council of Turkey, TUBİTAK, for the Ph.D. Scholarship I have benefited throughout my Ph.D.

"Knowing is not enough; we must apply.
Willing is not enough; we must do."

J. W. von Goethe

Contents

List of Figures

List of Tables

Chapter 1

Introduction

1.1. The Promise of Chalcogenides

Silicon is the workhorse of the electronics industry which have amazingly transformed the life we live in. Thanks to this special material, today our global world is more connected than ever after the advent of the internet, cell phones, and relevant electronic applications. However, ever increasing needs to store, manipulate and transfer enormous amount of daily produced data, demands new solutions that can overcome the fundamental limitations of silicon and electronics. Solutions generally require a paradigm shift in the selection of materials and methodologies for handling information. Theoretically, chalcogenides are promising materials possessing the potential to fulfill all the needs and requirements due to their unique material properties, and photonics with integrated chalcogenide elements capable of electro-optical and all-optical effects at same time is expected to transform the future the way electronics did.

Chalcogenides, which are amorphous semiconductors containing chalcogen elements of Se, S, and Te, have already been exploited in various applications including solar cells [1], sensors [2], electronics [3], and photonics [4]. Optical data storage based on chalcogenides have been very beneficial in memory applications [5], and recently, chalcogenide phase change memory technology [6] have been attracted huge interest for the fabrication of the ideal memory of the future, which is ultrafast, nonvolatile, scalable, low cost, and has very low power operation and long life cycle.

Inherent high bandwidth of the light is the key factor enabling transfer of data at high rates as utilized in optical communications, however light signal needs to be

modulated to carry meaningful information. Photonic integrated circuits (PIC) can modulate light at data rates well beyond the capability of electronics (> 1 Tb/s) using all optical means [7, 8] which can benefit from optical properties of chalcogenides such as ultra-fast high Kerr nonlinearity, low two photon absorption and wide IR transparency [9]. Combining all-optical and electro-optical properties in resonant cavities can be the ultimate solution for ever increasing needs of communication, and interfacing with electronics can be obtained without causing any bottlenecks.

In addition, chalcogenides have been used as host media for laser applications since they have low phonon energy and can be doped by rare earth elements [10]. Nonlinear optical applications have also exploited chalcogenides in applications such as generation of supercontinuum [11] and Raman lasing [12].

Developing new methods for material synthesis and harnessing this special material properties in the form of specific geometries such as nanowires and microwires for fabrication of phase change memories and photodetectors, and microsphere and microdisks for photonic applications, are the current field of intense research still waiting some answers for the problems hindering ultimate utilizations of chalcogenides.

This thesis is devoted to developing new strategies and concepts enabling chalcogenides to be utilized in novel photonic applications. Starting with chalcogenide fiber drawing for the production of micro and nano structures, we used chalcogenide fibers as a versatile media to produce functional structures in different forms including wires, spheres, spheroids, ellipsoids, disks and tapers for photonic applications.

Chalcogenide nanowires were produced by a new fabrication method we recently reported. Integration of selenium fibers on a very large scale electrical circuits was achieved, and nanowire based photodetection device was demonstrated as an application.

Chalcogenide resonators have been drawn an increasing interest for nonlinear optical applications. However, duality between production and integration phase of these resonators have been hold back the applications so far. What resolved in this thesis is finding a way out of this dilemma, hence paving the way for a myriad applications for photonics. Chalcogenides have been generally used for their all optical properties in photonic applications, but their quadratic electro-optical properties is somehow ignored up to now. Therefore, we also focus on building electro-optical resonator based chalcogenide photonic devices in this thesis.

There have been an enormous need for high index evanescent couplers to couple light efficiently into high index material resonators. Although recent studies have made some progress for the fabrication of tapers from high index fibers, still some problems are waiting to be addressed such as splicing to silica fibers or mechanical instabilities. We believe that we have resolved all these issues after developing an approach for the fabrication and interfacing of the chalcogenide fibers.

1.2. Thesis Outline

The contents of this thesis are organized in a historical sequence, which was followed by the author during lifetime of this research adventure. Contents of individual chapters are given and any collaboration with other members of Bayıdır Group is stated explicitly.

Chapter 2 is an introductory chapter giving information about chalcogenides, basic methodology used in the material synthesis, fundamentals of fiber drawing, and importance of iterative size reduction technique as a new nanotechnology tool for the fabrication of nano and microstructures.

Chapter 3 demonstrates design and application of a device, which is the first of its kind, a large are nanowire based photodetection circuitry. Production of selenium fibers using iterative size reduction technique were done by Mehmet Kanık and Dr. Mecit Yaman. Integration of nanowires and optical characterizations were done in collaboration with Erol Özgür.

Chapter 4 gives a theoretical background for Whispering Gallery Modes resonators. Simulations results illustrate WGMs in sphere microcavities.

Chapter 5 gives theoretical background for evanescent coupling to optical resonators, and information about fabrication of tapered fiber couplers. Experimental setup used for optical measurements are also presented to give a complete picture for optical coupling and characterization of the resonators before the subject is mentioned in relevant chapters.

Chapter 6 explains a new method developed for the production and integration of chalcogenides cavities, which is expected to give a momentum in this field. Optical, material and surface characterizations of the produced cavities are also considered. COMSOL simulations of in-fiber microsphere formation based on Plateau-Rayleigh instability were done in collaboration with Dr. Osama Tobail.

Chapter 7 shows a new direction for the production of active chalcogenide cavities with emphasis on their electro-optical capabilities. A FEM based simulation of WGMs in an electro-optic cavity is illustrated, and production steps towards realization of on-chip active chalcogenide disk cavities are discussed with ups and downs of experimental approach.

Chapter 8 discusses three different approaches for the tapering of chalcogenides, and finally represents an ideal solution to the problem, which is of paramount importance for the achievement of efficient optical coupling into cavities of high index material.

Chapter 9 summarizes what have been done through the thesis and gives a quick glimpse for future directions.

Appendix A gives MATLAB codes used for some calculations and simulations used in Chapter 4 and Chapter 5.

Chapter 2

Fiber Drawing As a Method for Fabricating Chalcogenide Nano and Microstructures

2.1. Chalcogenide Glasses

Chalcogenide glasses (ChGs) are important amorphous semiconductors containing at least one of chalcogen elements (sulphur, selenium and tellurium) from group 6A of periodic table, which are covalently bonded to glass formers such as As, Ge, Ga, and P. Due to the large composition space enabling optimization of material properties as demanded by specific applications, chalcogenide have been utilized in a broad range of technology and research areas such as photonics [4], phase change memory [6] and sensors [2].

ChGs have low phonon energies due to the covalently bonded heavy atoms with low vibrational energies, making them good hosts for rare earth dopants such as Nd^{3+} and Er^{3+} [10]. Therefore, they have lower softening temperatures and hardness, and higher thermal expansion coefficients [13]. However, their long wavelength cut-off lies in the mid-IR region [14], making their transparency in the range of 1.5-20 μm as shown in Figure 2.1. In addition, they have high refractive indices (n = 2.2-3.4) and nonlinear refractive indices n_2 two or three orders of magnitude higher than that of silica. Superior optical and material properties of chalcogenides have been extensively used for ultrafast all-optical applications [15, 16] in fiber form [17] or as integrated waveguides in photonic circuits [18].

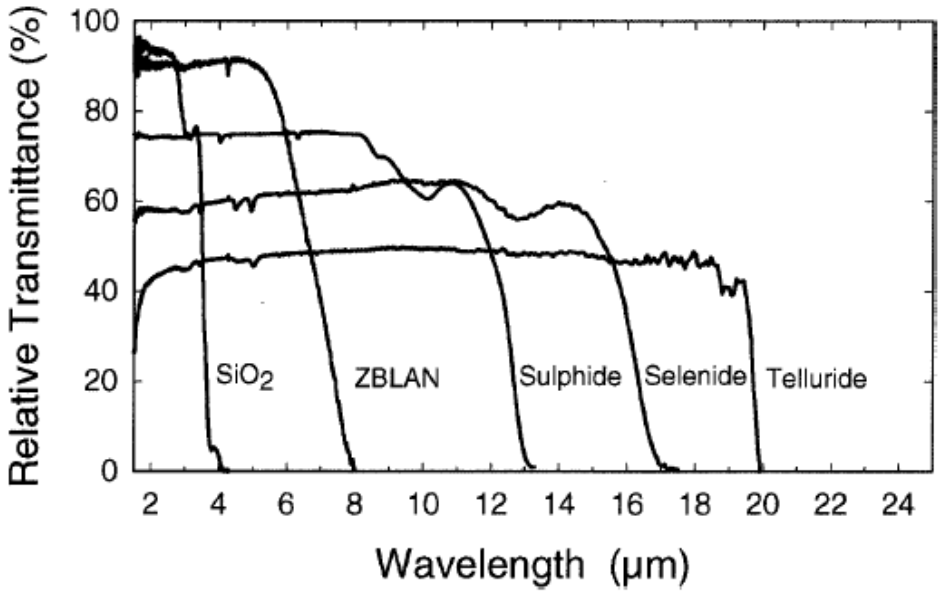

Figure 2.1: Infrared transmission spectra for various materials including ChGs [14].

Chalcogenide glasses can be deposited on substrates [19] by thermal evaporation, sputtering or wet spin deposition in order to make waveguides and resonators, which are building blocks of photonics circuits. However, all these methods require post-process anneal to obtain bulk glass like properties due to the changes in material stoichiometry during the process. More recently ultra-fast pulse laser deposition has been reported to circumvent these problems [20].

Fiber drawing of chalcogenides with other materials is also possible [21] by harnessing the rheological properties of these materials such as thermo-mechanical compatibility with high temperature engineered polymers, and their resistance to crystallization. Chalcogenide fibers have been used in a myriad applications [14] , which are nonlinear fiber optic amplifiers, laser power delivery, chemical sensing, imaging, etc. Recently fiber drawing has drawn attention and exploited in a ”stack and draw” fashion to produce micro-structured chalcogenide glass holey fibers [22], and chalcogenide micro and nanowires [23]. Fiber drawing as a method for fabricating chalcogenide nano and microstructures for photonics, phase change memory, and sensors will be an indispensable tool for science and technology in the future.

2.2. Glass Synthesis

Chalcogenide glasses synthesized in this thesis are Se, As_2Se_3 and As_2S_3. Selenium is used due to its photoconductive property for the fabrication of a photodetection device based on nanowires. As_2Se_3 and As_2S_3 are used in optics and photonics due to their superior optical properties such as high nonlinearity, wide IR transparency, and etc. For all materials, starting form is a rod of chalcogenide glass which is used as a preform for thermal fiber drawing. Glass synthesis steps are given basically for As_2Se_3.

The amorphous As_2Se_3 rod used in fiber drawing is prepared from high purity As and Se elements (Sigma Aldrich) using sealed-ampule melt-quenching technique [24]. The glove box stored (see Figure 2.2(a)) pure elements of materials As (wt% 40) and Se (wt% 60) are placed into a quartz tube under nitrogen atmosphere. In order to remove surface oxides and impurities, the tube is heated above 300 ºC under vacuum condition (see Figure 2.2(b)). After the tube is cooled down to room temperature, it is sealed under ~10^{-3} Torr vacuum. The sealed tube is placed in a rocking oven (see Figure 2.2(c)) and heated up to 800 ºC at a rate of 2 ºC. min^{-1}. After the oven is held at this temperature at vertical position for 24 hours, it is rocked at least for 6 hours to increase homogeneity. Subsequently, oven is cooled down to 600 ºC and the tube is quenched in water to form As_2Se_3 intermetallic glass rod with 10 cm length and 6 mm diameter.

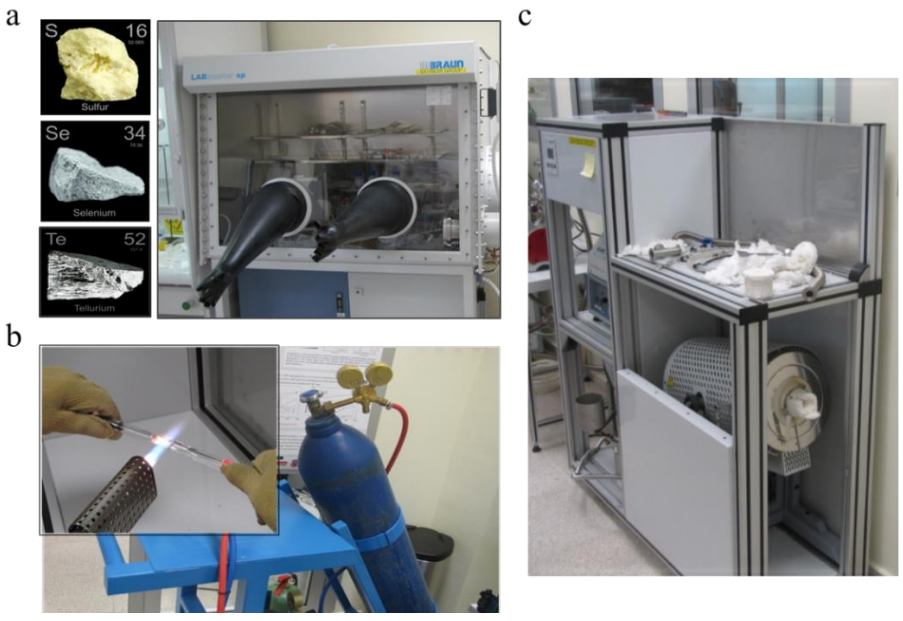

Figure 2.2: Chalcogenide glass synthesis. Process consists of three steps (a) material selection, (b) material purification and sealing, (c) rocking and homogenization.

2.3. Thermal Fiber Drawing

Fiber drawing process has two stages: fabrication of the initial preform structure and production of fibers by thermal drawing of the preform under high stress and temperature. As shown in Figure 2.3(a), a preform structure with 6 mm core diameter and 30 mm cladding diameter, which is actually an exact macroscopic copy of the fiber, is prepared by rolling 100 µm thick polyethersulfone (PES) films around an As_2Se_3 rod. Before consolidation process, the preform is held under 2×10^{-2} Torr vacuum at 180 ºC for 4 hours in order to evacuate trapped air between polymer layers. Then, rolled films are consolidated in a vacuum oven at 252 ºC for 30 minutes under 2×10^{-2} Torr vacuum. Fiber drawing process is executed in a custom made fiber tower which consists of a preform feeding mechanism, preform position alignment stage, furnace, optical thickness measurement system, tension measurement and a capstan. See Figure 2.3(b) for actual setup. Approximately 3 MPa tensile stress is applied to the preform during heating of the preform up to 300 ºC above glass transition temperature of As_2Se_3 and PES. Picture of the produced As_2Se_3 core PES cladding fibers are given in Figure 2.3(c). Volume reduction of the preform determines the final diameter of fiber, and is controlled by the tensile force and the furnace temperature.

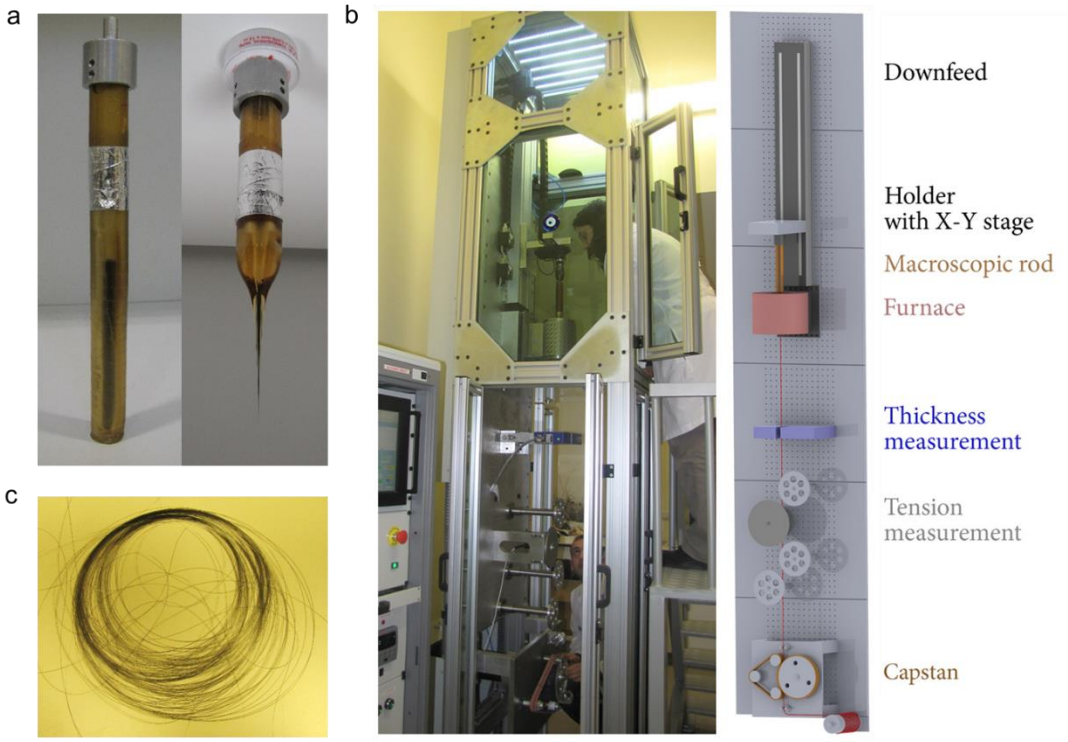

Figure 2.3: (a) Optical picture of a preform before and after thermal drawing. (b) Fiber tapering tower and basic components. (c) Chalcogenide core PES cladding fibers produced by thermal drawing.

2.4. Iterative Size Reduction Technique

We recently reported a new top-to-bottom nanotechnology fabrication method called iterative size reduction (ISR) method [23] to obtain polymer encapsulated globally oriented ultra-long micro and nanowires made of various materials ranging from polymers and semiconductors to metals, with improved piezoelectric, phase change, and photoconductive material properties. In this study, selenium nanowires, which are used as photoconductive elements in the pixel formation of a photodetection device [25] (see Chapter 3), are produced using ISR technique. For the production of As_2Se_3 single core polymer cladding fibers of different diameters and core-cladding ratios, only first two steps of ISR technique are followed with single fiber in every step. Post-fabrication thermal treatments to chalcogenide fibers are conducted to obtain different morphologies from single core micro fibers [26, 27].

ISR technique is basically stacking and redrawing of produced fibers in each successive steps as shown schematically in Figure 2.4. Nanowire array production from a macroscopic rod by iterative thermal size reduction starts with Step 1: A macroscopic cylindrical rod (diameter 10 mm, length 200 mm) is fabricated from a chalcogenide material that is to be transformed into micro and nanostructures. A thermo-mechanically suitable polymer sheet (PES) is tightly rolled around the rod until the final diameter is 30 mm. The multimaterial structure is then thermally consolidated under vacuum above the glass transition temperatures of both materials, in order to fuse the polymer sheets and the chalcogenide rod to obtain a preform. Finally the preform is drawn into a fiber to obtain hundreds of meters of polymer encapsulated chalcogenide microwires. Step 2: After stacking previously produced fibers of desired number, diameter and length, a polymer cladding is rolled around the stacked fibers, and consolidated. Second step drawing results in submicron wire arrays in a polymer fiber. Step 3: The same procedure, as followed in the second Step is applied again one more time to obtain hierarchically positioned arrays of smaller diameter nanowires. Chalcogenide nanowires produced by ISR method can be seen in Figure 2.5.

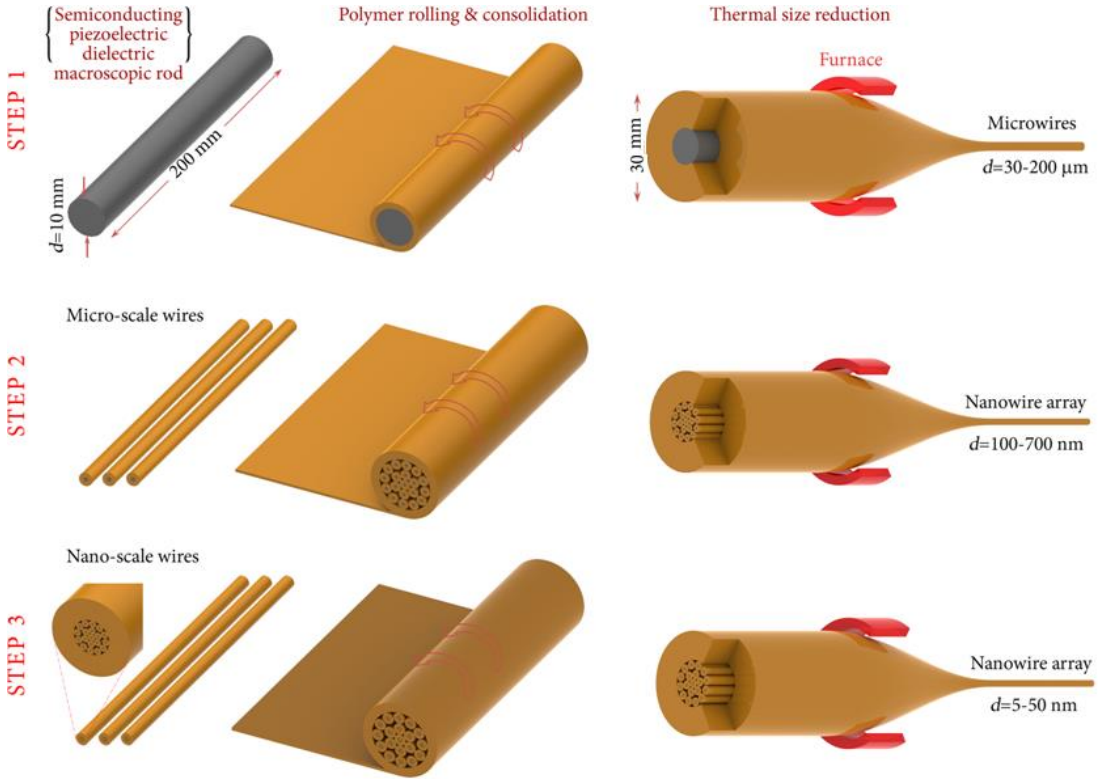

Figure 2.4: Steps of iterative size reduction technique resulting into one dimensional micro and nano-structures encapsulated by a polymer jacket.

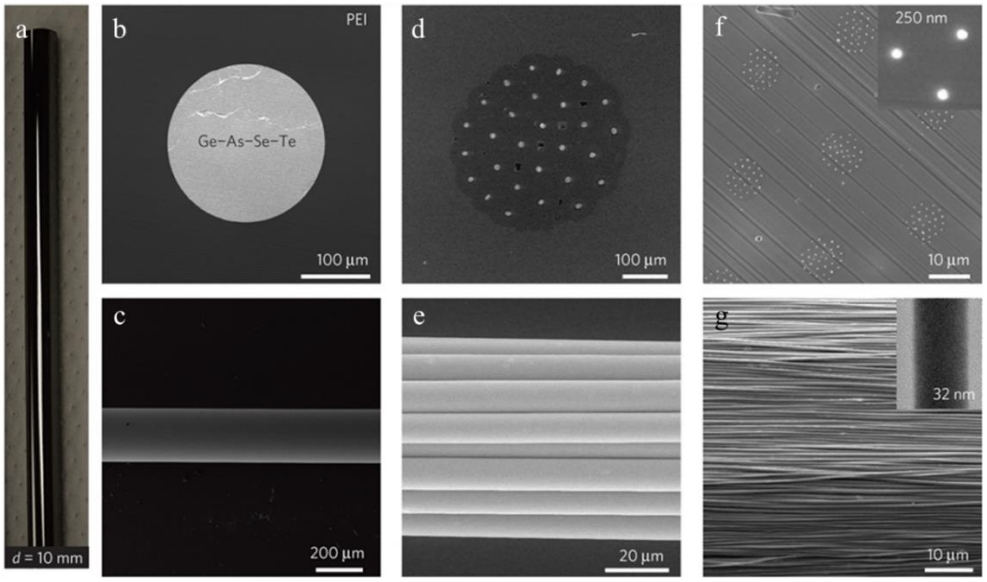

Figure 2.5: (a) A chalcogenide semiconductor rod is reduced to (b, c) hundreds of meters of single 200 µm diameter wire, (d, e) 30 wires of 5 µm diameter and (f, g) 1.000 wires of 250 nm diameter. Nanowires are extracted from polymer matrix by dissolving the polymer encapsulation in organic solvents, retaining their global alignment. Inset: Transmission electron microscopy image of a single 32-nm-thick nanowire.

Chapter 3

Large Area Chalcogenide Nanowire Based Photodetection Device

3.1. Introduction

Nanowires have long been among the most promising building blocks for future low power, high speed electronic devices due to their superlative physical properties. Albeit huge efforts towards their design, fabrication and characterization for a considerable time, it is striking that to date large scale production and integration of nanowire devices have not emerged, where their assembly into functional devices is identified as the main barrier before their large scale utilization. Although, there have been reports on nanowire integration into electronic circuitry [28-30]; we also believe there is ample room for various strategies towards this end. In this chapter, we demonstrate the feasibility of a new kind of indefinitely long, aligned, polymer encapsulated nanowire arrays, produced using a recently reported technique of iterative size reduction method [23], for integration into functional devices. Using the technique we are able to produce many different types of nanowires of various material compositions including chalcogenides, semiconductors, polymers or metals, with various functionalities such as photoconductivity, piezoelectricity, or structural coloring [31]. These nanowire arrays with their unique composition and geometry are also convenient for large area nanowire based device construction.

As a proof of principle, we constructed a chalcogenide nanowire based large area photodetection device [25]. We assembled polymer fibers containing hundreds of continuous parallel selenium nanowires manually on a lithographically defined circuit,

and then we removed the polymer by dissolving it in an organic solvent, in a controlled manner. The exposed nanowires remained over the electrical contacts as a monolayer, forming the photodetection units composed of hundreds of parallel aligned nanowires. We constructed the device within, but not restricted to, an area of 1 cm^2, containing 10x10 pixels. After integration to a designed electronic readout hardware, we managed to detect and display alphabetic characters on the sensor surface exposed to the dark field illumination of some alphabetic characters. The research can be extended towards many directions, since this method could be used to cover very large surfaces with various types of nanowires, and the process is substrate independent, which might facilitate production of nanowire based devices on flexible and non-planar surfaces.

3.2. Fabrication and Characterization of Selenium Wires

We utilized the iterative thermal size reduction technique (see Chapter 2) for production of polyethersulfone (PES) polymer encapsulated indefinitely long and axially aligned selenium nanowires. A bundle of selenium nanowires with removed polymer jacket by dichloromethane (DCM) can be seen in Figure 3.1.

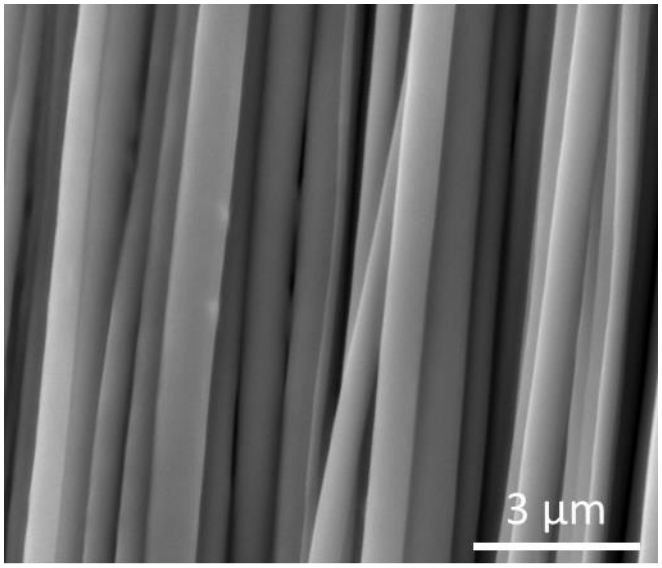

Figure 3.1: SEM image of the amorphous selenium nanowire array.

Selenium is an interesting chalcogenide material which is convenient to thermal drawing to obtain fibers [23], as well as it has photoconductivity [32], light induced crystallization, and phase dependent electrical conductivity [33]. Selenium has photosensitive conductivity in crystalline state, and can be crystallized by thermal

annealing [34] or exposing to specific organic reagents including pyridine, aniline, piperidine, which are all ring compounds containing nitrogen [35]. In order to investigate size dependent properties of selenium fibers produced by thermal drawing, three different set of selenium wires, which were designated by Step 1, Step 2 and Step 3 according to their decreasing radii, were selected. The first two step microwires were crystallized by thermal annealing, while the third step nanowires were crystallized by diluted pyridine as a 50% aqueous solution.

Photoconductivity of the micro and nanowires with different sizes were compared by measuring of the photocurrent under illumination with broadband light source using setup shown in Figure 3.2. Electrical measurements were performed with Keithley 2400 Source-Meter controlled by a computer program written in C#. The software can be used to capture time series data of current *I* and voltage *V* simultaneously or to measure *I-V* curves. A 50 W light source was used for illumination. Electrical contacts to the micro and nanowires were formed by applying silver paint. Current was monitored while applying a constant voltage of 10 Volt, and light source was on-off modulated by a switch. The time series data of photoconductance are given in Figure 3.3. All data were normalized according to the corresponding dark current values, which were on the order of picoamperes. As can be deduced form the photoconductance measurements of selenium wires of different radii, the wires have a size dependent photo-sensitivity and photo-responsiveness. Selenium wires having submicron diameters have superior properties when compared to the wires of micron size diameters. Consequently, selenium nanowires were used as a photosensitive elements in the construction of a photodetection device as described in the following sections.

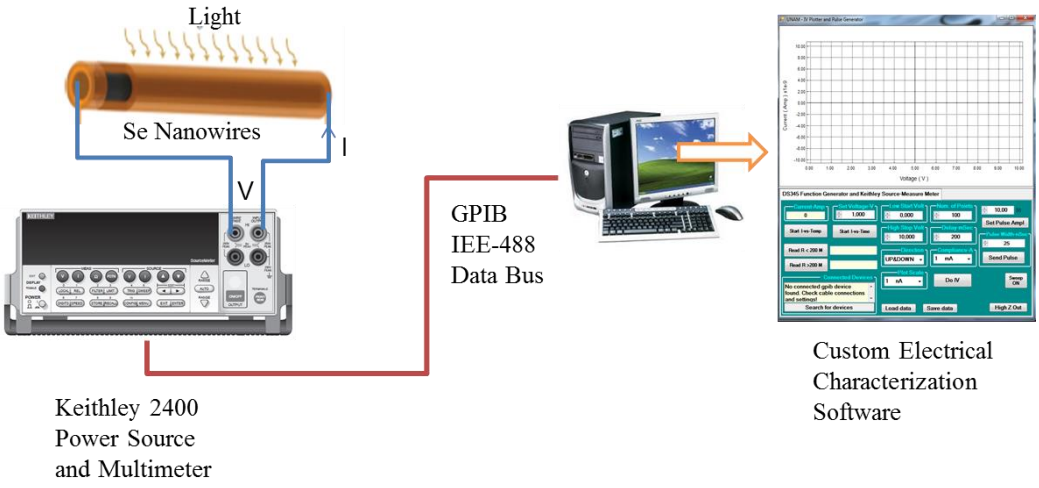

Figure 3.2: Electrical characterization setup used for the measurements of photoconductive properties of Se nanowires.

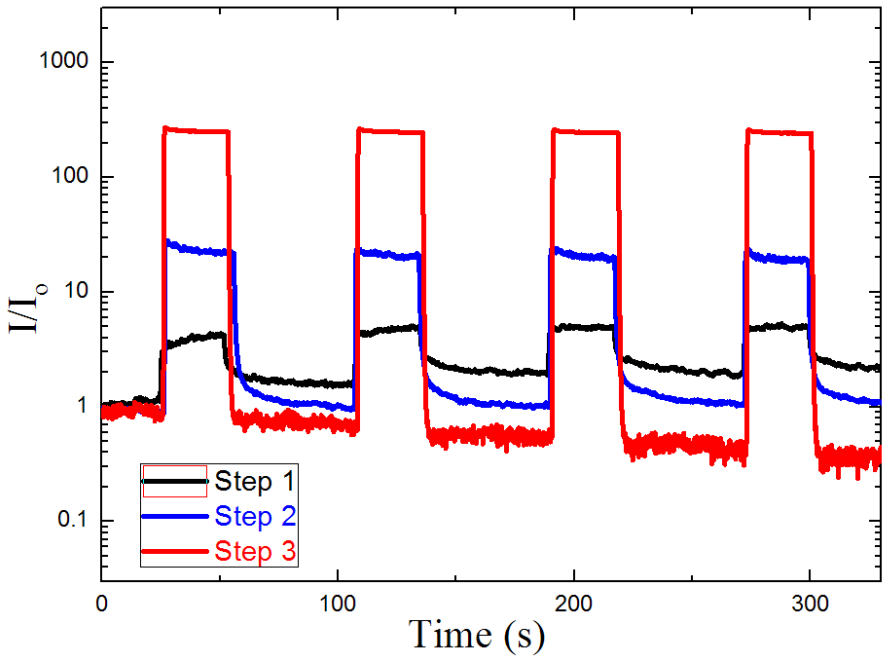

Figure 3.3: Size-dependent photoconductivity of selenium nanowires. Light was on-off modulated and meantime photocurrent was recorded at applied voltage of 10 Volts.

3.3. Integration of Selenium Nanowire Arrays

Selenium nanowire bundles produced by iterative size reduction technique have very convenient properties for manual manipulation such as being embedded and globally oriented in polymer fibers which can be handled easily. Using this convenience, we manually integrated selenium wires of 500 nm in diameter onto a lithographically defined electrical circuitry, which was produced by gold deposition on a chip of Pyrex glass and lift-off method resulting into electrode pairs and pathways (see Figure 3.4). The chip of the circuitry consists of a 10×10 pixel array in an area of 1 cm^2.

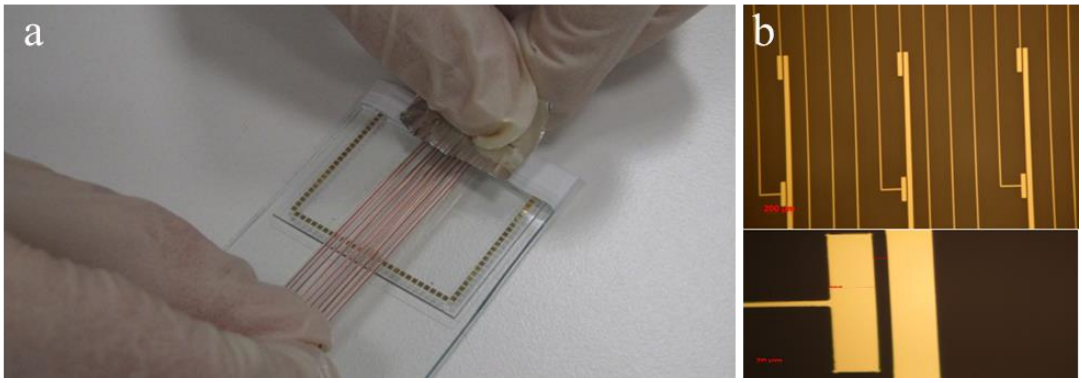

Figure 3.4: Macroscopic assembly of nanowires over a lithographically defined circuitry. (a) First step of nanowire integration to a macroscopic circuitry is manual alignment and accommodation of polymer fiber arrays containing hundreds of nanowires embedded inside. Second step is dissolving the polymer encapsulation and dispersion of nanowires over electrode pairs as monolayers. Third step is crystallization of the selenium nanowires with pyridine solution. (b) Optical microscope image of gold electrical pathways for signal and ground electrodes on the circuit.

We manually assembled fibers on the chip and after stabilizing their position with Teflon tape, we immersed them in DCM with a slight tilt. Without disturbing the orientation of the exposed individual nanowires, we gently washed the chip with DCM to remove the PES remnants. For the crystallization process, we immersed the chip with nanowires into a 50% by volume aqueous pyridine solution overnight. SEM micrographs of resulting crystalline selenium nanowires over the circuitry and a single pixel of the circuitry are shown in Figure 3.5.

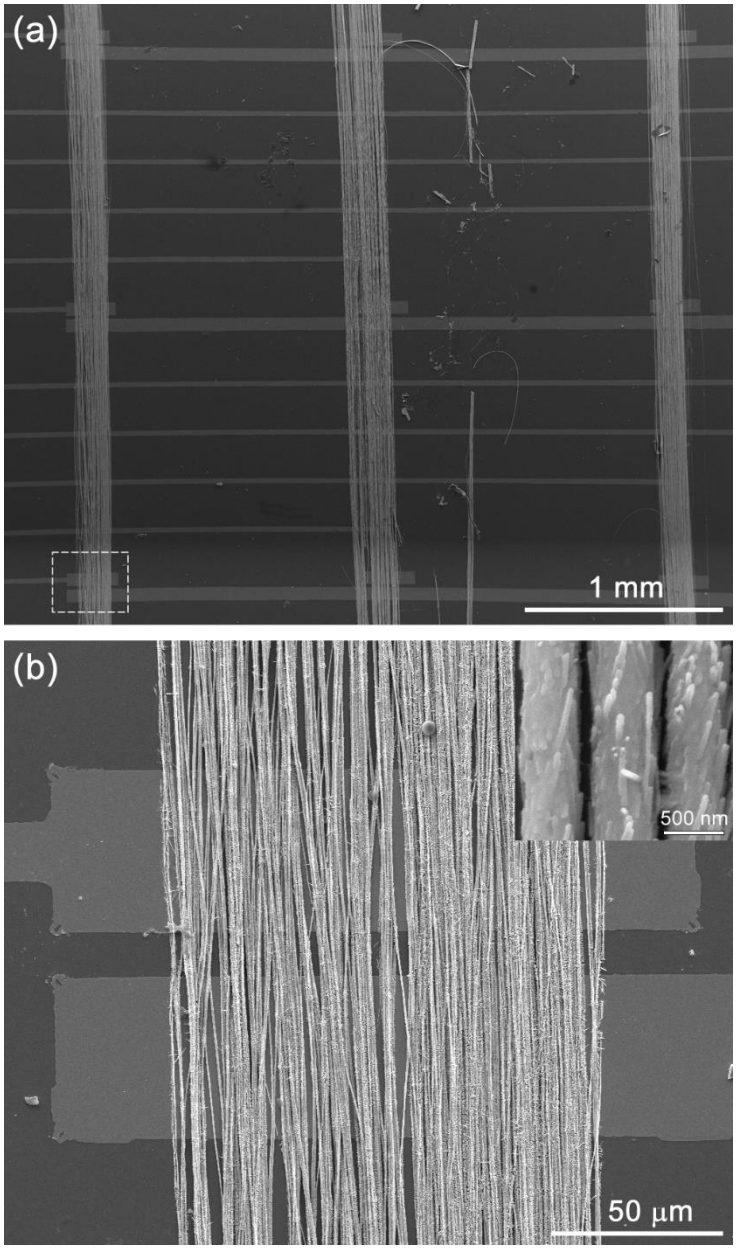

Figure 3.5: SEM image of the photodetection circuit with nanowire based pixels. (a) SEM image of crystallized selenium nanowires lying over ground and readout electrodes of the circuitry forming pixels. (b) SEM image of a single pixel, composed of hundreds of photoconductive selenium nanowires aligned over electrode pairs, which have a separation of 10 micrometers. A high resolution SEM image of nanowires can be seen in the inset.

3.4. Design and Demonstration of a Large Area Photodetection Device

To use a circuitry composed of nanowire-based pixel array as an imaging device, photocurrent of each pair electrode needs to be measured and interpreted for the construction of corresponding image pixel in gray scale. To accomplish this goal, we designed an electronic hardware to capture photoresponse of each and every pixel and to send relevant data to a custom application software for image construction. Schematics of the circuit designed by CadSoft Eagle PCB design software and printed circuit board layout are given in Figure 3.6 and Figure 3.7, respectively.

The circuit is consists of seven 16-channel analog multiplexer/demultiplexer (74HC4067) with four address inputs, one USB-to-UART converter (FT232R), a microprocessor with digital signal processing capabilities (dsPIC30F4011), a voltage regulator, and two LEDs for power and data transfer status. Firmware of the microprocessor is written by using C programing language in MPLAB integrated development environment (IDE). Every pair electrode, which are in a voltage divider configuration to convert photocurrent into voltage signal, are connected to the input port of the microprocessor through analog multiplexers. Seven input channels of microprocessor are multiplexed by four address input ports of the multiplexers and concurrently sampled. Voltage signal of every channel are then 10 bit digitized and transferred as ASCII data via USB. Total number of channels with seven analog multiplexers is 112, however, twelve of the channels are used as spare ports replacing some channels with cross talk. Using USB-USART converter chip, data is transferred with 19200 baud rate and can be read as if there is an assigned serial COM port. Surface mount packages (SMD) for electronic components are used in printed circuit board which has two copper plates at both sides. Electrical connections between channel ports and contact pads of the photodetection circuitry on the electronic hardware are made using soldering with thin enameled copper wires. Device is designed to be powered by USB only or external power source, which can be selected by a switch on the board. Final status of electronic hardware with nanowire integrated circuity can be seen in Figure 3.8.

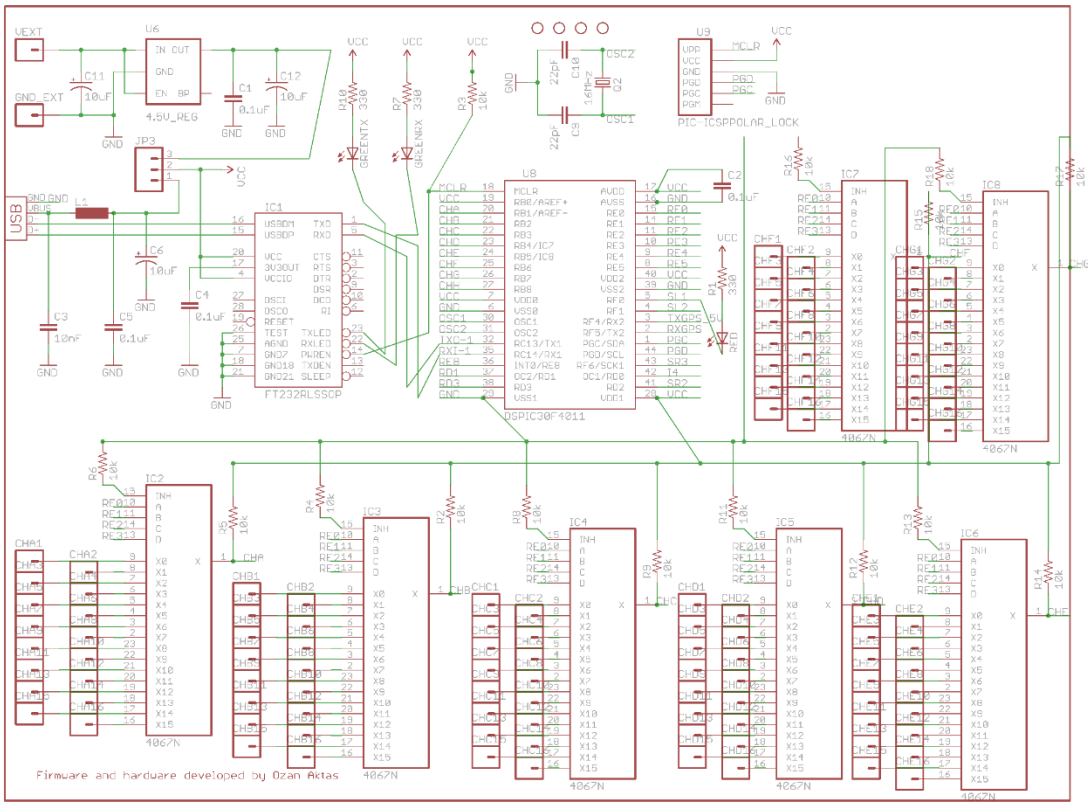

Figure 3.6: Electrical circuit design of nanowire based photodetection device.

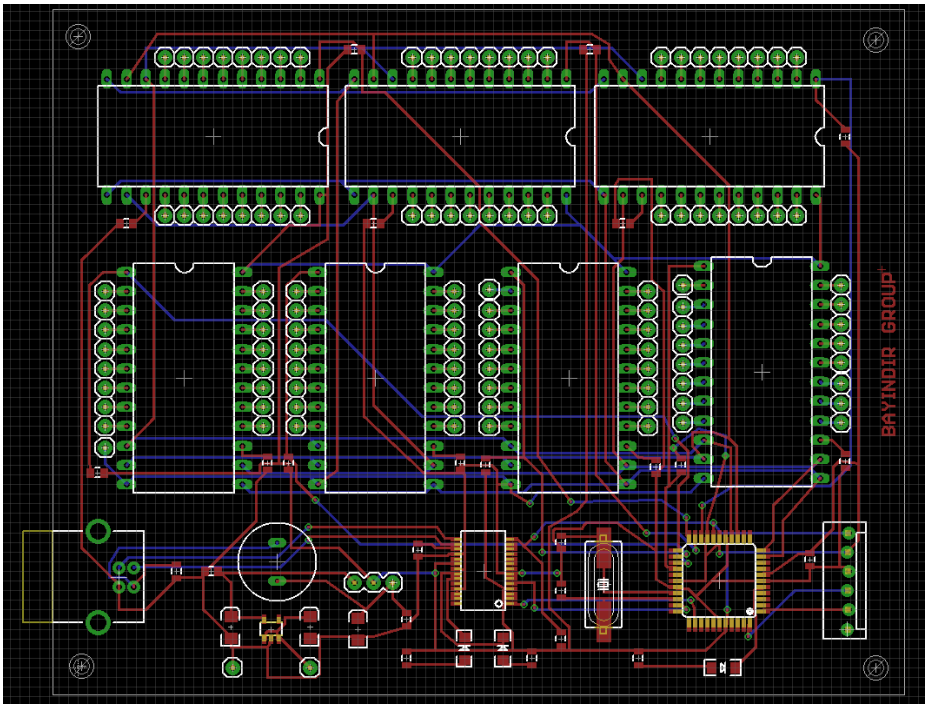

Figure 3.7: Printed circuit board layout of nanowire based photodetection device.

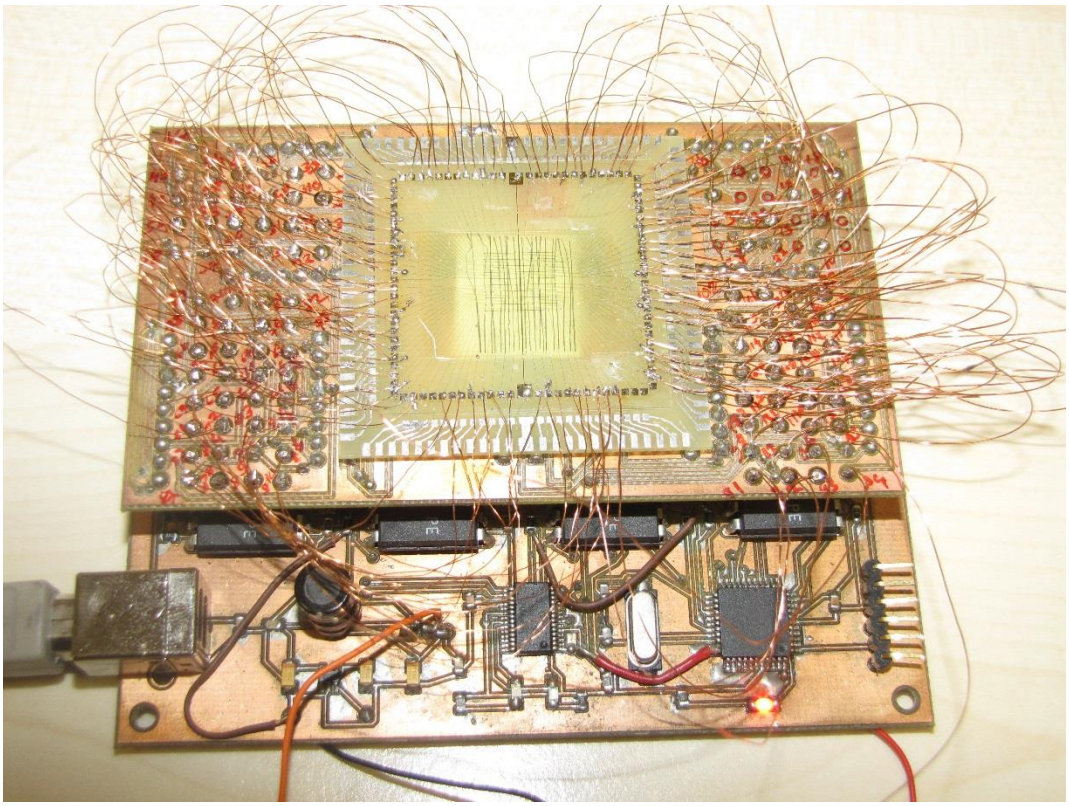

Figure 3.8: Photodetection device with electronic hardware and selenium nanowire integrated circuitry on the top. Device can be powered by USB or external power source. Each pixel is addressed by multiplexers and sampled by microprocessor. A voltage signal corresponding to a level of light intensity is measured for every pixel and data is transferred to a PC via USB.

A custom software is written in C# programing language in MS Visual Studio 2010 IDE in order to read serial data as packages from a virtual COM port and to construct an image of the captured photoresponse in gray scale. User interface of the developed software can be seen in Figure 3.9. A first order digital low pass filter is also implemented in the software to reduce signal noise.

Before constructing an image, each pixel must be calibrated to match their photo-sensitivities since they have slightly different responses to the same light intensity due to the fabrication ambiguities such as the number of nanowires having contact with electrode pairs and electrical contact quality. Distribution of pixel photosensitivity shows that majority of pixels has almost same sensitivity (on the order of 10^3) except a few highly sensitive and insensitive pixels (see Figure 3.10). The device is 68% functional. Calibration is done by the software for each pixel using photoresponse values of static dark and bright illumination of predetermined intensity of light.

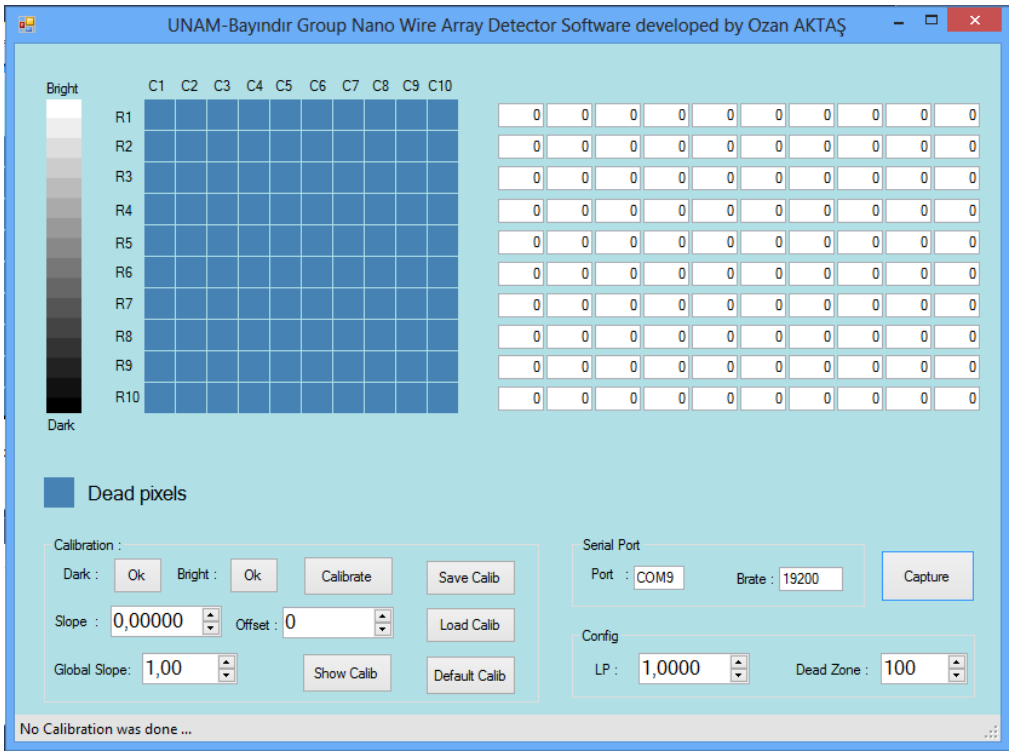

Figure 3.9: User interface of the developed software for the construction of captured image by the nanowire based photodetection device.

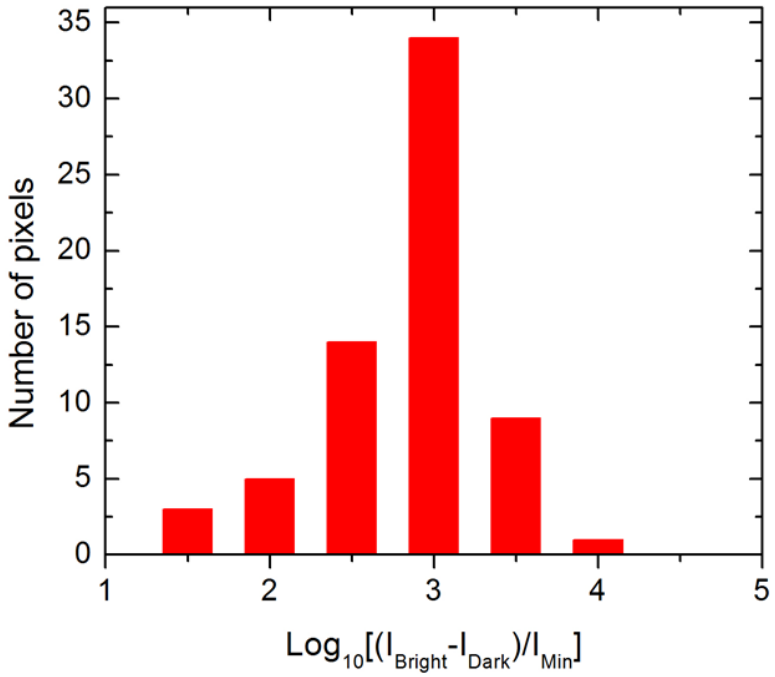

Figure 3.10: Histogram of pixel photo-sensitivities normalized with minimum level of current that can be detected by the circuit.

In order to create an image, dark field illumination of some alphabetic characters is applied via passing white light through transparent parts of a shadow mask prepared by printing. A schematics for the demonstration is shown in Figure 3.11(a). After proper calibration of pixels via the software, resulting images of full exposure of the device to static dark and bright illumination are shown in Figure 3.11(b). Blue pixels denote dead pixels, which are found to be completely insensitive to the light as a result of broken metal lines produced by lift-off process or misalignment of the fibers. Using close contact masks, dark field illumination of characters in the word "UNAM" are projected on the device and captured by the software as images shown in Figure 3.11(c). Using right-angle sided fonts and careful alignment of close contact masks over the circuitry of the sparsely distributed pixels, we obtain sharp contrast images.

Image resolution is as low as 1 pixel/1 mm or 4 dpi due to the sparsely distributed pixel over an active area of 1 cm^2. However, decreasing the space between electrode pairs and increasing the number of pixel electrodes per unit length will increase the resolution. Unfortunately, increase in pixel numbers comes along with the electrical readout problem, which requires addressing circuits such as used in active matrix displays. Very high impedance (on the order of 10^8 ohms) of nanowires between pair electrodes is another electrical interfacing problem, which can be resolved by using impedance matching circuits to analog digital converters in microprocessor. In addition, cross talk can occur between pixels because of the electrical multi-pathways from a signal line to the other common ground lines having contact with same nanowire bundle of the pixel. Fortunately, these pathways have much more resistance in comparison with that of the closest gap between pixel electrodes which is 10 micrometers.

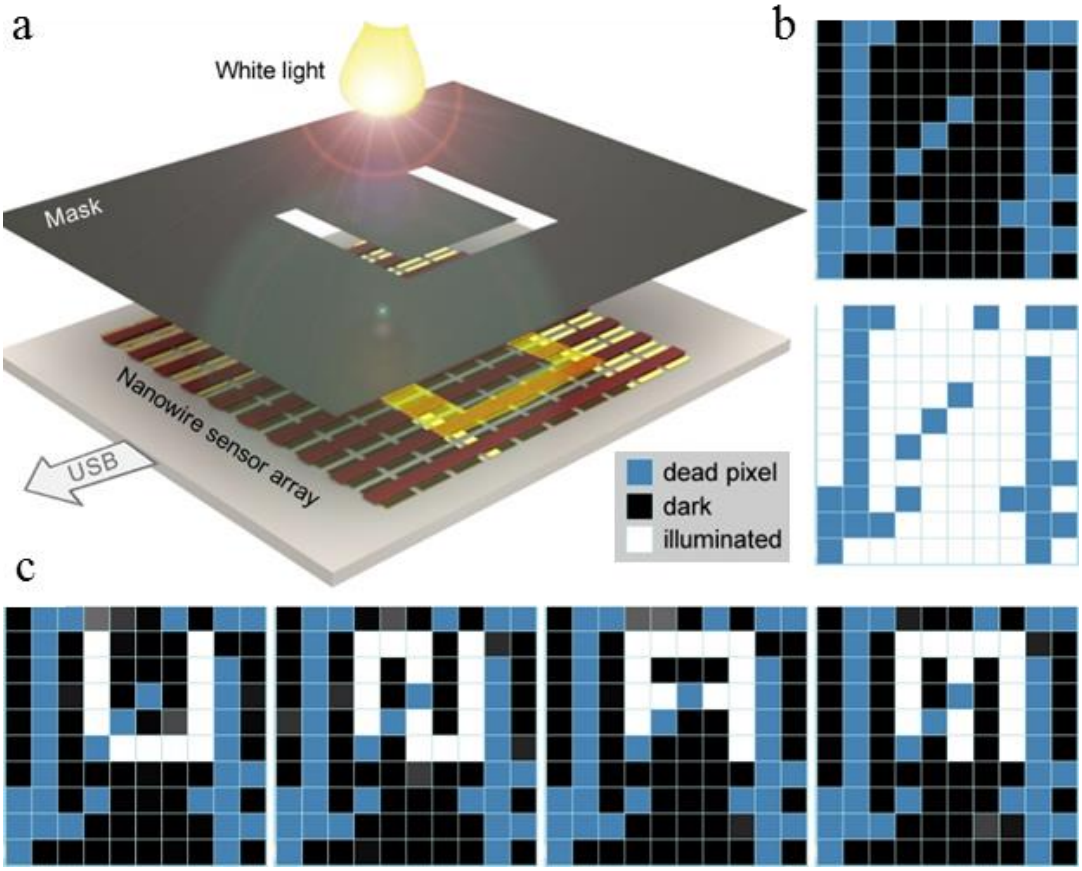

Figure 3.11: Demonstration of the large area nanowire based photodetection device. (a) Schematics of dark field illumination of some characters onto nanowire integrated photodetection device. (b) Software constructed image of a calibrated device after full exposure to a light source for static dark and bright illumination. (d) Captured images of dark field illuminated alphabetic characters of "UNAM". Blue pixels are dead pixels.

Chapter 4

Whispering Gallery Mode Resonators

4.1. Introduction

Light, the fastest entity known in the universe, nevertheless can be trapped in optical analog of a prison called “optical resonator” [36]. Conventional optical resonators consist of two mirrors recirculating light resonantly as in traditional Fabry-Perot (FP) resonators. However, these resonators suffer from difficulties in their assembly, alignment and binding, and vibrational instabilities. In addition, reducing size of these resonators can be very expensive and difficult task. On the other hand, a particular type of resonators which can confine light in concave surfaces of high index dielectric media via total internal reflection, are not prone to these mentioned problems. These optical resonators called “Whispering Gallery Mode (WGM)” resonators, due to the an acoustic analogy observed a century ago by Lord Rayleigh inside the dome of St Paul’s Cathedral in London [37]. It was named as WGM, because a whisper uttered against the wall of the dome can travel along the surface, hence can be heard by a listener at any other point around the gallery. He also suggested electromagnetic version of these surface waves. First theoretical understandings of WGM resonators were accomplished by Mie on the scattering of electromagnetic waves on spheres [38], and Debye on the derivation of resonant frequencies of dielectric and metallic spheres [39]. Existence of high frequency electromagnetic oscillations was pointed out in suitably shaped dielectric objects by Richtmyer [40], and general properties of electromagnetic oscillation in dielectric spheres was widely discussed later by Gastine [41]. First experimentally observation of WGM was done by laser action in solid state WGM lasers [42] and by elastic light scatterings in liquid spherical particles. WGM

were also utilized to measure size, shape, refractive index and temperature of spherical particles [43, 44]. Recent theoretical and technological advances can be found in some reviews [45-48].

The motivation behind temporal and spatial confinement of light in optical resonators is enhancement of light-matter interactions to reduce the threshold for nonlinear optical phenomena such as third harmonic generation [49], four wave mixing [50] and lasing [51] or to increase sensitivity of biological sensors for the ultimate detection of entities such as a single virus [52]. Exploiting high quality factor microresonators has been resulted in many photonic devices with a myriad applications during the last decade, some of which are low threshold lasers [53], frequency comb generators [54] and filters [55]. Especially surface tension induced resonators in sphere [56] and toroid [57] geometries have attracted a considerable interest, due to their micron scale volumes with atomically flat surfaces. Along with the perfection comes the highest temporal and spatial confinement of the light in terms of quality factors ($Q \leq 10^9$) and mode volumes.

The microspheres are the simplest type of WGM resonators. They are often produced by a melting process enabling surface tension forces to create a smooth spherical surface. Although their fabrication is easy, resonance structure of a microsphere is highly complicated due to various modes with equatorial, radial and polar field dependencies. However, spherical WGMs are similar to atomic orbitals and have analytic solutions for the electromagnetic problem. WGMs are actually considered to be electromagnetic waves with high angular momentum (high azimuthal and angular mode numbers), which are localized and resonantly circulating in the equatorial belt of the cavity. Experimental and theoretical aspects of coupling light into these WGM resonators will be revised in the next chapter.

4.2. Ray Optics in 3D Cavities

Whispering gallery modes in a sphere cavity can be simply considered as circulating rays (see Figure 4.1(a)) at incident angles of $\theta_1 \approx 90°$ via total internal reflection (TIR) mechanism due to difference between refractive indices of medium and cavity. The resonance condition for a light ray traveling around the perimeter of the cavity, occurs when a round-trip optical path length is a multiple of wavelength λ:

$$2\pi r n_s = m\lambda \tag{4.1}$$

where r is radius and n_s is refractive index of sphere cavity, m is an integer, and λ is wavelength of the ray. Wave nature must be considered for correct predictions to be made, nevertheless; ray picture is useful for understanding the basics of the phenomenon.

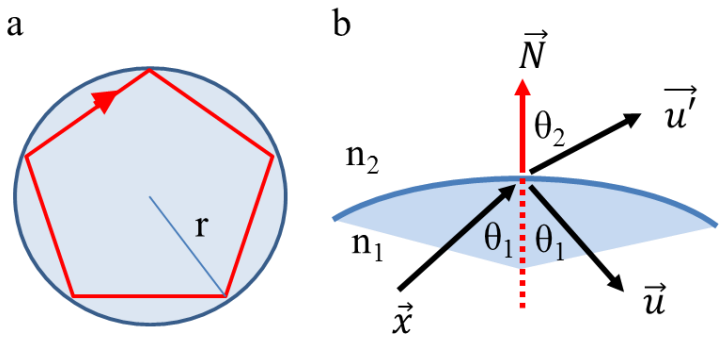

Figure 4.1: a) Circulating light ray inside a high index cavity ($n_1 > n_2$) via total internal reflection. b) Schematics of incident $\vec{x}$, reflected $\vec{u}$ and refracted $\vec{u}'$ rays at the interface.

4.2.1. Vector Formulation of Refraction

We can derive vectorial formulation of Snell Law:

$$n_1 \sin\theta_1 = n_2 \sin\theta_2 \tag{4.2}$$

using the relations between of incident $\vec{x}$, reflected $\vec{u}$ and refracted $\vec{u}'$ unit ray vectors as shown in the schematics of Figure 4.1(b). Since they are unit vectors and coplanar, we can rewrite Equation 4.2 as

$$n_1(\vec{x} \times \vec{N}) = n_2\left(\vec{u'} \times \vec{N}\right) \tag{4.3}$$

Thus, we obtain

$$(n_1\vec{x} - n_2\vec{u}') \times \vec{N} = 0 \tag{4.4}$$

The expression in the parenthesis must be parallel to the normal vector $\vec{N}$, therefore we can write

$$n_1\vec{x} - n_2\vec{u}' = a\vec{N} \tag{4.5}$$

where *a* is a unknown constant. Taking dot product of both sides with $\vec{N}$, and using the relation $\vec{N} \cdot \vec{N} = 1$, we find that a is:

$$a = n_1\vec{N} \cdot \vec{x} - n_2\vec{N} \cdot \vec{u'} = n_1 \cos\theta_1 - n_2 \cos\theta_2 \tag{4.6}$$

Using again Snell Law, we can write instead of $\cos\theta_2$:

$$\cos\theta_2 = \frac{n_1}{n_2}\sqrt{cos^2\theta_1 - [1 - (n_2/n_1)^2]} \tag{4.7}$$

Inserting Equation 4.7 into Equation 4.6, we get for *a* is:

$$a = n_1 \cos\theta_1 - n_1\sqrt{cos^2\theta_1 - [1 - (n_2/n_1)^2]} \tag{4.8}$$

Using Equation 4.5, the refracted ray vector $\vec{u}'$ is:

$$\vec{u}' = \frac{1}{n_2}(n_1\vec{x} - a\vec{N}) \tag{4.9}$$

4.2.2. Vector Formulation of Reflection

Similarly, vectorial formulation for reflection can found using the fact that reflection and incident angles are same. Thus we have:

$$\vec{x} \times \vec{N} = \vec{u} \times \vec{N} \tag{4.10}$$

as a starting relation, which can be rewritten as:

$$(\vec{x} - \vec{u}) \times \vec{N} = 0 \tag{4.11}$$

Due to same reasons before, we have

$$\vec{x} - \vec{u} = b\vec{N} \tag{4.12}$$

where *b* is a unknown constant. Taking dot product of both sides with unit vector $\vec{N}$, we can obtain

$$b = \vec{N} \cdot \vec{x} - \vec{N} \cdot \vec{u} = \cos\theta_1 - (-\cos\theta_1) = 2\cos\theta_1 \tag{4.13}$$

Finally, the reflected ray vector $\vec{u}$ is:

$$\vec{u} = \vec{x} - 2\cos\theta_1\,\vec{N} \tag{4.14}$$

4.2.3. Ray Tracer Algorithm and Simulation Results

Ray tracing in 3D space can be done by propagating light, which has initially at some point of space (x_0, y_0, z_0) inside a cavity and has some direction described by an initial unit vector $\vec{x}_0$, with small steps along a straight line until the ray come across the surface, where at the point of intersection if incident angle satisfies the relation

$$cos^2\theta_1 = (\vec{N} \cdot \vec{x})^2 \geq 1 - n_2^2/n_1^2 \tag{4.15}$$

the ray refracts and escapes out of the cavity, so simulation ends here. We can use Equation 4.8 and Equation 4.9 to find the refracted ray vector $\vec{u}'$, which gives the escape direction. However, if the condition given by Equation 4.15 does not satisfy the relation, we can use Equation 4.14 to find the reflected ray vector $\vec{u}$. Since now we know the intersection point and the direction light reflects to, we can continue to propagate light until we come across another point of the surface again. Same procedure can be applied iteratively as much as pleased or until the ray escapes. Normal unit vector $\vec{N}$ can be found at every intersection point by calculating normalized gradient vector ∇S at that point, where S is the implicit function defining the cavity surface. For example, a toroidal cavity is set of points satisfying

$$\left(R - \sqrt{y^2 + y^2}\right)^2 + z^2 = r^2 \tag{4.16}$$

where *r* and *R* are minor and major radius of toroid, respectively. Implicit function S can be taken as

$$S(x, y, z) = \left(R - \sqrt{y^2 + y^2}\right)^2 + z^2 - r^2 \tag{4.17}$$

and the gradient is

$$\nabla S = \frac{\partial S}{\partial x}\hat{\imath} + \frac{\partial S}{\partial y}\hat{\jmath} + \frac{\partial S}{\partial z}\hat{k} \tag{4.18}$$

We first studied a toroidal cavity taking different initial conditions for the ray and we found that four types of trajectory can be used to confine the light propagating inside the cavity as shown in Figure 4.2. The first type is the WGMs. Next, we studied an oblate spheroid cavity. Results were qualitatively compared with the results of another simulation which we did by using finite difference time domain (FDTD) method in Lumerical software (see Figure 4.3(a, b)). Light can be confined only an annular region of the space in the cavity, which is called caustics. Electromagnetic wave solutions and ray optics solutions show identical caustics for light coupled into an oblate spheroid cavity as shown in Figure 4.3(c, d).

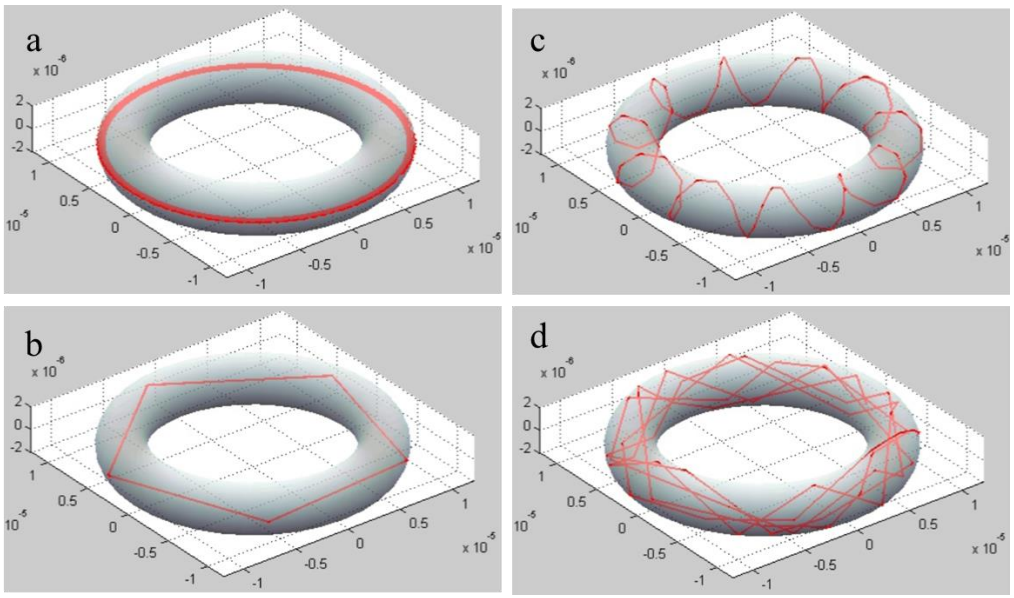

Figure 4.2: Different ray trajectories in a toroidal cavity. (a) Whispering gallery modes. (b) Bowtie modes. (c) Spiral modes. (d) Chaotic modes. Units of axes are meter.

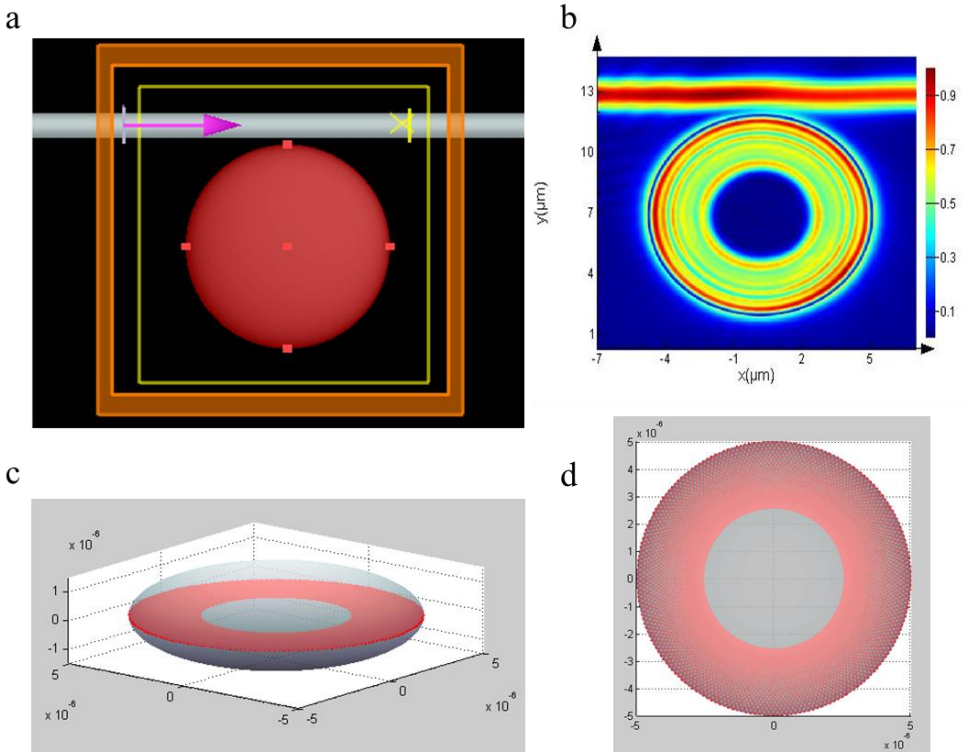

Figure 4.3: (a) Lumerical FDTD simulation configuration. (b) High radial order modes in an oblate ellipsoidal cavity. (c) Caustics of modes in 3D perspective. (d) Caustics of modes in top view. Units of axes are meter.

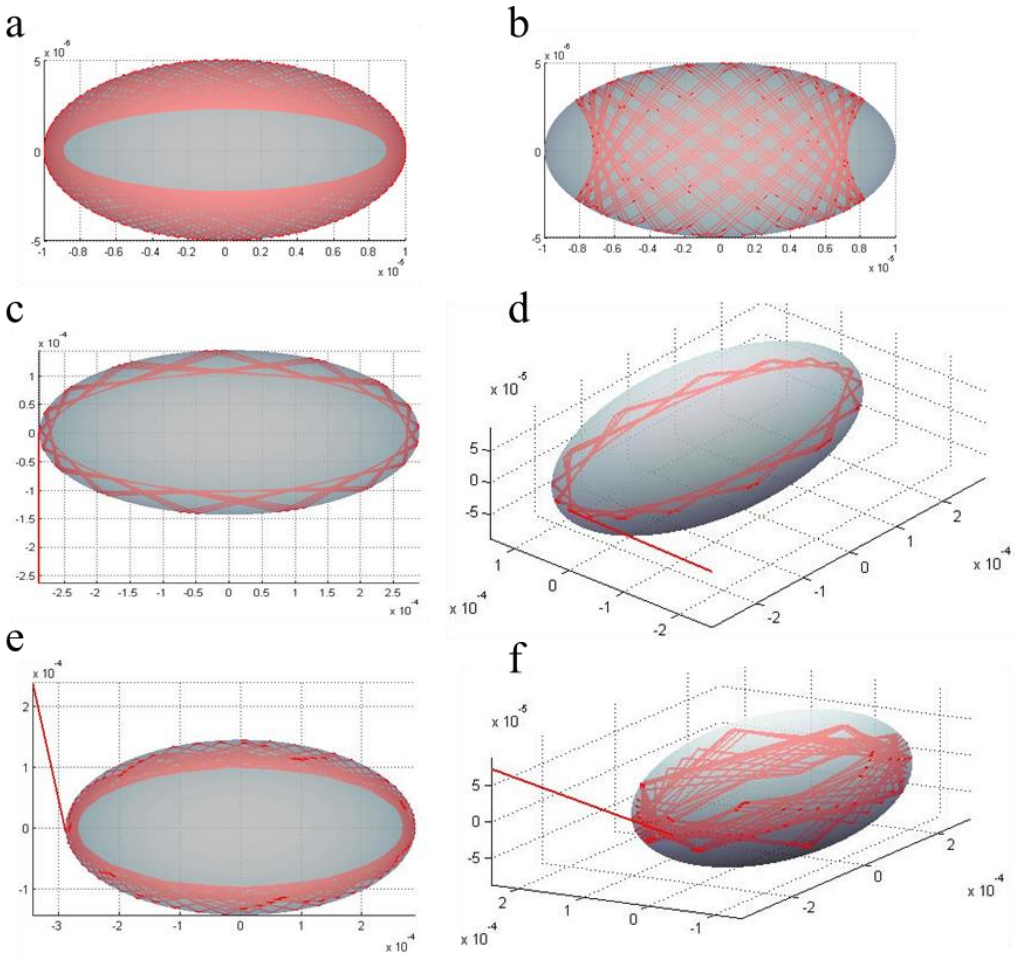

Figure 4.4: Different caustics and escaping mechanisms in a triaxial ellipsoidal cavity. (a) Outer caustics. (b) Inner caustics. Escape trajectory of a horizontal mode in a (c) top and (d) perspective view. Escape trajectory of a skewed mode in a (e) top and (f) perspective view. Units of axes are meter.

Finally, we studied a triaxial ellipsoidal cavity, which is an asymmetric cavity. There are two kinds of caustics found for the confined light in this case as shown in Figure 4.4 (a, b). Asymmetric cavities are known with their directional emission of radiation [58, 59]. Light escapes at point of highest curvature on the cavity refracting tangentially to the cavity surface, where the incident angle is greater than the critical angle of total internal reflection. Ray simulations for horizontal and skewed trajectories, as shown in Figure 4.4(c-f), confirm theoretical expectations. MATLAB codes for ray optics simulation for toroids are given in Appendix A.2.

4.3. Electromagnetic Theory of WGMs

Exact electromagnetic wave solutions in a dielectric cavity can only be found for spherical cavities. The vector solution of Maxwell's equations for a dielectric sphere can be derived from two independent solutions of a scalar equation, which are called Debye Potentials (*U*, *V*) [39, 45].

For a time harmonic field, Maxwell's equations for an isotropic dielectric sphere can be written as:

$$\nabla \times \vec{E} = ik\vec{H} \tag{4.19}$$

$$\nabla \times \vec{H} = -ik\vec{E} \tag{4.20}$$

where $k = (w/c)\sqrt{\varepsilon\mu}$; ε and μ are dielectric constant and magnetic permeability of the sphere. These equations have two types of solutions in spherical coordinate system as TE and TM modes for which radial components of electric field E_r and magnetic field H_r are zero, respectively. For TM modes, $\vec{E}$ field and $\vec{H}$ fields are:

$$E_r = \left(\frac{\partial^2}{\partial r^2} + k^2\right)U\,, \quad H_r = 0$$

$$E_\theta = \frac{1}{r}\frac{\partial^2}{\partial r}\frac{U}{\partial\theta}\,, \qquad H_\theta = -ik\frac{1}{r}\frac{\partial U}{\partial\varphi} \tag{4.21}$$

$$E_\varphi = \frac{1}{r\sin\theta}\frac{\partial^2}{\partial r}\frac{U}{\partial\varphi}, \quad H_\varphi = ik\frac{1}{r}\frac{\partial U}{\partial\theta}$$

and for TE modes, $\vec{E}$ field and $\vec{H}$ fields are:

$$H_r = \left(\frac{\partial^2}{\partial r^2} + k^2\right)V\,, \quad E_r = 0$$

$$H_\theta = \frac{1}{r}\frac{\partial^2}{\partial r}\frac{V}{\partial\theta}\,, \qquad E_\theta = ik\frac{1}{r}\frac{\partial V}{\partial\varphi} \tag{4.22}$$

$$H_\varphi = \frac{1}{r\sin\theta}\frac{\partial^2}{\partial r}\frac{V}{\partial\varphi}, \quad E_\varphi = -ik\frac{1}{r}\frac{\partial V}{\partial\theta}$$

where Debye potentials U, V satisfies a scalar equation which explicitly takes the form in spherical coordinates for both potentials:

$$\frac{\partial^2 U}{\partial^2 r}+\frac{1}{r^2\sin\theta}\frac{\partial}{\partial\theta}\left(\sin\theta\frac{\partial U}{\partial\theta}\right)+\frac{1}{r^2\sin^2\theta}\frac{\partial^2 U}{\partial\varphi^2}+k^2U=0 \tag{4.23}$$

where $k=k_0\sqrt{\varepsilon\mu}$ inside the sphere, $k=k_0$ outside the sphere, and $k=w/c$. By substituting the potential as $U=R(r)\Theta(\theta)\Phi(\varphi)$ in Equation 4.23 and using separation of variables, we obtain the following equations:

$$\frac{d^2R}{dr^2}+\left(k^2-\frac{l(l+1)}{r^2}\right)R=0 \tag{4.24}$$

$$\frac{1}{\sin\theta}\frac{d}{d\theta}\left(\sin\theta\frac{d\Theta}{d\theta}\right)+\left(l(l+1)-\frac{m^2}{\sin^2\theta}\right)\Theta=0 \tag{4.25}$$

$$\frac{d^2\Phi}{d\varphi^2}+m^2\Phi=0 \tag{4.26}$$

where l is angular mode number and m is azimuthal mode number, which can take integers from $-l$ to l. Radial Equation 4.24 can be transformed to Bessel equation with substitution $R(r)=\sqrt{kr}Z(kr)$

$$\frac{d^2Z}{dz^2}+\frac{1}{z}\frac{dZ}{dz}+\left(1-\frac{v^2}{z^2}\right)Z=0 \tag{4.27}$$

where $z=kr$ and $v=l+1/2$. As a result, the solution of the Equation 4.23 has the form

$$U_{lm}^{i}(r,\theta,\varphi)=C_iP_l^m(\cos\theta)\sqrt{kr}J_v(kr)e^{\pm im\varphi} \tag{4.28}$$

for inside of the sphere of radius a (r$\leq a$), and

$$U_{lm}^{e}(r,\theta,\varphi)=C_eP_l^m(\cos\theta)\sqrt{kr}H_v^{(1)}(k_0r)e^{\pm im\varphi} \tag{4.29}$$

for outside of the sphere ($r>a$). $C_{i,e}$ are some arbitrary constants, $P_l^m(x)$ are adjoint Legendre polynomials, $J_v(x)$ are Bessel function of the first kind and $H_v^{(1)}(x)$ are Hankel function of the first kind.

Resonance frequencies and fields are determined by boundary conditions. Tangential components of the electric and magnetic fields must be continuous on the sphere surface, which can be expressed as:

$$\hat{r}\times\vec{E}_{in}=\hat{r}\times\vec{E}_{ex} \tag{4.30}$$

$$\hat{r} \times \vec{H}_{in} = \hat{r} \times \vec{H}_{ex} \tag{4.31}$$

where $\vec{E}_{in}$ and $\vec{E}_{ex}$ are internal and external electric fields, and $\vec{H}_{in}$ and $\vec{H}_{ex}$ are internal and external magnetic fields, respectively. Boundary conditions lead to a characteristic equation which determines admissible values of the $k_0 a$. The characteristic equation for TM modes is:

$$\frac{\left[\sqrt{ka}J_\upsilon(ka)\right]'}{\sqrt{ka}J_\upsilon(ka)} = \sqrt{\frac{\varepsilon}{\mu}}\frac{\left[\sqrt{k_0 a}H_\upsilon^{(1)}(k_0 a)\right]'}{\sqrt{k_0 a}H_\upsilon^{(1)}(k_0 a)} \tag{4.32}$$

and for TE mode is:

$$\frac{\left[\sqrt{ka}J_\upsilon(ka)\right]'}{\sqrt{ka}J_\upsilon(ka)} = \sqrt{\frac{\mu}{\varepsilon}}\frac{\left[\sqrt{k_0 a}H_\upsilon^{(1)}(k_0 a)\right]'}{\sqrt{k_0 a}H_\upsilon^{(1)}(k_0 a)} \tag{4.33}$$

where the prime means a total derivative over the argument of function, i.e., over ka or $k_0 a$. The roots of characteristic equation gives the relation between the wavenumber *k* and the sphere radius *a*. Since there are many roots satisfying the characteristic equations, it is necessary to specify by a third index q what number of the root of Equation 4.32, or 4.33 is used. The radial mode number q corresponds to number of field maximum in radial direction, azimuthal mode number *m* corresponds to number of field maximum (2×m) in the periphery of the sphere, and polar mode number *l-m+1* corresponds to number of field maximum in meridional direction.

Resonance wavelengths corresponding to (*q*, *l*, *m*) mode numbers can be found by solving the characteristic equations or more practically using the asymptotic expansion of the characteristic equation in powers of *l* [60]

$$\begin{aligned} nx_{q,l} = \upsilon + 2^{-\frac{1}{3}}\alpha_q \upsilon^{\frac{1}{3}} - \frac{P}{(n^2-1)^{\frac{1}{2}}} + \left(\frac{3}{10}2^{-\frac{2}{3}}\right)\alpha_q^2 \upsilon^{-\frac{1}{3}} \\ - \frac{2^{-\frac{1}{3}}P\left(n^2 - 2P^{\frac{2}{3}}\right)}{(n^2-1)^{\frac{3}{2}}}\alpha_q \upsilon^{-\frac{2}{3}} + O(\upsilon^{-1}) \end{aligned} \tag{4.34}$$

where $x_{q,l} = ka$ is size parameter, $\upsilon = l + 1/2$, *n* is refractive index of the sphere, α_q is the q_{th} zero of the Airy function $A_i(-z)$, and $P = n$ for TE modes and $P = 1/n$ for TM modes. It is clear that resonance wavelengths depend on polarization and (*q*, *l*) mode numbers, so there is $2l+1$ degeneracy for the modes with respect to azimuthal mode number *m*.

4.4. Numerical Simulations of WGMs

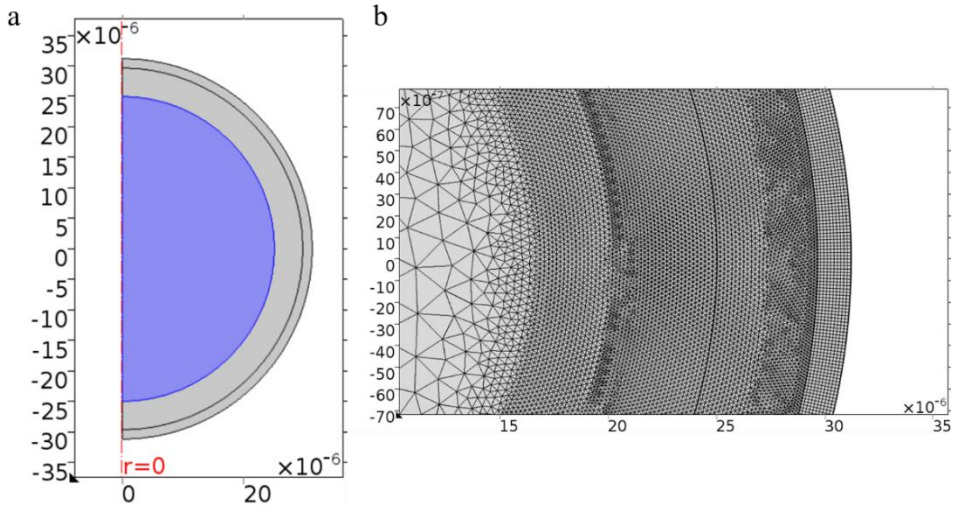

Figure 4.5: Two dimensional axisymmetric FEM based COMSOL simulation. (a) Simulation environment showing half of the sphere of radius 25 μm, air region and perfectly match layer. (b) Zoomed-in figure showing a part of the mesh.

In order to find electric field distributions of WGMs, we performed two dimensional axisymmetric simulations using finite element method (FEM) with COMSOL Wave Optics Module (electromagnetic waves, frequency domain interface). Simulation environment consists of 25 μm radius sphere with refractive index n_s of 2.8, an air region (n_{air} = 1) and perfectly match layer (PML) around the sphere as shown in Figure 4.5(a). Working wavelength λ is 1.55 μm. Air region and PML have thickness of 3λ and λ, respectively. Maximum mesh size is chosen λ/7 for sphere shell and air region, and λ/10 for PML (see Figure 4.5(b)).

In 2D axisymmetry, the electric field varies with the azimuthal mode number *m* as

$$\vec{E}(r,\varphi,z) = \tilde{E}(r,z)e^{-im\varphi} \tag{4.35}$$

For this case, the wave equation for time harmonic and eigenfrequency problems can be rewritten as

$$\left(\nabla - i\frac{m}{r}\hat{\varphi}\right) \times \left[\mu^{-1}\left(\nabla - i\frac{m}{r}\hat{\varphi}\right) \times \tilde{E}\right] - k_0^2 \varepsilon \tilde{E} = 0 \tag{4.36}$$

where $\hat{\varphi}$ is the unit vector in the out-of-plane φ–direction. The azimuthal mode number is taken as *m* = 272 in our case. Distribution of electric field magnitudes, and electric field directions for resonance modes of TM and TE polarizations can be seen in Figure 4.6. Resonance modes are designated as $TE_{(q,\ l,\ l\text{-}m)}$ and $TM_{(q,\ l,\ l\text{-}m)}$. Results of analytic calculations and FEM simulations are compared in Table 4.1. Position of resonance modes can be seen in Figure 4.7.

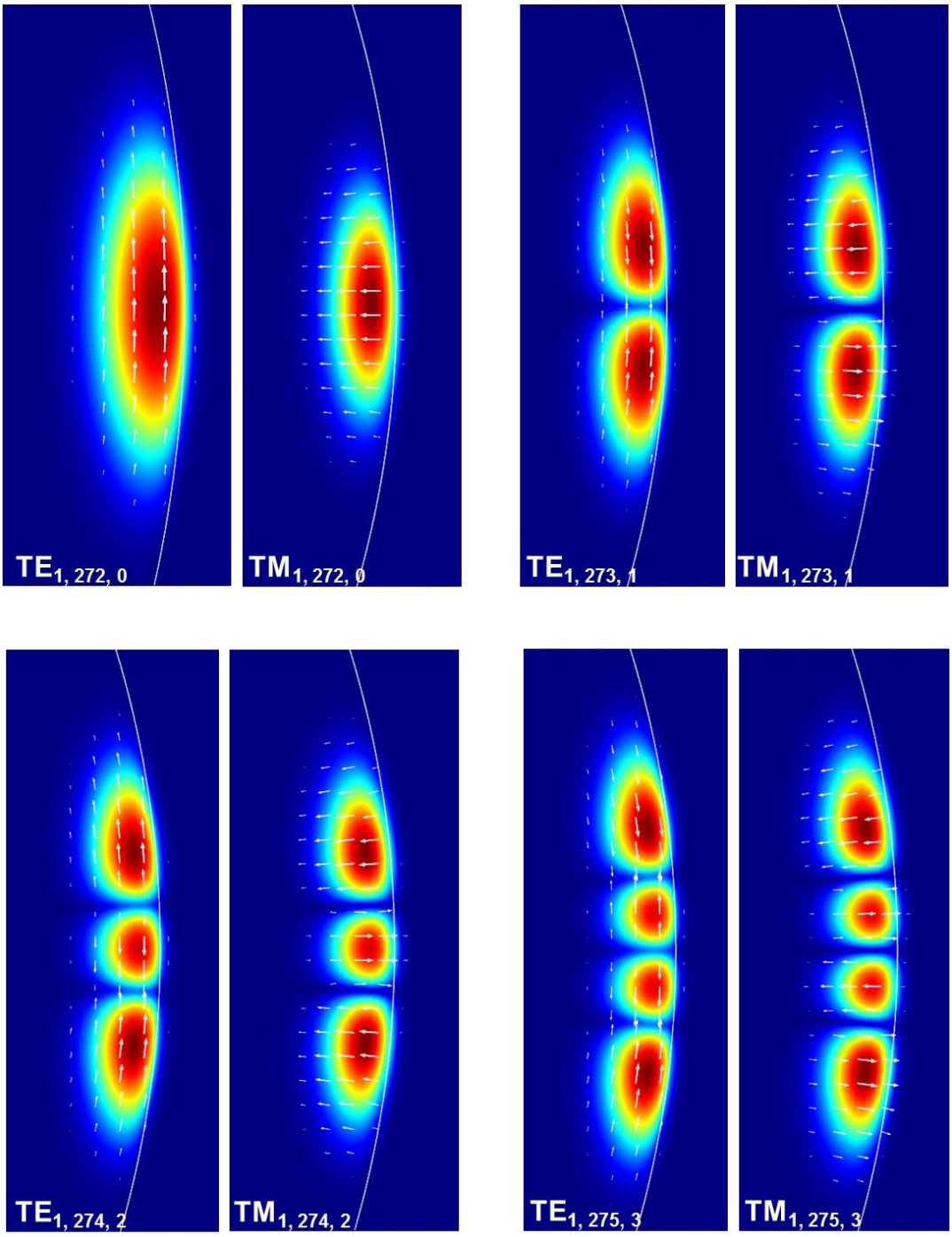

Figure 4.6: Results of FEM simulation showing electric field distribution of Whispering Gallery Modes in a sphere of 25 µm radius. Radial mode number *q* is 1 for all modes and the angular mode number *l* takes values in 272-275. White arrows show electric field vector of WGM.

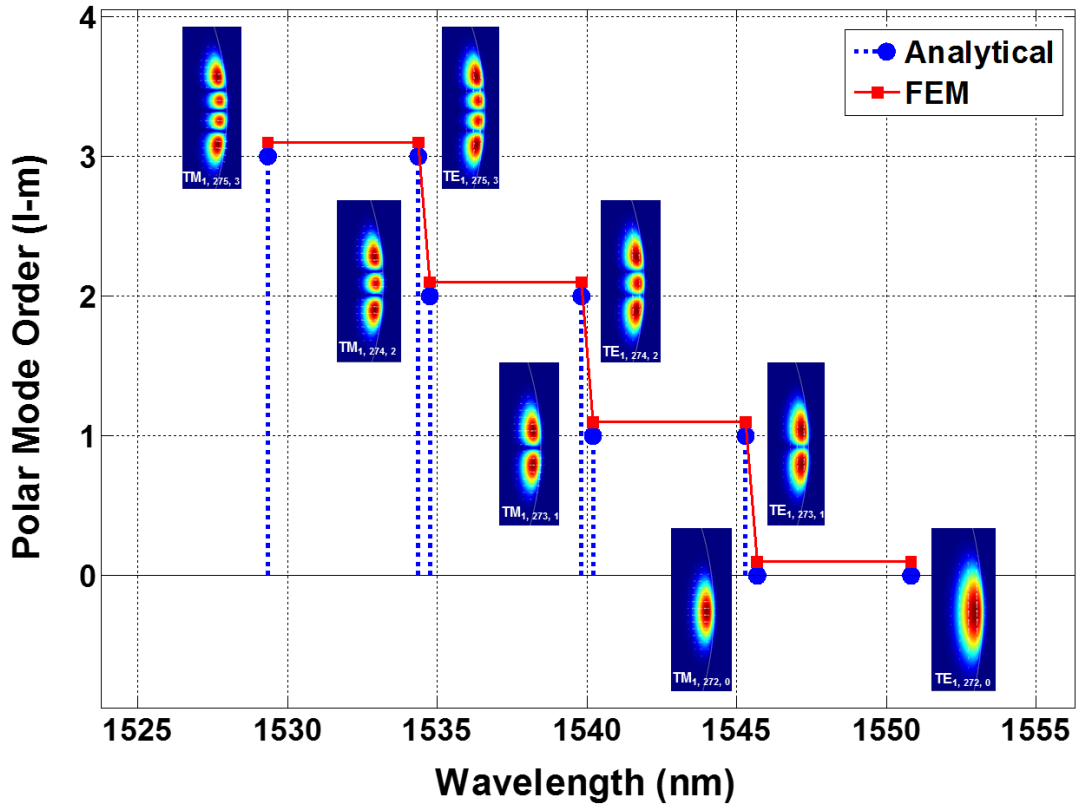

Figure 4.7: Graphics of resonance wavelengths positions calculated by FEM simulations and analytic expression of Equation 4.16.

Polarization	***q***	***l***	***l-m***	**FEM (nm)**	**Analytic (nm)**
TE	1	272	0	1550.81735	1550.84578
TM	1	272	0	1545.69789	1545.69658
TE	1	273	1	1545.28799	1545.31761
TM	1	273	1	1540.20636	1540.20513
TE	1	274	2	1539.79803	1539.82890
TM	1	274	2	1534.75384	1534.75275
TE	1	275	3	1534.34702	1534.37924
TM	1	275	3	1529.33993	1529.33903

Table 4.1: Comparison of FEM simulation and analytic results. Resonance wavelengths are given in the unit of nanometer.

4.5. Free Spectral Range

Free Spectral Range (FSR) is defined as the frequency or wavelength separation between successive longitudinal modes of the cavity. Considering fixed radial mode number of *q*, frequency difference between a mode order *l* and mode order *l*+1 can be calculated using the first three terms of the asymptotic expansion in Equation 4.34 as:

$$\begin{aligned}\Delta f_{q,l} &= \frac{c\left(x_{q,l+1} - x_{q,l}\right)}{2\pi} \\ &= \frac{c}{2\pi na}\left[1 + \alpha_q\left(\frac{l+1/2}{2}\right)^{\frac{1}{3}}\left(1 - \left(1 + \frac{1}{l+1/2}\right)^{\frac{1}{3}}\right)\right]\end{aligned} \tag{4.37}$$

where c is speed of light in vacuum. For large *l*, what we obtain for FSR is:

$$\Delta f_{FSR} = \frac{c}{2\pi na} \tag{4.38}$$

The FSR of a micro-sphere cavity resonators can be rewritten in terms of wavelength λ as:

$$\Delta\lambda_{FSR} = \frac{\lambda^2}{2\pi na} \tag{4.39}$$

Considering same *q*, *l*, and *m*, it is also possible to determine the spacing between different modes of TM and TE polarizations as:

$$\Delta f^{TE-TM} = \Delta(nx_{q,l})\frac{c}{2\pi na} \approx \frac{c}{2\pi na}\sqrt{\frac{n^2-1}{n}} \tag{4.40}$$

And the separation between modes of successive radial order *q* is:

$$f_{q+1,l} - f_{q,l} \approx \frac{c}{2\pi na}\left(l + \frac{1}{2}\right)^{\frac{1}{3}}\left(\frac{\pi^2}{3q}\right)^{\frac{1}{3}} \tag{4.41}$$

4.6. Finesse

The finesse F of a resonator is a dimensionless parameter describing the ability to resolve the cavity resonance spectrum. It is defined as the ratio of the FSR and full width at half maximum (FWHM) value of the resonance peak in the spectrum and given as:

$$\mathcal{F} = \frac{\Delta\lambda_{FSR}}{\Delta\lambda_{FWHM}} \tag{4.42}$$

4.7. Mode Volume

Whispering gallery modes of a sphere have different spatial field distributions depending the value of mode orders (*q*, *l*, *m*). Mode volume of the WGMs can be related to the energy density of the optical modes and defined as

$$V_m = \frac{\int \epsilon(r)\left|\vec{E}(r)\right|^2 d^3r}{max\left(\epsilon(r)\left|\vec{E}(r)\right|^2\right)} \tag{4.43}$$

Considering first order radial modes (*q*=1) of a microsphere cavity, the mode volume for WGMs is estimated as [56]:

$$V = 3.4\pi^{\frac{3}{2}}\left(\frac{\lambda}{2\pi n}\right)^3 \upsilon^{\frac{11}{6}}\sqrt{\upsilon - m + 1} \tag{4.44}$$

where λ is the resonance wavelength and $\upsilon = l + 1/2$.

4.8. Quality Factor

Light coupled into a cavity decays due to some energy loss mechanisms such as absorption or scattering and has a life time τ in the cavity described by the decaying stored energy function *U(t)* as:

$$U(t) = U(0)e^{-t/\tau} = U(0)e^{-\frac{w_0 t}{Q}} \tag{4.45}$$

where life time τ is also expressed in terms of quality factor *Q*. *Q*/2π actually gives the number of total oscillations light can survive inside the cavity. Using stored energy function *U(t)*, *Q*-factor can be formally defined as:

$$Q = \frac{w_0 U}{-\frac{dU}{dt}} \tag{4.46}$$

The time dependence of the stored energy suggests that electric field damps as

$$E(t) = E(0)e^{-\frac{w_0 t}{2Q}}e^{-iw_0 t} \tag{4.47}$$

Fourier Transform of the electric field *E(t)* yields:

$$E(w) = \frac{1}{\sqrt{2\pi}}\int_{-\infty}^{\infty} E(t)e^{iwt}dt \tag{4.48}$$

from which we can calculate the magnitude of the Fourier Transform *E(w)* as

$$|E(w)|^2 \propto \frac{1}{(w - w_0)^2 + \left(\frac{w_0}{2Q}\right)^2} \tag{4.49}$$

So in frequency domain, the resonance has Lorentzian shape and FWHM or Δw is equal to w_0/Q. We can practically calculate Q-factor from frequency domain measurements as:

$$Q = \frac{w_0}{\Delta w} = \frac{f_0}{\Delta f} \tag{4.50}$$

where $f_0 = w_0/2\pi$ and Δf is FWHM of resonance peak. Line shape of the resonance peak can be measured scanning the wavelength of the tunable laser coupled to cavity. In fact, line shape is actually a convolution of laser's line shape and cavity's line shape, which are both Lorentzian. Since the convolution of two Lorentzian line shape is also a Lorentzian line shape with a FWHM, which is sum of FWHM of laser and cavity line shape. True FWHM is therefore given as

$$FWHM_{WGM} = FWHM_{measurement} - FWHM_{laser} \tag{4.51}$$

For our case we ignore FWHM of laser (0.004 pm for $\lambda = 1550\ nm$), which is two orders of magnitude smaller than the experimental wavelength resolution (0.1 pm).

There are basically two loss mechanism resulting into decay of stored energy, intrinsic losses and extrinsic losses, which are caused by cavity related losses such as material absorption, radiation loss, scattering and contamination loss, and coupling loss due to coupling of the light back into the coupler, respectively. Therefore energy decay rate is sum of intrinsic and extrinsic decay rates, which is in other terms:

$$\frac{1}{Q} = \frac{-\frac{dU}{dt}}{w_0 U} = \frac{-\frac{dU_{in}}{dt}}{w_0 U} + \frac{-\frac{dU_{ex}}{dt}}{w_0 U} \tag{4.52}$$

Thus,

$$\frac{1}{Q} = \frac{1}{Q_{in}} + \frac{1}{Q_{ex}} \tag{4.53}$$

where Q_{ex} is the coupling Q-factor. In a similar fashion, intrinsic Q-factor can be decomposed to:

$$\frac{1}{Q_{in}} = \frac{1}{Q_{mat}} + \frac{1}{Q_{scat}} + \frac{1}{Q_{rad}} + \frac{1}{Q_{cont}} \tag{4.54}$$

The *Q*-factor resulted from material absorption is given as [61]:

$$Q_{mat} = \frac{2\pi n}{\alpha\lambda} \tag{4.55}$$

where α is material absorption coefficient. The scattering related *Q*-factor is [61]:

$$Q_{scat} = \frac{\lambda^2}{2\pi^2\sigma^2 B} \tag{4.56}$$

where σ and B are the root mean square (rms) size and the correlation length of surface roughness.

Radiation losses are caused by the tunneling of light from the cavity due to its finite dielectric constant and curvature of its surface. Radiation loss related Q-factor is given by [62, 63]

$$Q_{rad} = \frac{1}{2}\left(l + \frac{l}{2}\right) n^{1-2b}(n^2 - 1)^{\frac{1}{2}} e^{2T_l} \tag{4.57}$$

where

$$T_l = \left(l + \frac{1}{2}\right)(n_l - tanh\eta_l) \tag{4.58}$$

$$\eta_l = arcosh\left\{ n\left[1 - \frac{1}{l + \frac{1}{2}}\left(\alpha_q\left(\frac{1}{2}\left(l + \frac{1}{2}\right)\right)^{\frac{1}{3}} + \frac{l^{1-2b}}{\sqrt{l^1 - 1}}\right)\right]^{-1}\right\} \tag{4.59}$$

and b = 0 for TE modes and b = 1 for TM modes. Q_{rad} is generally very high (>10^{10}) and is a decisive parameter among other *Q*-factors only for spheres of small radius (a < 10 μm).

Chapter 5

Optical Coupling to WGMs

5.1. Introduction

WGM resonators have very desirable properties such as ultrahigh *Q*-factors and small mode volumes. However, technological exploitation of these resonators is only possible if light can be efficiently and controllably coupled in and out of these WGMs. Required assets for an ideal optical coupler are 1) phase matching, 2) spatial field overlap, 3) ideality, which accounts for amount of parasitic coupling to unwanted modes, and 4) critically, which implies 100% energy exchange at resonance. Besides, low cost fabrication and easy alignment of couplers can be considered to be other important factors. The only approach that fulfills all these requirements is the utilization of phase matched optical couplers, which depend on frustrated total internal reflection (TIR) mechanism as used in prism couplers, and near field evanescent coupling as used in tapered fibers or integrated waveguides. Free space beams [64] do not efficiently couple into WGMs, therefore they will not be considered further.

Prism couplers [65] are the earliest methods to couple light into WGMs of resonators. A laser beam directed into a prism can be coupled into WGMs of a resonator via frustrated TIR mechanism if the resonator is close enough to the prism surface. Phase matching is obtained adjusting the incidence angle of the beam. However, system is bulky, and optimal alignment and control of separation between prims and resonator is quite challenging. Nevertheless, a coupling efficiency of 80% was reported up to date [66].

The integrated waveguide couplers [67] can couple light through a phase matched waveguide whose evanescent field overlaps with that of WGMs. Achieving a critical

coupling is difficult and requires fine alignment, but the system is rather robust and compact.

The fiber-prism coupler [68] couples core guided light into WGMs via frustrated TIR mechanism at the fiber end, which is polished with a specific angle satisfying phase matching condition. It combines the benefits of prism coupling and waveguide light insertion, and do not require any alignment. However, fabrication of the fiber with proper angled tip is not an easy task.

The most efficient couplers ever found to date is tapered fibers, which enables almost 100% energy transfer to WGMs of microspheres at critical coupling [69] and shows high ideality [70]. Phase matching condition can be satisfied tuning the radius of tapered region. Coupling loss can be tuned by changing the separation between the cavity and the tapered fiber for reaching the critical coupling point. Tapered fibers can be easily fabricated pulling apart inside a hot zone created by a heating agent such as CO_2 laser or a hydrogen torch. Apart from the coupling efficiency, probably other most significant advantage of using tapered fibers is their intrinsic focusing of guided beam and easy alignment with respect to resonator perimeter. Coupling light out using the same fiber itself is also a convenient compatibility for the integration to external systems. Disadvantages of tapered fibers are their fragile nature and their limited applicability which excludes coupling to resonators made of materials with higher refractive index than that of silica [71].

Due to the aforementioned superior properties of tapered fiber, this chapter is devoted to the theoretical understanding of coupling between microsphere and tapered fibers, fabrication of tapered silica fibers, and experimental details of optical coupling and characterization.

5.2. Optical Modes of Step-Index Fiber Waveguide

A cavity resonator coupled to a tapered fiber is generally positioned close to a region where radius of tapered fiber is minimum and locally constant over some distance along the fiber between transition regions. In this region of constant radius, tapered fibers can be treated as step-index cylindrical waveguides to simplify theoretical arguments and ease the understanding of optical coupling to WGMs.

The fields of the step-index fiber in cylindrical coordinates are calculated by solving the wave equation [72], which is Helmholtz equation for time harmonic fields. If the direction of the wave propagation taken to be the z-direction, and longitudinal field components are in the form:

$$(E_z\,, H_z) = \psi(r,\theta)e^{-i\beta z}e^{iwt} \qquad l = 0, 1, 2, \ldots, \tag{5.1}$$

the wave equation in the longitudinal direction is

$$\left(\frac{\partial^2}{\partial r^2} + \frac{1}{r}\frac{\partial}{\partial r} + \frac{1}{r^2}\frac{\partial^2}{\partial \theta^2} + (k^2 - \beta^2)\right)\psi(r,\theta) = 0 \tag{5.2}$$

The solutions are separable if we use the ansatz, $\psi(r,\theta) = \mathcal{R}(r)e^{\mp il\theta}$, and $\mathcal{R}(r)$ satisfies the Bessel differential equation :

$$\frac{\partial^2 \mathcal{R}}{\partial r^2} + \frac{1}{r}\frac{\partial \mathcal{R}}{\partial r} + (k^2 - \beta^2 - \frac{l^2}{r^2})\mathcal{R} = 0 \tag{5.3}$$

For the modes to be confined and finite, the solutions take the form

$$\begin{aligned} \mathcal{R}(r) &= CJ_l(hr), \qquad k^2 - \beta^2 > 0 \\ &= CK_l(qr), \qquad k^2 - \beta^2 < 0 \end{aligned} \tag{5.4}$$

where $h^2 = k^2 - \beta^2$ and $q^2 = \beta^2 - k^2$.

The step-index fibers have a circular refractive index profile *n(r)*

$$\begin{aligned} n(r) &= n_1\,, \qquad r < R_f \\ &= n_2\,, \qquad r > R_f \end{aligned} \tag{5.5}$$

where R_f is the radius of the core. The exact solutions for core ($r<R_f$) are:

$$\begin{aligned} E_r &= -\frac{i\beta}{h^2}\left(AhJ_l'(hr) + \frac{i\omega\mu l}{\beta r}BJ_l(hr)\right)\cos(\omega t + l\theta - \beta z) \\ E_\theta &= \frac{\beta}{h^2}\left(\frac{il}{r}AJ_l(hr) - \frac{\omega\mu}{\beta}BhJ_l'(hr)\right)\sin(\omega t + l\theta - \beta z) \\ E_z &= AJ_l(hr)\cos(\omega t + l\theta - \beta z) \end{aligned} \tag{5.6}$$

$$\begin{aligned} H_r &= \frac{\beta}{h^2}\left(BhJ_l'(hr) - \frac{i\omega\epsilon_1 l}{\beta r}AJ_l(hr)\right)\sin(\omega t + l\theta - \beta z) \\ H_\theta &= -\frac{i\beta}{h^2}\left(\frac{il}{r}BJ_l(hr) + \frac{\omega\epsilon_1}{\beta}AhJ_l'(hr)\right)\cos(\omega t + l\theta - \beta z) \\ H_z &= BJ_l(hr)\cos(\omega t + l\theta - \beta z) \end{aligned} \tag{5.7}$$

and for cladding ($r>R_f$)

$$\begin{aligned} E_r &= \frac{i\beta}{q^2}\left(CqK_l'(qr) + \frac{i\omega\mu l}{\beta r}DK_l(qr)\right)\cos(\omega t + l\theta - \beta z) \\ E_\theta &= \frac{\beta}{q^2}\left(\frac{il}{r}CK_l(qr) - \frac{\omega\mu}{\beta}DqK_l'(qr)\right)\sin(\omega t + l\theta - \beta z) \\ E_z &= CK_l(qr)\cos(\omega t + l\theta - \beta z) \end{aligned} \tag{5.8}$$

$$\begin{aligned} H_r &= -\frac{\beta}{q^2}\left(DqK_l'(qr) - \frac{i\omega\epsilon_2 l}{\beta r}CK_l(qr)\right)\sin(\omega t + l\theta - \beta z) \\ H_\theta &= \frac{i\beta}{q^2}\left(\frac{il}{r}DK_l(qr) + \frac{\omega\epsilon_2}{\beta}CqL_l'(qr)\right)\cos(\omega t + l\theta - \beta z) \\ H_z &= DK_l(qr)\cos(\omega t + l\theta - \beta z) \end{aligned} \tag{5.9}$$

where the tangential components of electric field are real and longitudinal components are imaginary as a convention. Therefore A and C must be imaginary, and B and D must be real.

Applying continuity boundary conditions on the fiber cladding interface, characteristic equations can be written, whose roots are propagations constants. Generally there are two types of modes, *HE* and *EH*. Since all of their field components are nonzero, they are hybrid modes.

The characteristic equation for *EH* modes are:

$$\frac{J_{l+1}(hR_f)}{hR_f J_l(hR_f)} = \frac{n_1^2 + n_2^2}{2n_1^2}\frac{K_l'(qR_f)}{qR_f K_l(qR_f)} + \frac{l}{(hR_f)^2} - P \tag{5.10}$$

and for *HE* modes are:

$$\frac{J_{l-1}(hR_f)}{hR_f J_l(hR_f)} = -\frac{n_1^2 + n_2^2}{2n_1^2}\frac{K_l'(qR_f)}{qR_f K_l(qR_f)} + \frac{l}{(hR_f)^2} - P \tag{5.11}$$

where

$$P = \sqrt{\left(\frac{n_1^2 - n_2^2}{2n_1^2}\right)^2 \left(\frac{K_l'(qR_f)}{qR_f K_l(qR_f)}\right)^2 + \left(\frac{l\beta}{n_1 k_0}\right)^2 \left(\frac{1}{(hR_f)^2} + \frac{1}{(qR_f)^2}\right)^2} \tag{5.12}$$

The number of roots depends on the size of the fiber and refractive index difference, however, there is always one fundamental mode HE_{11} propagating through the fiber waveguide. For fibers with very small radius, most of the field is evanescent.

5.3. Numerical Simulation of Fiber Modes

In order to find electric field distributions, we performed simulations using three dimensional finite element method (FEM) with COMSOL Wave Optics Module (electromagnetic waves, beam envelope interface). Simulation environment consists of 1.8 μm radius 15 μm long fiber with refractive index n_f of 1.44, an air shell (n_{air} = 1) and perfect electric conductor (PEC) layer as shown in Figure 5.1. Working wavelength λ is 1.55 μm. Air region has thickness of λ. Maximum mesh size for cross sections are chosen λ/15 for fiber and λ/5 for air shell region. Mesh size for longitudinal direction is 3λ. Mesh distribution can be also seen in Figure 5.1.

In beam envelope study type, high spatial frequency component of electric field for propagation direction $\vec{k}_1$ is written explicitly as:

$$\vec{E}(r) = \vec{E}_1(r)e^{-i\vec{k}_1 \cdot \vec{r}} \tag{5.13}$$

where $\vec{E}_1(r)$ is envelope function. Inserting this electric formulation into Maxwell's equation, results in the following wave function:

$$(\nabla - i\vec{k}_1) \times \left((\nabla - i\vec{k}_1) \times \vec{E}_1(r)\right) - k^2\vec{E}_1(r) = 0 \tag{5.14}$$

where $k=k_0 n$ and $k_0=w/c$. FEM solution for fundamental mode HE_{11} is given in Figure 5.2. Propagation constants calculated from FEM simulations and characteristic Equation 5.11 are given for comparison in Table 5.1. Electric field distributions for different modes are given in Figure 5.3.

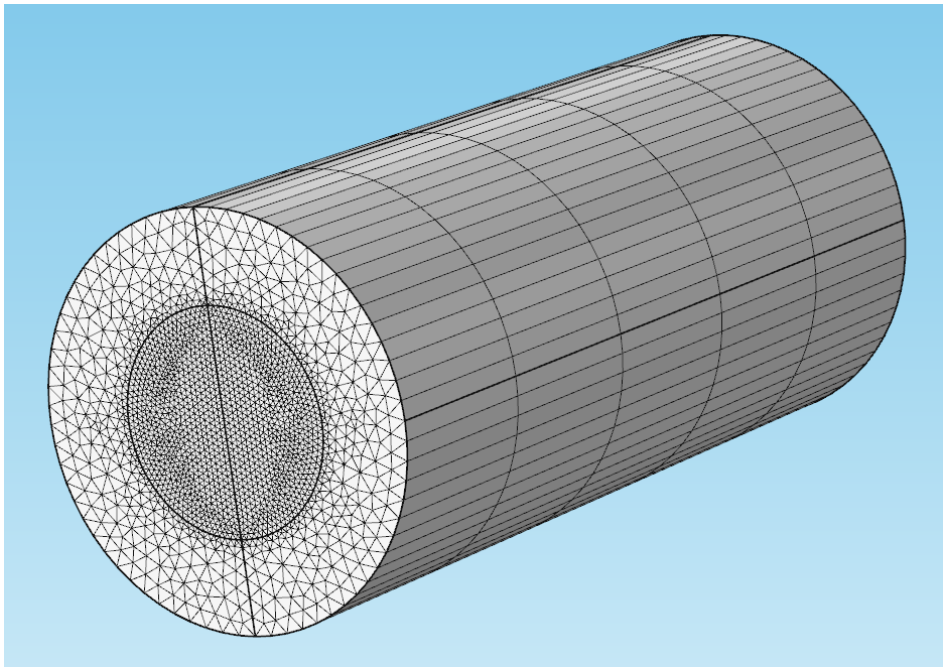

Figure 5.1: Mesh distribution of a fiber waveguide with air cladding. Simulation parameters are : R_f = 1.8 µm, L = 15 µm, n_f =1.44, λ = 1.55 µm.

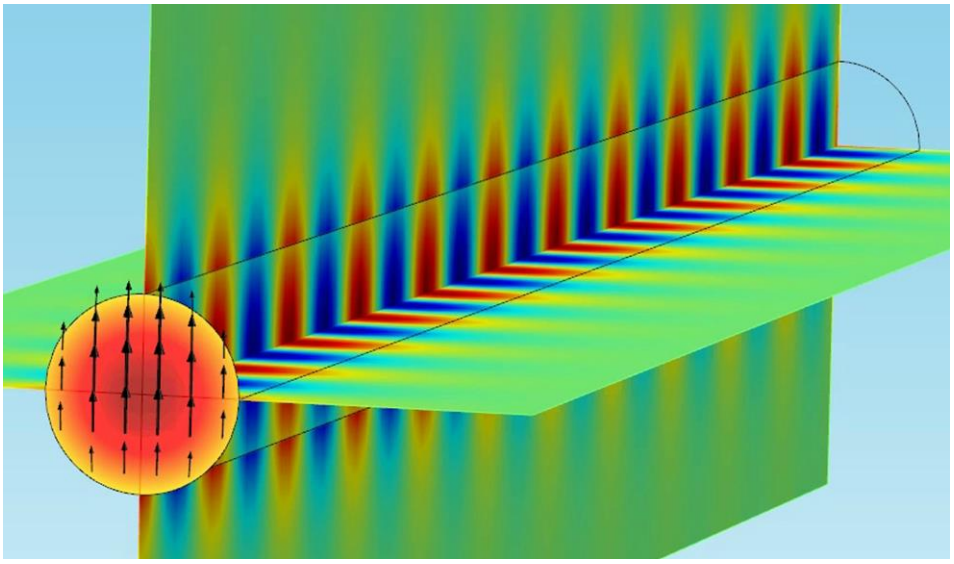

Figure 5.2: Simulation result for the fundamental mode HE_{11} propagating along the fiber waveguide.

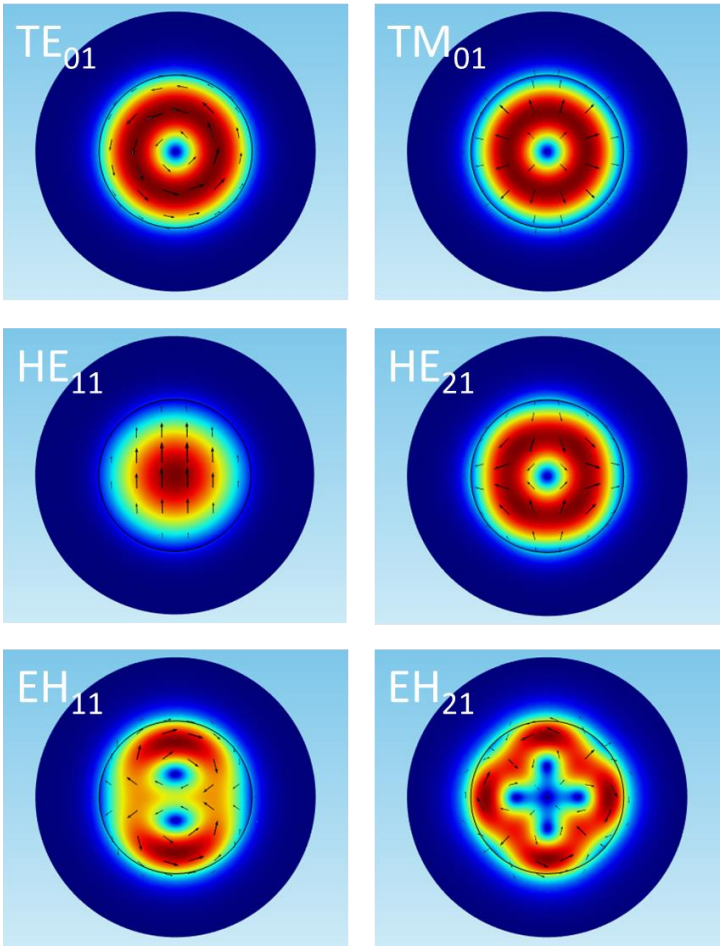

Figure 5.3: Electric field magnitudes and vector fields in cross section for some fiber guided modes.

TE/TM	HE_{1n}	HE_{2n}	EH_{1n}	HE_{3n}	EH_{2n}	β (10^6 m^{-1}) (Exact)	β (10^6 m^{-1}) (FEM)
	HE_{11}					5.70852	5.70852
TE_{01}						5.52879	5.52878
		HE_{21}				5.50387	5.50386
TM_{01}						5.48988	5.48989
			EH_{11}			5.25528	5.25527
				HE_{31}		5.22249	5.22249
	HE_{12}					5.12826	5.12827
					EH_{21}	4.92304	4.92302

Table 5.1: Comparison of FEM and exact results for propagation constants of some modes.

5.4. Theory of Optical Coupling for the Sphere Cavity and Fiber System

Optical coupling depends critically on two parameters: spatial overlap of the fiber modes and sphere modes (see Figure 5.4(a)), and the phase-matching between them. Coupling strength can be described by a coupling coefficient *r*, which is given by the coupled mode theory as [73]:

$$r = \frac{w\epsilon_0}{4}(n_s^2 - n_0^2)N_f N_s \iiint_{V_s} \left(\vec{E}_f^t \cdot \vec{E}_s^t + E_f^z E_s^z\right) e^{i\Delta\beta z} dxdydz \tag{5.15}$$

where longitudinal E^z and transverse components E^t of electric fields are written explicitly, $\Delta\beta = \beta_f - \beta_s$ is difference between propagation constants of modes, V_s is the volume of the sphere cavity, N_f and N_s are factors that normalize the power of fiber and sphere modes, respectively. The coupling parameter *r* represent coupling from fiber to sphere. Similarly coupling from sphere to fiber is represented by *r'*, and transmission coefficients are *p* and *p'* as shown in a schematic of coupling between fiber waveguide and microsphere cavity in Figure 5.4(b).

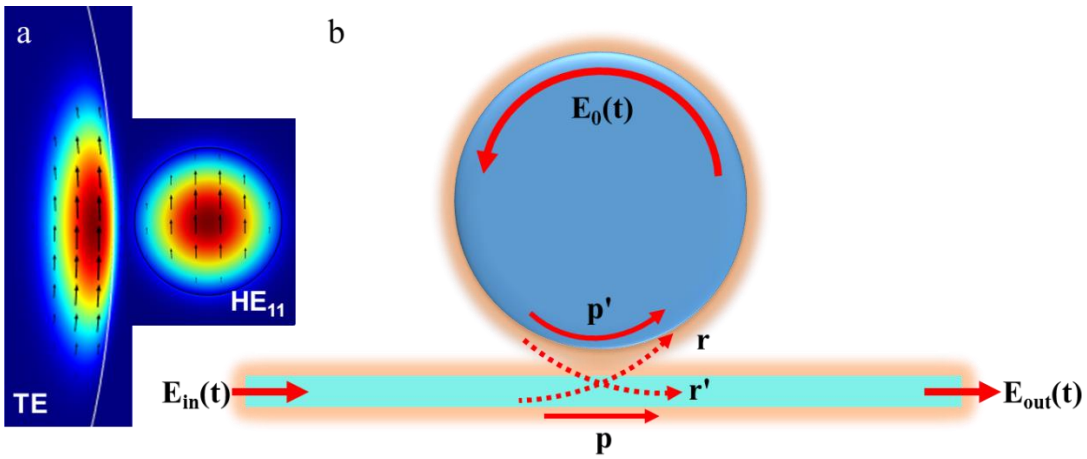

Figure 5.4: (a) Cross section of the coupling region. (b) Schematic of a tapered fiber evanescently coupled to WGM of a microsphere.

The phase matching implies the similarity between the propagation constants or effective refractive indices n_{eff} , which is related to the propagation constant β *by*;

$$\beta = \frac{\omega}{c} n_{eff} \tag{5.16}$$

where ω is angular frequency of light and c is the speed of light in the vacuum. Therefore, the propagation constant difference can be calculated as

$$\Delta\beta = \frac{\omega}{c}\left(n_{eff,f} - n_{eff,s}\right) \tag{5.17}$$

where $n_{eff,f}$ and $n_{eff,s}$ are effective indices for the modes in the fiber waveguide and the sphere microresonator, respectively. Propagation constant of a silica fiber for the fundamental mode HE_{11} can be calculated using [74]

$$\beta^2 = k^2 {n_f}^2 - 2.405^2 / r_f^2 \tag{5.18}$$

where k is the wave vector in air, n_f and r_f are the refractive index of the bulk silica $n_f = 1.44$ and the radius of the taper waist, respectively. After propagation constants are calculated for different tapered fiber radii, they can converted into effective refractive index $n_{eff,f}$ using Equation 5.16. Effective refractive index $n_{eff,s}$ of the microsphere resonator can be calculated for each *WGM(q, l, m)* mode by using $n_{eff,s} \cong l/x_{q,l}$, where q is radial mode number, l is angular mode number, and $x_{q,l} = k_l r_s$ is the size parameter of the sphere microresonator given by Equation 4.34.

In order to calculate effective refractive indices of tapered silica fiber and chalcogenide microresonators, a MATLAB code was developed. For a sphere microresonator, polar mode numbers l corresponding to resonance wavelengths in an experimental scan range, are first computed for different radial mode orders q and resonator radii r_s by using Equation 4.34. Following the determination of l values, $n_{eff,s}$ are calculated as a function of radial mode order q and resonator radius r_s.

Phase matching is important for optimal light coupling. Smaller the difference between the propagation constants or effective refractive indices, higher the phase matching; therefore, better optical coupling can be obtained. As seen in Figure 5.5, the effective refractive index of resonator for fundamental modes (q = 1) approaches to the effective refractive index of the silica fiber with an increasing trend for smaller radii (or size parameters). Also for higher radial mode orders (q > 1), the difference between the effective refractive indices of resonator and fiber exponentially decreases for very small resonator radii r_s. This explains why higher mode orders couples into the resonators much more favorably then the lower mode orders.

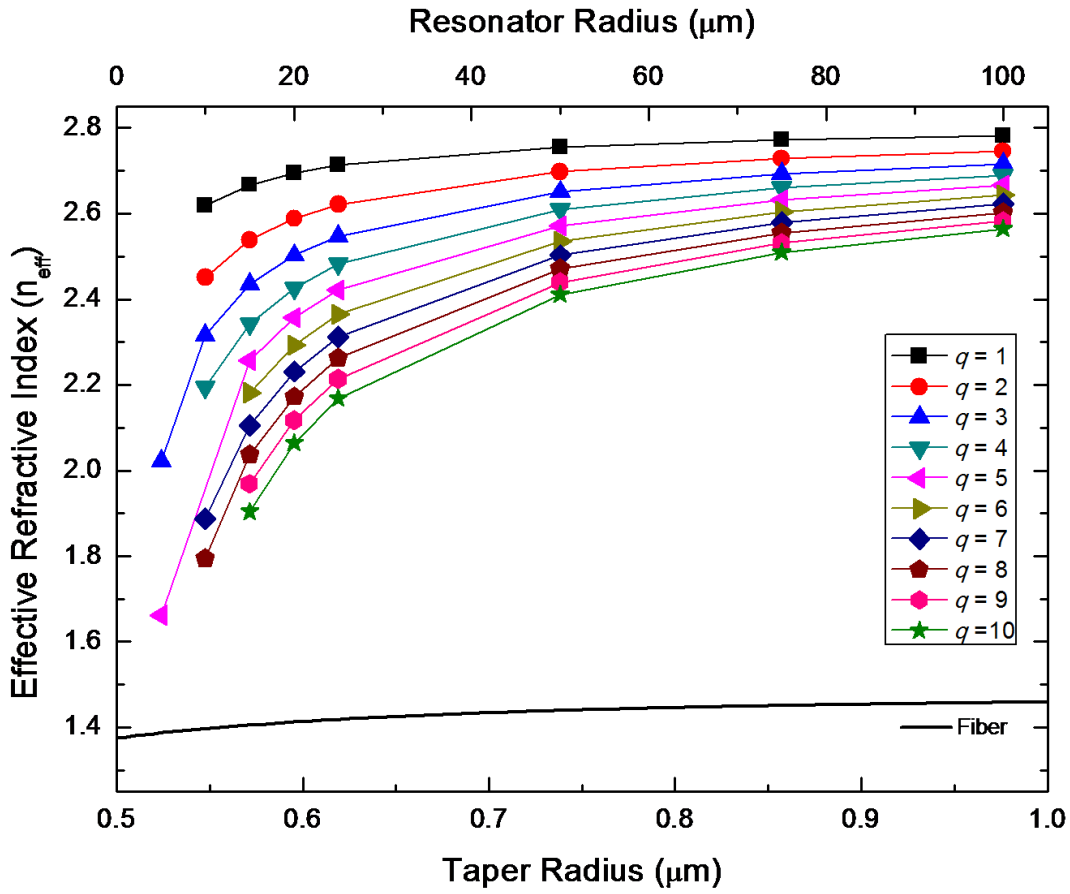

Figure 5.5: The effective refractive indices $n_{eff,s}$ of chalcogenide microspheres with various sizes for different modes of radial orders (q = 1, 2, 3 … 10), and effective refractive indices $n_{eff,f}$ of tapered silica fiber with respect to its waist radius (for fundamental HE_{11} mode). Radius of the microresonator is R = 25 μm.

In addition, achieving a smaller taper radius than the exact phase-matching taper radius can enhance the optical coupling since the decreased radius increases the evanescent field of the fiber which overcomes the negative effect of phase-mismatch and enhances the coupling up to a certain point where phase-mismatch recovers its dominance over the optical coupling again. Therefore, the optimal radius for maximum coupling strength is lower than the radius satisfying exact phase matching condition. Coupling coefficient depends on the spatial overlap of the fiber and sphere modes, so changing distance between the fiber and the sphere will change the coupling coefficient enabling tuning of coupling strength, which is not possible in Fabry-Perot resonators.

Evolution of optical coupling in fiber wave guide and sphere microcavity system can be analyzed by scattering matrix formalism [66, 75, 76]. Assuming only HE_{11} mode is traveling along the fiber through the coupling region as shown in Figure 5.4 and only a fundamental TE or TM mode of the sphere with (q = 1, l = m) mode orders is exited, the relations between pump field $E_{in}(t)$ and circulating field $E_0(t)$ inside the sphere and the transmitted field $E_{out}(t)$ can be written as:

$$E_0(t) = p' E_0(t - \tau_0) e^{\left(i\varphi - \frac{\alpha L}{2}\right)} + irE_{in}(t) \tag{5.19}$$

and

$$E_{out}(t) = pE_{in}(t) + ir' E_0(t) \tag{5.20}$$

where $\tau_0 = n_s L/c_0$ is circulating time for mode traveling inside the sphere, $L = 2\pi R_s$ is perimeter of the sphere, $\varphi = 2\pi n_s L/\lambda$ is the phase lag after one circulation inside the sphere, n_s is index of sphere, c_0 is the speed of light, and α is the intrinsic loss coefficient in the sphere cavity caused by scattering, absorption, radiation, and etc. The time reversal symmetry and energy conservation lead to $r = r'$, $p = p'$, and $|p|^2 + |r|^2 = 1$. If we assume the sphere cavity is a high Q-factor resonator and intrinsic and coupling losses are very small, this means $\alpha \ll 1$ and $|r| \ll 1$. For a resonance frequency $w = 2\pi c_0/\lambda_o$, frequency detuning from resonance frequency w_0 can be written as

$$\Delta w = w - w_0 = 2\pi c_0 \left(\frac{1}{\lambda} - \frac{1}{\lambda_0}\right) \approx 2\pi c_0 \frac{-\Delta\lambda}{\lambda_0^2} \tag{5.21}$$

And we also have

$$\begin{aligned} \varphi = \frac{2\pi n_s L}{\lambda} &= 2\pi n_s L \left(\frac{1}{\lambda} - \frac{1}{\lambda_0} + \frac{1}{\lambda_0}\right) = 2\pi n_s L \frac{-\Delta\lambda}{\lambda_0^2} + \frac{2\pi n_s L}{\lambda_0} \\ &= 2\pi n_s L \frac{-\Delta\lambda}{\lambda_0^2} + 2\pi N \end{aligned} \tag{5.22}$$

where N is a integer and we use resonance condition $n_s L = N\lambda_0$ in the last term. Combining Equation 5.21 and Equation 5.22, we have

$$\varphi = \frac{n_s}{c_0} \Delta w + 2\pi N$$

So we

$$\exp\left(i\varphi - \frac{\alpha L}{2}\right) = \exp\left(i \frac{n_s L}{c_o} \Delta w - \frac{\alpha L}{2}\right) = 1 + i \frac{n_s L}{c_o} \Delta w - \frac{\alpha L}{2} \tag{5.23}$$

where we use Taylor expansions in the last term. Putting Equation 5.23 into Equation 5.19, neglecting second order terms and using Taylor expansion again for circulating field

$$E_0(t-\tau_0) = E_0(t) - \tau_0 \frac{dE_0}{dt} \tag{5.24}$$

finally we obtain:

$$\frac{dE_0(t)}{dt} + \left(\frac{1-p}{p\tau_0} + \frac{c_0\alpha}{2n_s} - i\Delta w\right) E_0 = i\frac{r}{\tau_0} E_{in}(t) \tag{5.25}$$

Defining intrinsic and coupling Q-factors as:

$$\frac{w_0}{2Q_{in}} = \frac{c_0\alpha}{2n_s} \tag{5.26}$$

$$\frac{w_0}{2Q_{coup}} = \frac{1-p}{p\tau_0} \approx \frac{r^2}{2\tau_0} \tag{5.27}$$

thus, Equation 5.25 becomes

$$\frac{dE_0(t)}{dt} + \left(\frac{w_0}{2Q_{in}} + \frac{w_0}{2Q_{coup}} - i\Delta w\right) E_0 = i\frac{r}{\tau_0} E_{in}(t) \tag{5.28}$$

For steady state solutions, we can drop derivative term and obtain

$$E_o(t) = \frac{ir/\tau_0}{\frac{w_0}{2Q_{coup}} + \frac{w_0}{2Q_{in}} - i\Delta w} E_{in}(t) \tag{5.29}$$

Therefore, we can deduce the transmission coefficient of the coupled system by using Equation 5.29 and 5.20, and $p \approx 1$, which is a Lorentzian function:

$$T = \frac{|E_{out}(t)|^2}{|E_{in}(t)|^2} = 1 - \frac{{w_0}^2/Q_{in}Q_{coup}}{\left(\left[\frac{1}{Q_{in}} + \frac{1}{Q_{coup}}\right]\frac{w_0}{2}\right)^2 + \Delta w^2} \tag{5.30}$$

The transmission coefficient T can be rewritten in terms of experimentally available quantities as

$$T = 1 - \frac{K}{\left[2Q_L \frac{(w - w_0)}{w_0}\right]^2 + 1} \tag{5.31}$$

where K is the transmission depth at resonance frequency and Q_L is the loaded quality factor, which are given by

$$K = \frac{4Q_{in}Q_{coup}}{\left(Q_{in}+Q_{coup}\right)^2} \tag{5.32}$$

$$1/Q_L = 1/Q_{coup} + 1/Q_{in} \tag{5.33}$$

For full transmission spectrum containing M resonance peaks of w_i, transmission is given by

$$T = 1 - \sum_{i=1}^{M} \frac{K_i}{\left[2Q_{L,i} \frac{(w - w_i)}{w_i}\right]^2 + 1} \tag{5.34}$$

where K_i and $Q_{L,i}$ are transmission depth and loaded quality factor of corresponding resonance peaks w_i. See Figure 5.6 and Table 5.2 for a simulated transmission spectra of a 25 μm radius sphere, and Appendix A.1 for MATLAB codes.

Intrinsic quality factor Q_{in} and coupling quality Q_{coup} factor can also be written in terms of K an Q_L as:

$$Q_{in} = 2Q_L\left[1 + \sqrt{1 - K}\right]/K \tag{5.35}$$

$$Q_{coup} = 2Q_L\left[1 - \sqrt{1 - K}\right]/K \tag{5.36}$$

Q_{in} is generally fixed by fabrication. However, Q_{coup} can be change by adjusting the separation between fiber and sphere cavity. So depending on the ratio of $\delta = Q_{in}/Q_{coup}$, three coupling regimes are possible: over-coupling $\delta > 1$, critical coupling ($\delta = 1$) and under-coupling ($\delta < 1$). Maximum power transfer can achieved in critical coupling where transmission drops to zero.

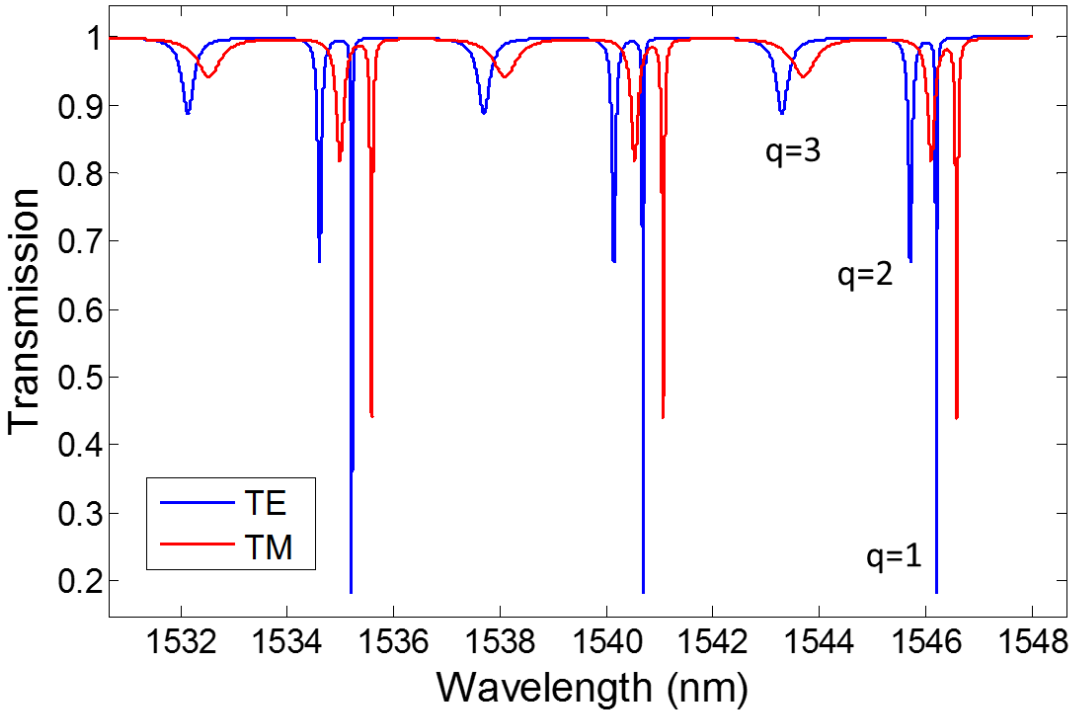

Figure 5.6: TE and TM WGM modes for a sphere of 25 µm radius with n_s = 2.79.

TM	q	l=m	λ (nm)	Q_{coup}	TE	q	l=m	λ (nm)	Q_{coup}
	1	273	1535.6			1	274	1535.2	
	1	272	1541.1	2×10^4		1	273	1540.7	4×10^4
	1	271	1546.6			1	272	1546.2	
	2	264	1535.0			2	265	1534.6	
	2	263	1540.5	5×10^3		2	264	1540.2	1×10^4
	2	262	1546.1			2	263	1545.7	
	3	257	1652.5			3	258	1532.1	
	3	256	1538.2	1.5×10^3		3	257	1537.7	3×10^3
	3	255	1543.7			3	256	1543.3	

Table 5.2: Simulation parameters for the calculation of WGM modes. Q_{in} =10^5 is taken same for all modes.

5.5. Fabrication of Tapered Optical Fibers

Although it is possible to fabricate tapered silica fibers by etching with HF [77], single mode silica fibers are more conveniently tapered by pulling them apart with two controller driven linear translation stages moving towards opposite directions, while being heated up to silica softening temperature in a hot zone created by a heat source. We have tried heating by CO_2 laser, propane/butane mix torch, and hydrogen torch which gives the best results. Total tapering length L (30 mm), length of the hot zone h (5 mm) and tapering speed v (0.005 mm/s) are important parameters for a tapering process. Tapering results into a biconical shapes with a region of constant radius in the middle. Using volume conservation, left part of the symmetric tapered fiber profile in cylindrical coordinate system can be estimated as [78]:

$$\begin{aligned} r(z) &= r_0 e^{-z/h} \qquad 0 < z < L/2 \\ &= r_0 e^{-L/2h} \qquad L/2 < z < (L+h)/2 \end{aligned} \tag{5.37}$$

where $r(z)$ is radius of fiber at z, r_0 is initial fiber radius. Unlike etched fibers, for which only the core of the fiber remains after tapering, the core of the fiber being tapered by heat gradually diminishes, and at some point only the cladding region remains. In the beginning, there is only core-cladding guided fundamental mode HE_{11} of the fiber. Depending on the rate of tapering other higher modes of same symmetry with HE_{11} can be exited in the transition region resulting into beating of modes at the fiber end [79]. With further tapering, fiber transmission reaches a cut-off where only a single air-cladding guided mode survives. In order to prevent or minimize exiting higher modes, fibers need to be tapered very gradually as described by the adiabaticity criteria [80]:

$$\left|\frac{dr}{dz}\right| < \frac{r(\beta_1 - \beta_2)}{2\pi} \tag{5.38}$$

where dr/dz is local change of radius, β_1 and β_2 are propagation constants of the fundamental mode and next higher mode, respectively. In an adiabatically tapered fiber, almost 100% transmission values are observed [81]. Longer tapers provide higher adiabaticity with negligible insertion loss.

The tapering setup, as represented in Figure 5.7 and schematically in Figure 5.8, consists of several electronic, optical and mechanical systems. We used two antagonist linear motion stages (Newport) driven by a motion controller (Newport ESP300). After removing the polymer buffer at some portion of a SMF28 optical fiber and cleaning

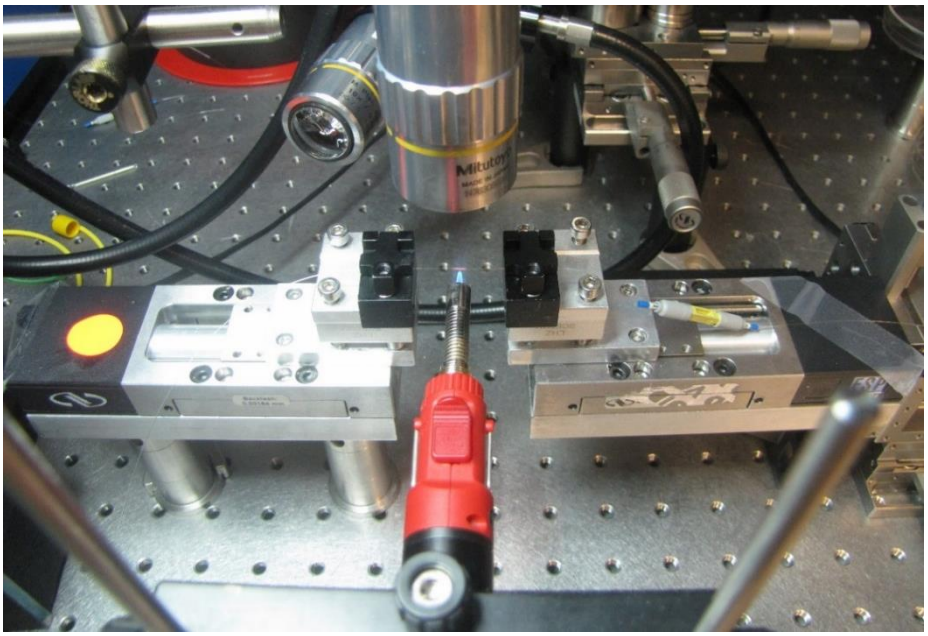

Figure 5.7: Fiber tapering setup used for the fabrication of tapered silica fibers.

the exposed part in an isopropanol alcohol solution to remove polymer residues, the fiber is fixed to the linear motion stages by fiber holders. A tunable laser operating at 1550 nm (Santec TLS-510) is coupled into the fiber at one end using mechanical fiber splicers (Thorlabs) and the other end of the fibers is coupled to the IR detector of a powermeter (Newport 1935C). The pulling length and optical transmission through fiber are continuously monitored in real time and recorded by a custom built software developed in MS Visual Studio .Net 2013 IDE by using C# language. User interface can be seen in Figure 5.9. Laser, powermeter and linear stages are controlled automatically during the tapering process. The tapering fiber is also continuously observed by a CCD camera equipped with a 10X long working distance objective.

We can obtain silica tapered fibers with sub-micron waist diameters (see Figure 5.10) within minutes. Stopping criteria for a tapering process is the observation of the oscillatory transmission signal transforming into a stable signal, indicating only a single optical mode to be guided. Monitoring output signal characteristics enables us to observe adiabaticity of the fibers, which depends on the length of hot zone and alignment of fiber holders. Beating of multi modes for a non-adiabatic tapering can be observed as an increase in amplitude and frequency of oscillations in the transmission signal as shown in Figure 5.11. On the other hand, for an adiabatic tapered fiber, transmission spectra is same before and after tapering, except a constant power drop for all wavelengths as seen in Figure 5.12.

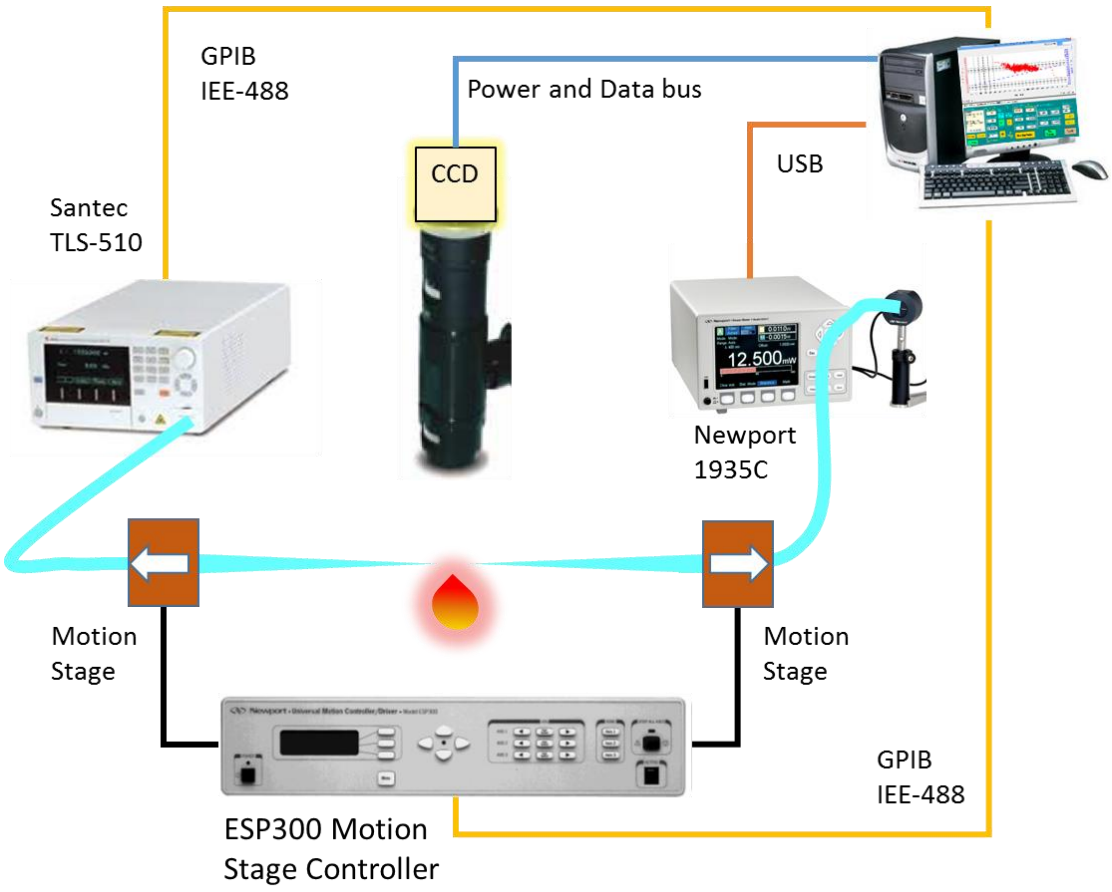

Figure 5.8: Schematic for fiber tapering setup.

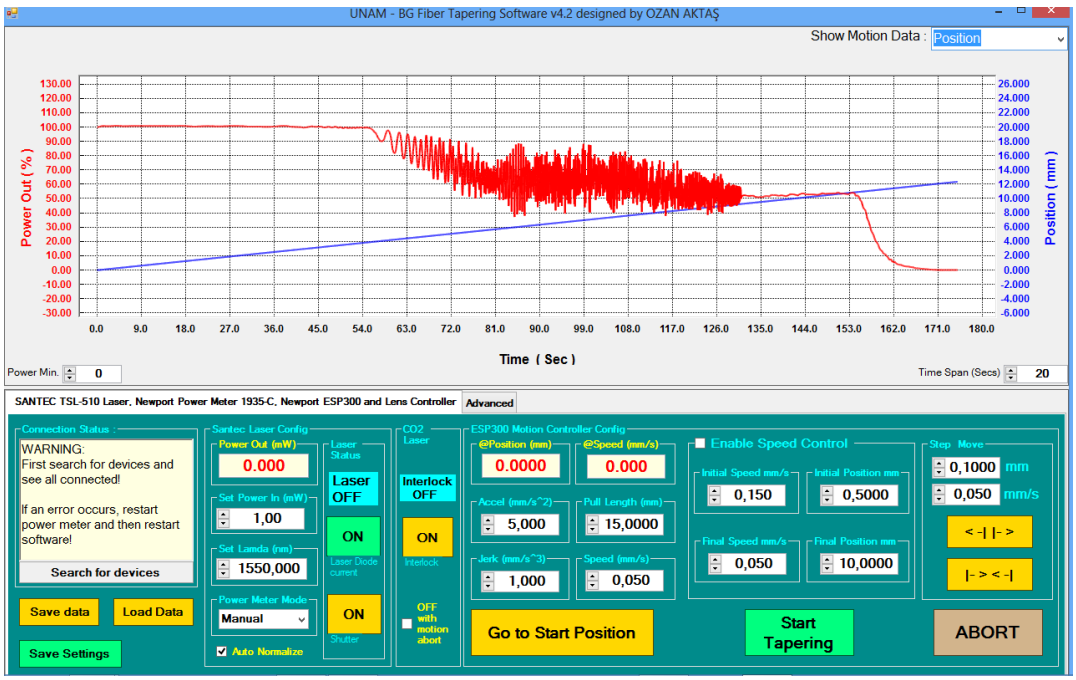

Figure 5.9: User interface of fiber tapering system software.

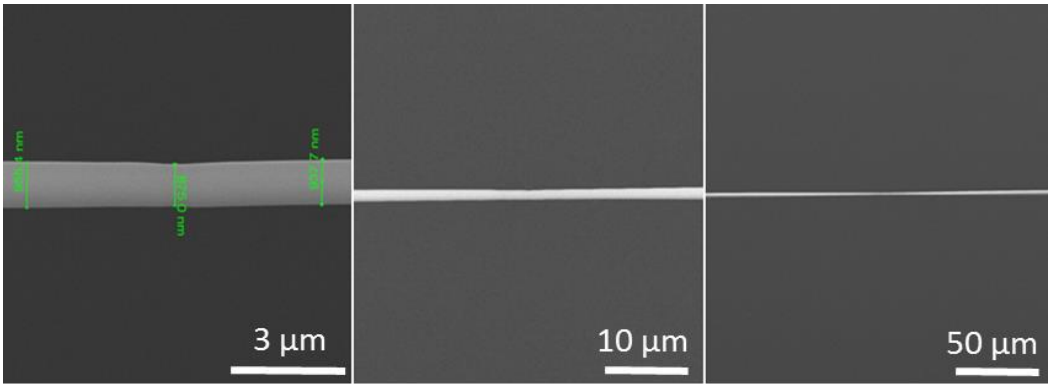

Figure 5.10: SEM images of a tapered fiber fabricated by the tapering setup.

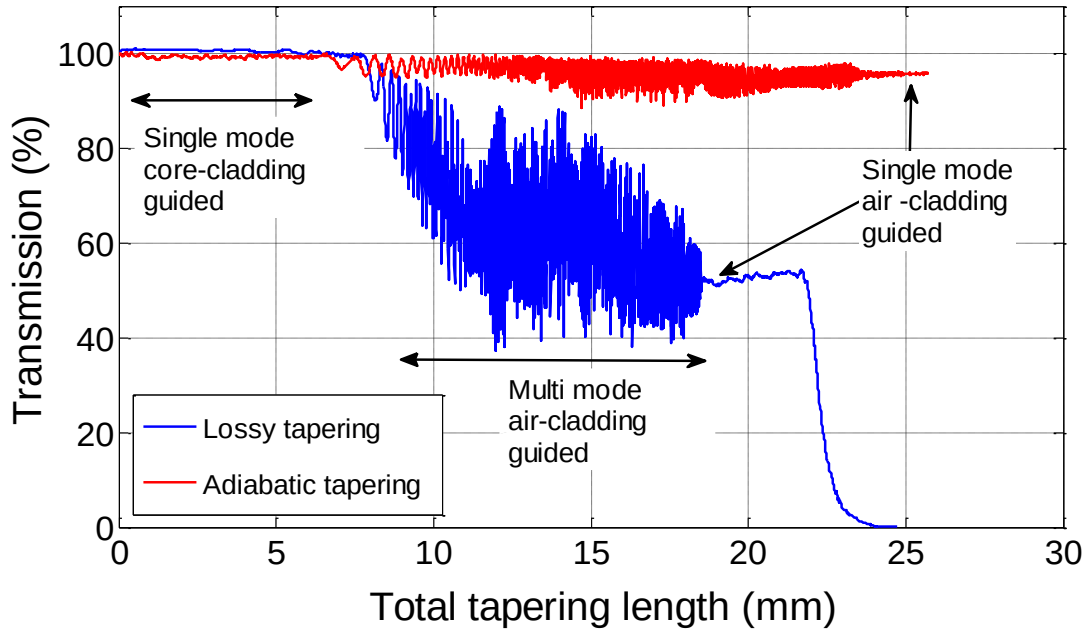

Figure 5.11: Transmission through the optical fiber during fiber tapering. Transmission is given as a function of the total tapering length. Adiabatic and non-adiabatic instances of fiber tapering can recognized from transmission data showing beating of fiber multi-modes observed as oscillations.

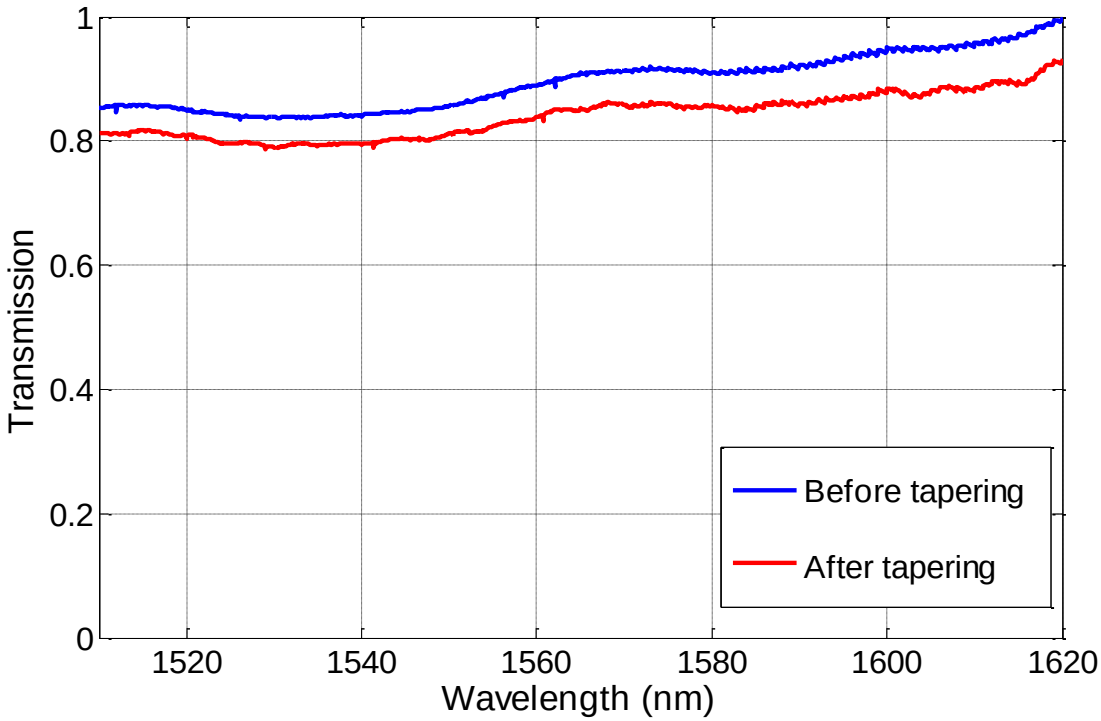

Figure 5.12: Transmission spectra of a silica fiber before and after tapering process with good adiabaticity. Only a parasitic loss is expected for an adiabatic fiber irrespective of the used wavelength. Otherwise, there would be a wavelength dependent transmission dips in the spectra, due to the beating of higher modes with the fundamental mode of the fiber.

5.6. Optical Coupling and Cavity Characterization System

Experimental setup (schematically shown in Figure 5.13) used for the optical characterizations of microresonator consists of an external cavity tunable laser (Santec TLS-510, 500 kHz linewidth, 1500-1630 nm range), a polarization controller, an optical power meter (Newport 1935C with 918D-IR-0D3R detector), an oscilloscope (Tektronix 1012B) , a color CCD camera (Hitachi) with long working distance objective system (Optem Zoom 70XL), and 3-axis closed loop piezo translation stage with controller (BPC303 Controller, NanoMax-TS piezo stage with 5 nm position resolution) which is not shown in the figure.

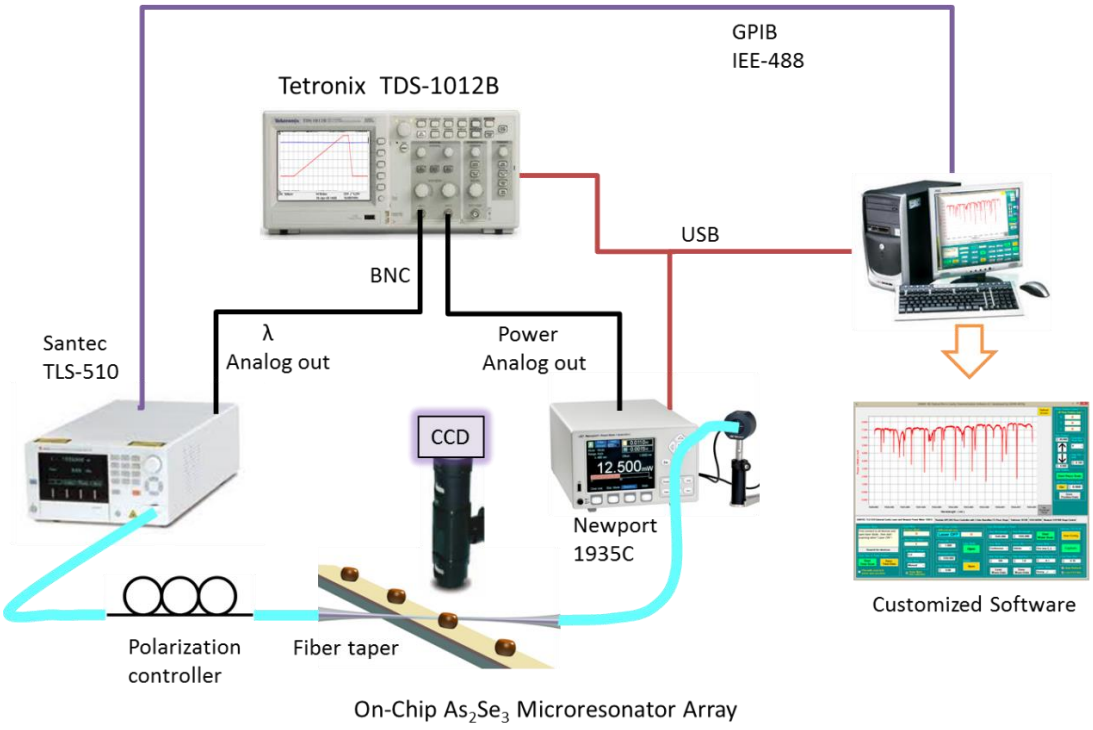

Figure 5.13: Schematics of experimental setup used for the optical characterization of microresonators.

In order to begin optical characterizations, one of the resonators in the microresonator array is positioned by the piezo stage close to a tapered fiber assuring alignment with the equator of resonator (see Figure 5.14), and polarization was adjusted for optimum light coupling. Laser wavelength can be scanned continuously for a desired wavelength range up to 100 nm with scan rates from 1 nm/s to 100nm/s. For single mode measurements, we set scan range as 50 pm and scan rate as 1 nm/s in

order to increase wavelength resolution (sub-picometer). First channel (X axis) of the oscilloscope is connected to analog output port of external cavity laser producing a chain of triangular voltage pulses corresponding to the wavelength scan range and second channel (Y axis) is connected to output port of optical power meter to measure the transmission. Using acquisition of dual channel data in X-Y format provides optical transmission spectrum of microcavity under test.

Optical characterization of microcavities is managed by a custom developed software written in C# programing language using MS. Visual Studio .Net 2013 IDE. The user interface can be seen in Figure 5.15. The software handles data acquisition from the oscilloscope reading wavelength and power channels and implementing a calibration process where a linear fit to the wavelength channel is used to find start and stop wavelength data points in the time axis (see Figure 5.16). After calibration of both axis, data can be plotted in wavelength (nm) vs. power (W) format by the software during data acquisition. The software also adjust configuration settings, manage communications with devices using data buses shown in Figure 5.13 as well as data acquisition from 3 axis piezo stage and optic spectrum analyzer (OSA Q8384).

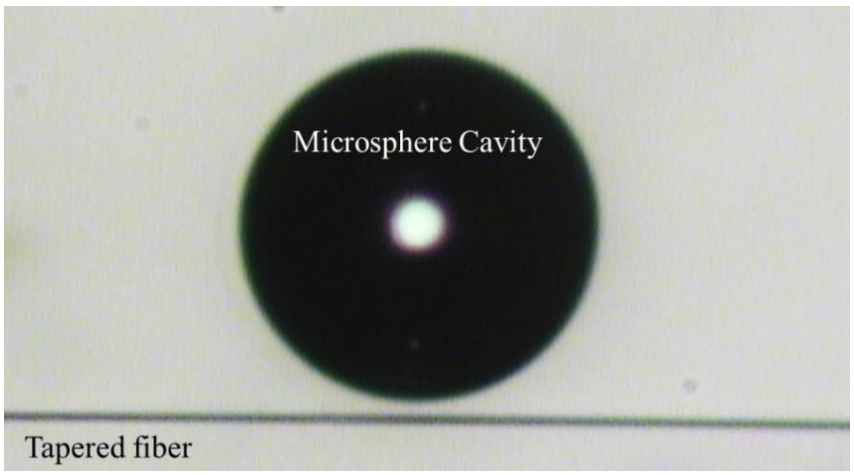

Figure 5.14: Tapered fiber coupling to a microsphere cavity resonator of 25 μm in radius.

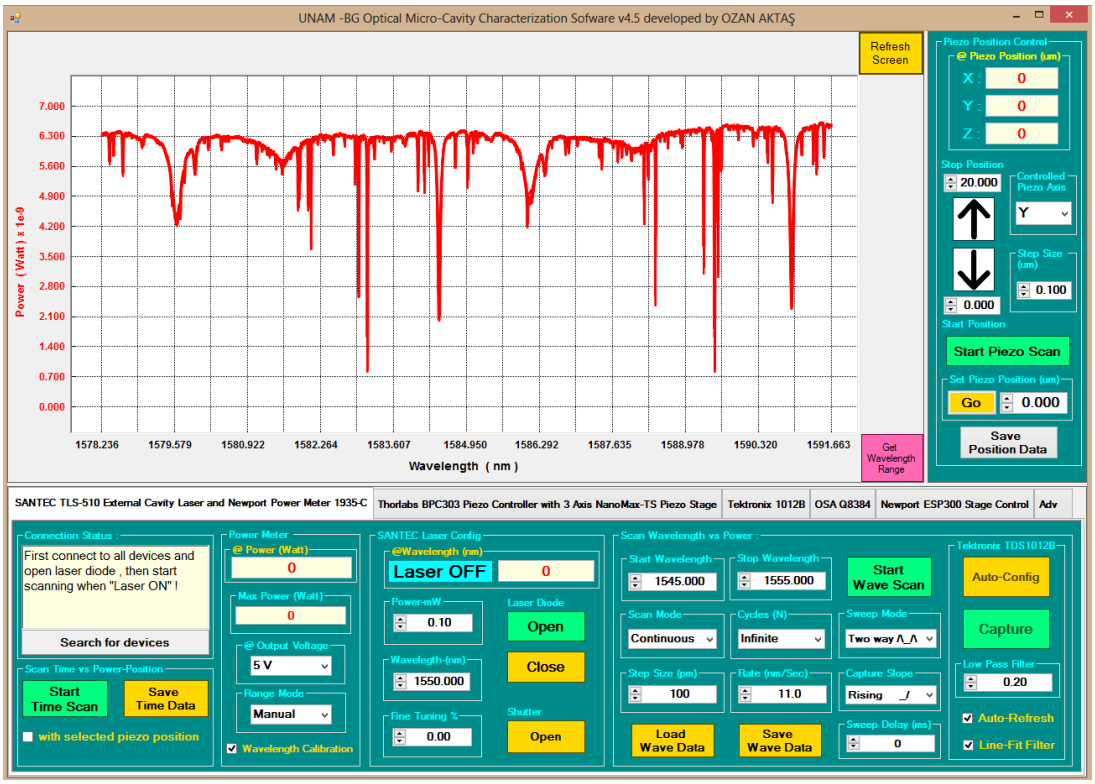

Figure 5.15: User interface of the developed software for optical characterization of microcavities.

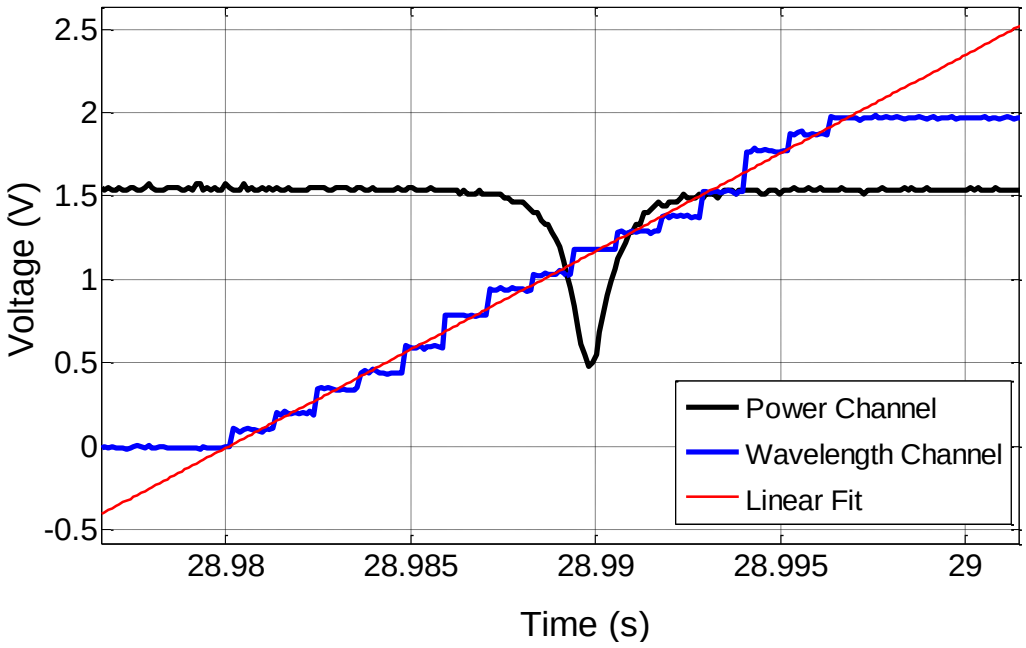

Figure 5.16: Two oscilloscope channels during a single wavelength scan. A linear fit to the wavelength channel is used to find start and stop wavelength points in the time axis. After calibration of both axis, data can be plotted in wavelength (nm) vs. power (W) format by the software during data acquisition.

Chapter 6

A New Route for Fabricating On-Chip Chalcogenide Microcavity Resonators

6.1. Introduction

The development of strategies for mass production and multiple integration of optical microresonators in photonic circuits has been a subject of intense research, aiming to reach the full potential of their technological exploitation. Among the different types of optical microresonators [36], especially surface-tension-induced whispering gallery mode (WGM) microresonators in the form of spheres [56] and toroids [57], are the focus of interest, regarding their compact shapes with atomically smooth surfaces which enable the highest temporal and spatial confinement of light in terms of quality factor ($Q \leq 10^9$) and mode volume, reducing the threshold for nonlinear optical interactions such as third harmonic generation,[49] four wave mixing [50], and Raman lasing [51]. Utilization of these appealing features has resulted in myriad applications including low threshold lasers [53], frequency comb generators [54], and extremely sensitive biological sensors [52]. However, spherical WGM resonators have limited functionality due to the restriction of their on-chip integration by shape and a priori unknown eccentricity. Resonators with a definite state of eccentricity can be obtained by deforming a sphere between two solid plates, compromising spherical symmetry [82]. A current state-of-the-art technology is the toroidal silica microresonator, produced by lithography and high power laser reflow techniques, which seem to have an advantage for mass production and on-chip integration. Unfortunately, the production demands individual surface reflow for each

and every resonator with high temperatures (above 1000 °C), hindering the integration of other optical components on the same substrate [83]. In addition, using silica as a resonator material makes optical coupling to an on-chip high refractive index waveguide highly inefficient. Alternatively, chalcogenides have recently been considered as a material for active and passive resonant media because of their high refractive index (n = 2.2–3.4), wide mid-IR transparency window, extraordinary high nonlinearity, photosensitivity, low two-photon absorption, low phonon energy, and ability to be doped by most of the rare earth elements [4, 7]. Even though their *Q*-factors ($<7 \times 10^7$) are not as high as that of silica WGM resonators, thresholds for some nonlinear optical interactions are on the same order of magnitude, due to their high nonlinearity [12]. Nevertheless, similar obstacles exist before the full utilization of the chalcogenide microresonators, emerging from the exclusive nature of their production and integration phases. Methods compatible to mass production can produce hundreds of polydisperse spheres [84, 85]. However, spheres with a desired shape and optical quality need to be separated from the debris by very elaborate and laborious techniques, and manipulated by their attachment on a fiber tip [10] or using optical tweezers [58]. Other methods, similar to production of silica spheres, rely on melting the tip of a chalcogenide fiber by laser heating [86]. Although these spheres are attached to a fiber stem, allowing them to be easily manipulated, high yield production is not possible due to the very nature of the process and the eccentricity caused by the stem [87]. Besides spheres on a fiber tip, an additional example for the *in-situ* formation of WGM resonators is photoinduced microcavity resonators in chalcogenide microfibers [88, 89]. The integration of a single chalcogenide sphere coupled to a tapered fiber has been demonstrated by packaging the system using a UV-curable polymer [90]. Another route towards the production of chalcogenide microspheres is to induce the Plateau-Rayleigh (PR) capillary instability[91, 92] in a chalcogenide fiber, which was first shown by optical fusing the bare core in the midair [85] and recently in a polymer cladding for small fiber lengths (<1 mm) by using a tapering process [93] and a local heat treatment [94].

In this chapter, we report a novel versatile method for the high yield production and on-chip integration of self-assembled globally oriented high-*Q* WGM chalcogenide microresonators with surface-tension-induced spherical, spheroidal, and ellipsoidal boundaries with sub-nanometer roughness [26]. The production involves the formation of chalcogenide microspheres within a polymer fiber of extensive length (≥5 cm),

which was accomplished by preserving the integrity of the polymer cladding during thermal treatment. The transformation of these spherically symmetric resonators en masse into axisymmetric or asymmetric resonators was conducted by controlled plastic deformation. By using a special polymer as an adhesive layer in the integration phase, we demonstrate the near-perfect transfer and attachment of the microresonators embedded in the polymer fiber on any substrate, preserving their initial symmetries. As a result, novel on-chip chalcogenide WGM resonators are introduced to the WGM microresonator family. By optical characterization of the spherical and spheroidal microresonators, we routinely obtain very high *Q*-factors: up to $Q_L = 3.1 \times 10^5$ which is, to our knowledge, the highest loaded *Q*-factor ever measured in As_2Se_3 WGM microresonators evanescently coupled to a silica tapered fiber.

6.2. Fabrication of Chalcogenide Microcavities

For the production of chalcogenide WGM microresonators, multimaterial fibers, which consist of a chalcogenide glass (As_2Se_3) core and a thermoplastic polymer polyethersulfone (PES) cladding, were used in this study. Fibers were obtained as a result of the size reduction of a preform (see Figure 2.3(a)) by thermal drawing in a fiber tower (see Figure 2.3(b)). The amorphous As_2Se_3 rod used in the production of the preform was prepared from high purity As and Se elements using a sealed ampule melt-quenching technique [24] (see Chapter 2.2). As a result of fiber drawing, we obtained fibers (see Figure 2.3(c)) with different diameters *d*, ranging from 1 mm to 30 μm, corresponding to As_2Se_3 core diameters ranging from 200 μm to 6 μm. In order to produce a long chain of uniform As_2Se_3 microspheres embedded in a PES fiber, we developed a novel thermal treatment technique, which is based on extensive convective radial heating of the fiber with a conformal polymer cover preserving the integrity and straightness of the cladding at elevated temperatures (see Figure 6.1). A long uncovered fiber with free ends on a hot plate was observed to be bent or even twisted while releasing the built-in tension originating from the thermal drawing process.

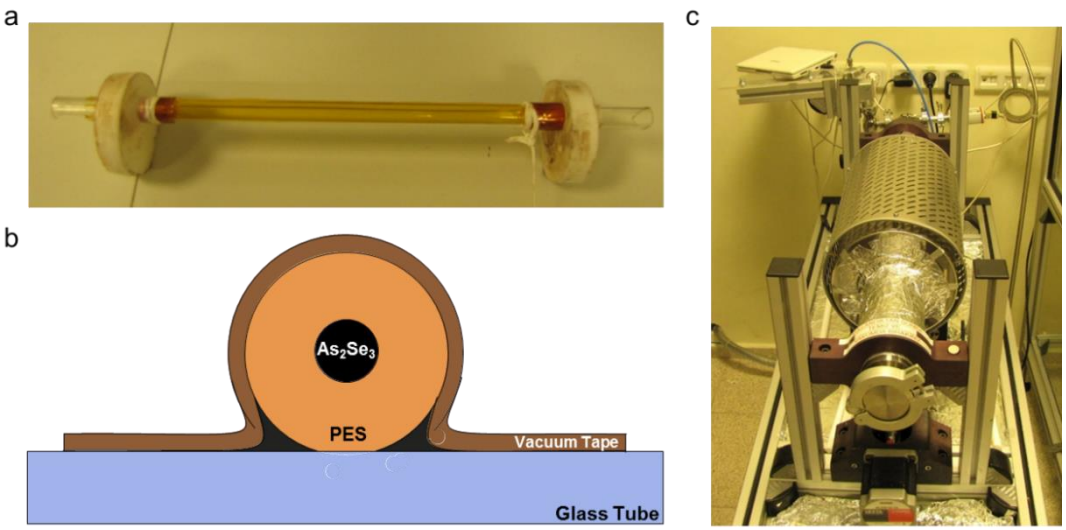

Figure 6.1: Formation of spherical microresonators in centimeter long polymer fibers. In order to produce a long chain of uniform As_2Se_3 microspheres embedded in a PES fiber, a novel method was developed, which takes the advantage of convective (non-contact) heating of fiber under a conformal cover assisting integrity and straightness of the fiber during the process. (a) A 12 centimeter long fiber was accommodated on a 10 mm diameter glass tube and (b) covered by a supporting vacuum tape (Kapton tape) which can stand high temperatures (over 320 ºC). In order to eliminate contact heating of fiber, the glass tube was isolated by two circular Teflon spacers from the walls of a custom-made tubular oven. (c) The tubular oven supplies necessary uniform heating with circular temperature distribution inducing PR instability in the fiber core. Releasing built-in stress, length of the fiber finally was reduced approximately to the half of initial length. After 15 minutes at 300 ºC, chalcogenide core polymer cladding fiber turned into a long self-assembled chain of microspheres held immobile in the cladding. After removing the cover tape and cutting uneven ends of the fiber, 5 centimeters long product, which is the longest fiber with embedded microspheres reported, was obtained at the end.

On the contrary to the processing conditions to which a fiber is exposed during fiber drawing, such as sudden cooling under tension, thermal treatment of As_2Se_3 core PES cladding fiber at elevated temperatures (260–310 °C) for substantial times leads ultimately to break-up of the continuous core into a chain of self-assembled spheres and inter-sphere satellites, due to overwhelming of surface tension against viscous forces. In order to understand the dynamics of PR instability and the evolution of the fiber core, using temperature dependent viscosities for both materials (see Figure 6.2) a two dimensional axisymmetric numerical finite element method simulation was performed by using the Fluid Dynamics Module in COMSOL for the modeling of heat-mediated microstructure formation.

Simulation and experimental snapshots of in-fiber microsphere formation (see Figure 6.3(a, b)) reveal that amplitude of the dominant sinusoidal modulation on the core surface grows over time until pinch-off, at which point detachment occurs, leaving a smaller structure in the middle exposed to the same instability over and over again, resulting in a fractal pattern of main spheres with satellite spheres on their sides. Satellite and sub-satellite sphere formations can be observed down to the 5^{th} generation, where the fractal process eventually stops reaching submicrometer scales (see Figure 6.4). Instability wavelengths, which are spatial periods of the structural perturbations on the fiber surface, determining the separation between the largest spheres at fiber core break-up, are given as a function of temperature along with the experimental and theoretical comparisons, and characteristic times for core break-up are given in Figure 6.5 and Figure 6.6, respectively. Pre-compensating the fiber diameter or adjusting the ratio of core diameter to outer diameter, a wide range of sphere sizes (1 mm – 1 μm) can be obtained. Fibers enclosing spherical microresonators were produced as long as 5 cm in length, as shown in Figure 6.3(c), limited only by the length of the tubular oven. However, uneven distribution of temperature or of stress caused by the conformal cover can result in unequal separations between main spheres.

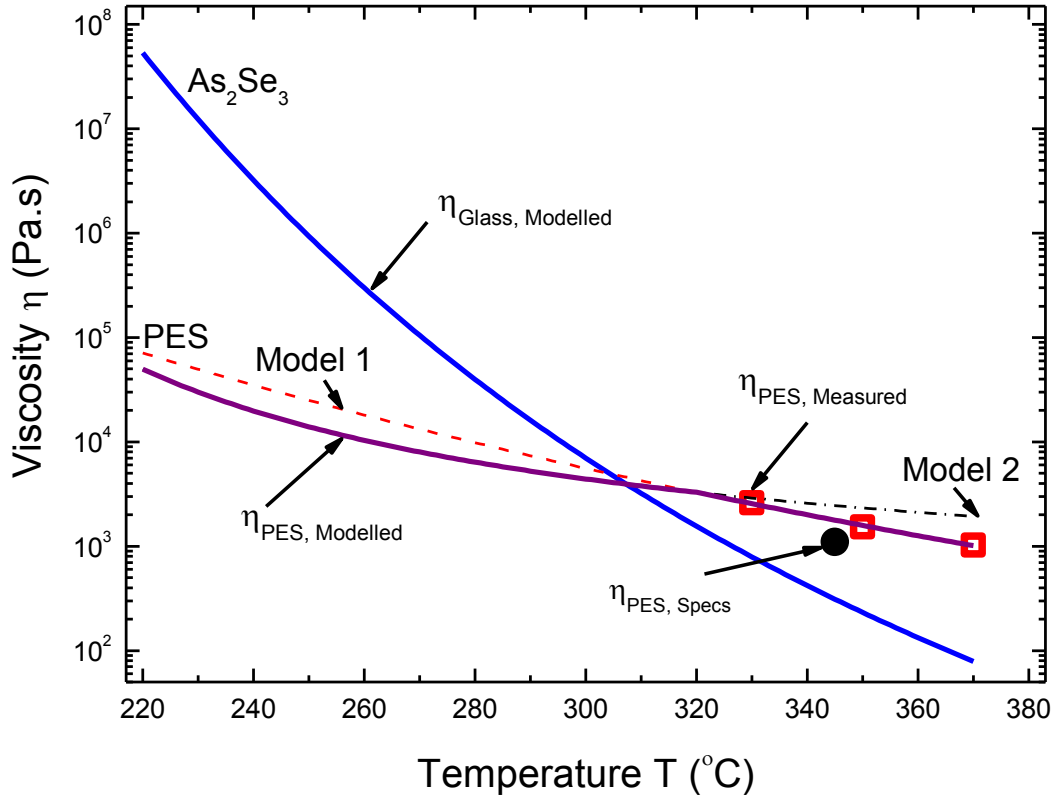

Figure 6.2: In our simulation, we used temperature dependent viscosities for both of the polymer cladding and the glass core. The As_2Se_3 and PES viscosities were determined by the universal logarithmic models.[95, 96] For the PES, we performed rheometry measurements to make sure that the viscosity used in the model was realistic and also consistent with the viscosity specified by the polymer manufacturer ($\eta_{PES, Specs}$). The PES model consists of two parts which are Model 1 (Arrhenius) for high temperatures and Model 2 with slightly varying activation energy for low temperatures.[96] Even the first order approximation of all Arrhenius relation gives more accurate modeling of PES viscosity than assuming a constant viscosity. This is because the viscosity contrast determines not only the instability wavelength, but also the characteristic time.

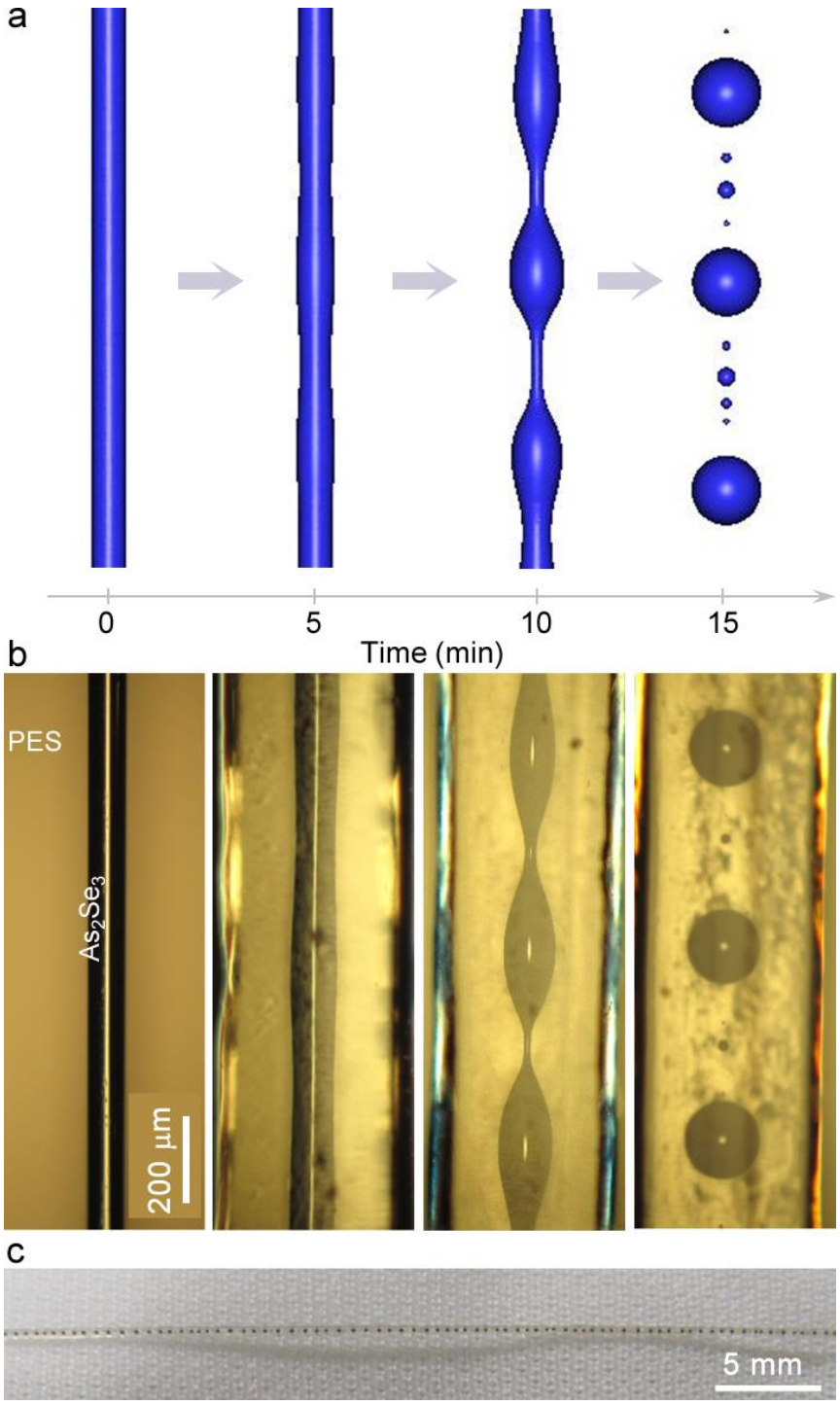

Figure 6.3: Simulation and experimental snapshots showing the evolution of microsphere formation in the As_2Se_3 core of a PES cladding fiber by Plateau-Rayleigh (PR) instability. (a) A finite element fluid dynamics simulation discloses clearly the dynamics of PR instability occurring in the fiber. (b) Initially intact 80 µm diameter chalcogenide core of the polymer cladding fiber turns into a self-assembled chain of 160 µm diameter spheres and smaller satellite spheres embedded inside the fiber, in 15 minutes at 300 °C. (c) A photograph of a 5 cm long PES cladding fiber with embedded As_2Se_3 microspheres.

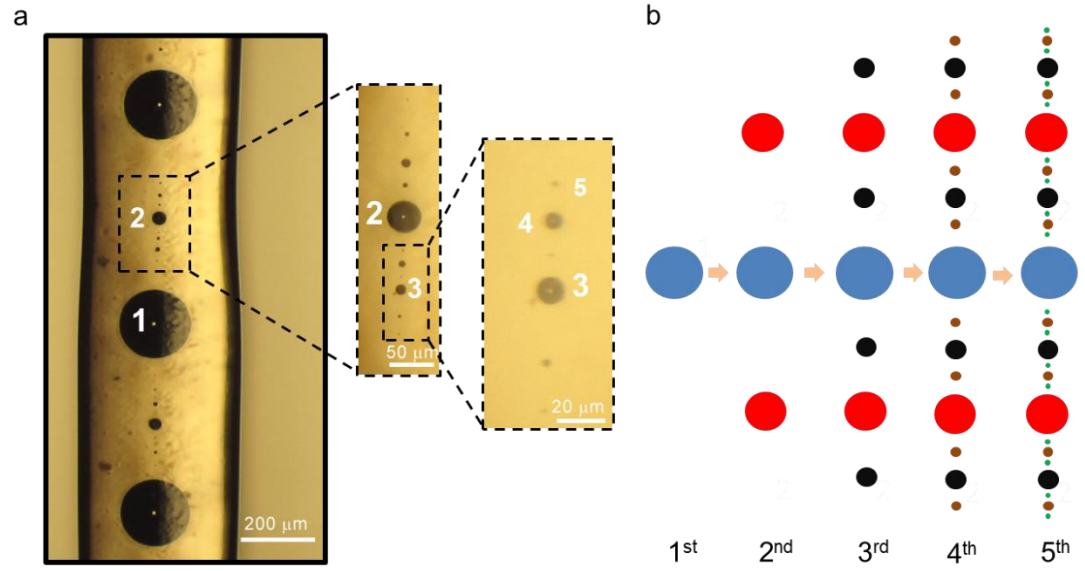

Figure 6.4: Fractal process of microsphere formation by Plateau-Rayleigh instability. (a) Optical microscope pictures show fractal nature of PR instability occurring in a fiber core. Successive optical micrographs of the fiber, showing inner structure with increasing detail are taken by using 5X, 10X and 20X objectives, respectively. Although the process is self-quenching after a number of generations finally reaching submicron scales, satellite and sub-satellite sphere formation between main spheres (the first generation) can be seen down to 5th generation. Numerical simulations also reveal same fractal pattern of in-fiber sphere formation. Numbers 1-5 in the figures indicate number of sphere generations. (b) Rule of thumb is as simple as graphically represented by the figure; i.e., for every next generation, two smaller satellite spheres are supposed to reside at the sides of larger spheres of previous generation.

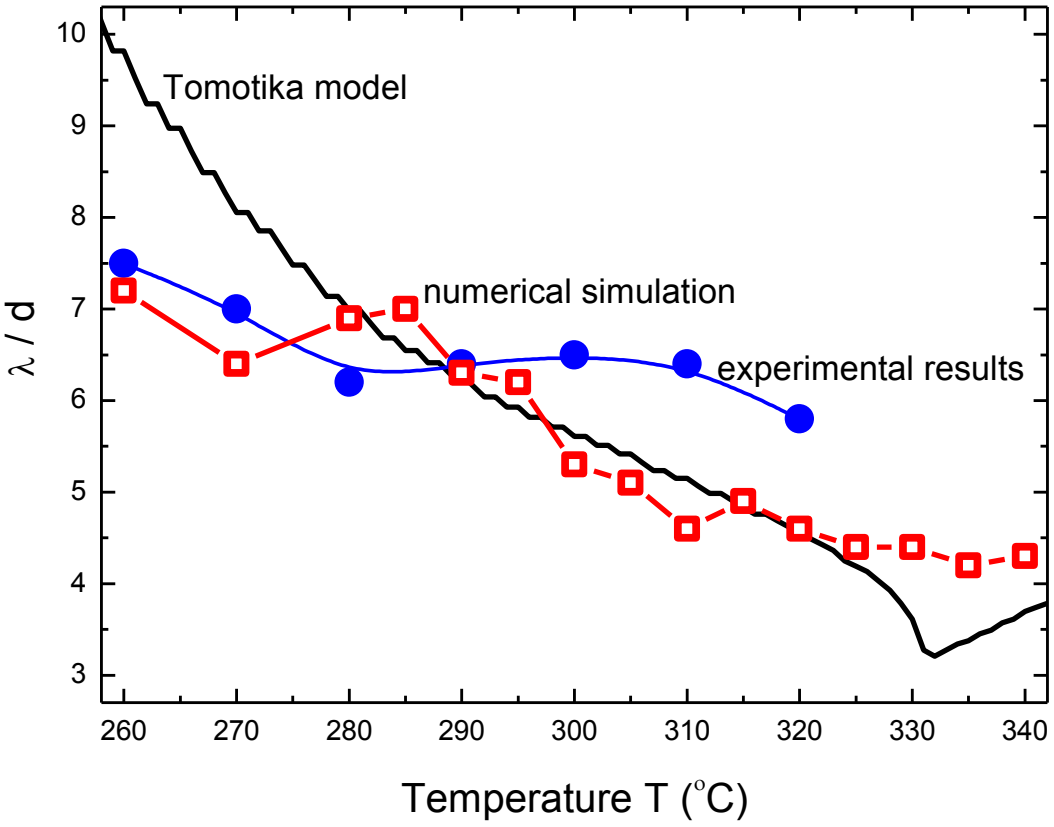

Figure 6.5: Theoretical comparisons of instability wavelength with experimental data. Comparison of the temperature dependent normalized (with respect to the initial core diameter *d*) average instability wavelength λ of experimentally produced micro-spheres and theoretically calculated data based on Tomotika model [91] and our 2D finite element numerical simulation. At low temperatures, the simulation coincides very well with the experiment, while Tomotika model over-estimate the instability wavelength. When the temperature is increased, both the simulation and the analytical models under-estimate the experimentally measured instability wavelengths. The best agreement between the three data sets is at moderate temperatures (T = 280-300 °C). Therefore, we chose this range for comparing the results of experiments and simulation of sphere formation.

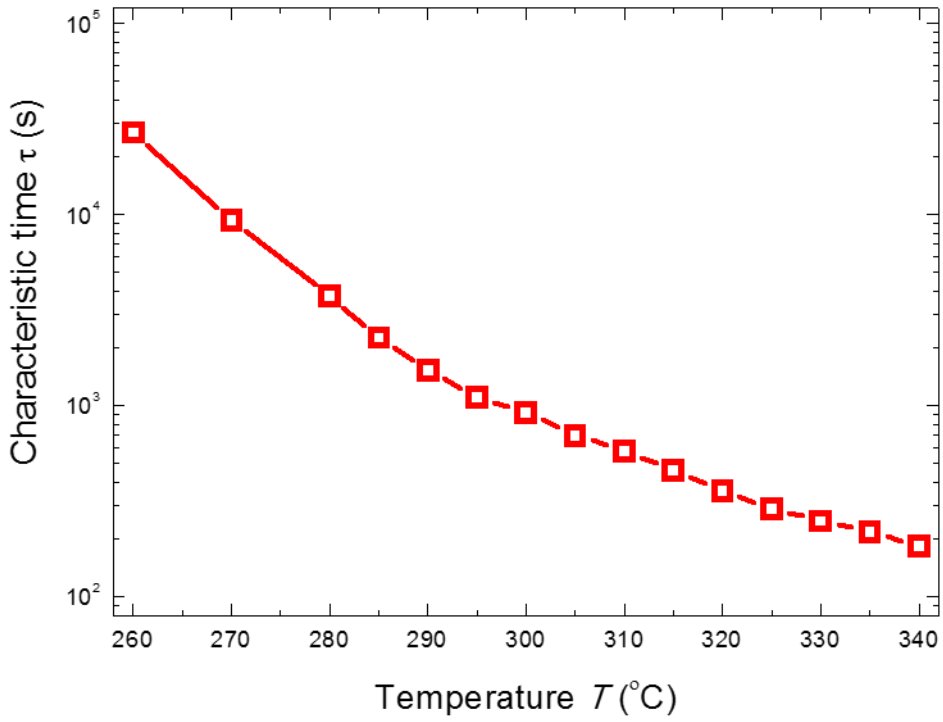

Figure 6.6: Characteristic time of fiber core break-up. The variation of the characteristic time (τ) as a function of temperature T. The characteristic time is defined as the time at which the break-up starts. The logarithmic decrease of τ with temperature follows two different activation regions intersecting at a point, which coincides with the viscosity contrast turning point (around 310 ^{o}C as in Figure 6.2).

Using continuous volume preserving transformations of the spherical microresonators induced by controlled plastic deformations in a custom made setup, we produced 3D ellipsoidal asymmetric resonant cavities (ARCs) with arbitrary eccentricity. ARCs, intrinsically possessing emission directionality, are important for laser applications [97] as well as for fundamental studies of classical and quantum chaos, due to the resemblance between the Hamiltonian dynamics of a point mass moving in a 3D space constrained by hard walls, and the ray dynamics of the light in a uniform dielectric cavity [59] Also, recently, enhanced energy storage in deformed optical resonators was reported [98].

Mechanical deformation of a PES polymer fiber enclosing an As_2Se_3 microsphere array between two parallel glass plates at a temperature of 280 °C, which is above the glass transitions of the As_2Se_3 (T_g = 170 °C) and PES (T_g = 220 °C), transforms the array of spheres into an array of triaxial ellipsoids, and finally into an array of "cigar-shaped" bodies globally oriented in a perpendicular direction to the fiber axis, because the fiber yields readily in this direction. Schematics of the fiber deformation process between two parallel glass plates in a high temperature furnace and deformation setup can be seen in Figure 6.7(a) and Figure 6.8, respectively. Optical reflection micrographs of deformed fibers can be seen in Figure 6.7(b–d). The specular Fresnel reflection (R = 22%) from the surface of resonators can be used to easily discriminate spherical and ellipsoidal cavities. We used dichloromethane (DCM) to dissolve PES cladding and to reveal spherical, ellipsoidal and "cigar-shape" cavities. Scanning electron microscopy (SEM) micrographs of the resonators given in Figure 6.7(e–g) show that it is possible to obtain smooth surfaces after deformations in a polymer encapsulation. SEM micrographs in Figure 6.7(h, i) show profile views of ellipsoidal and "cigar shape" cavities.

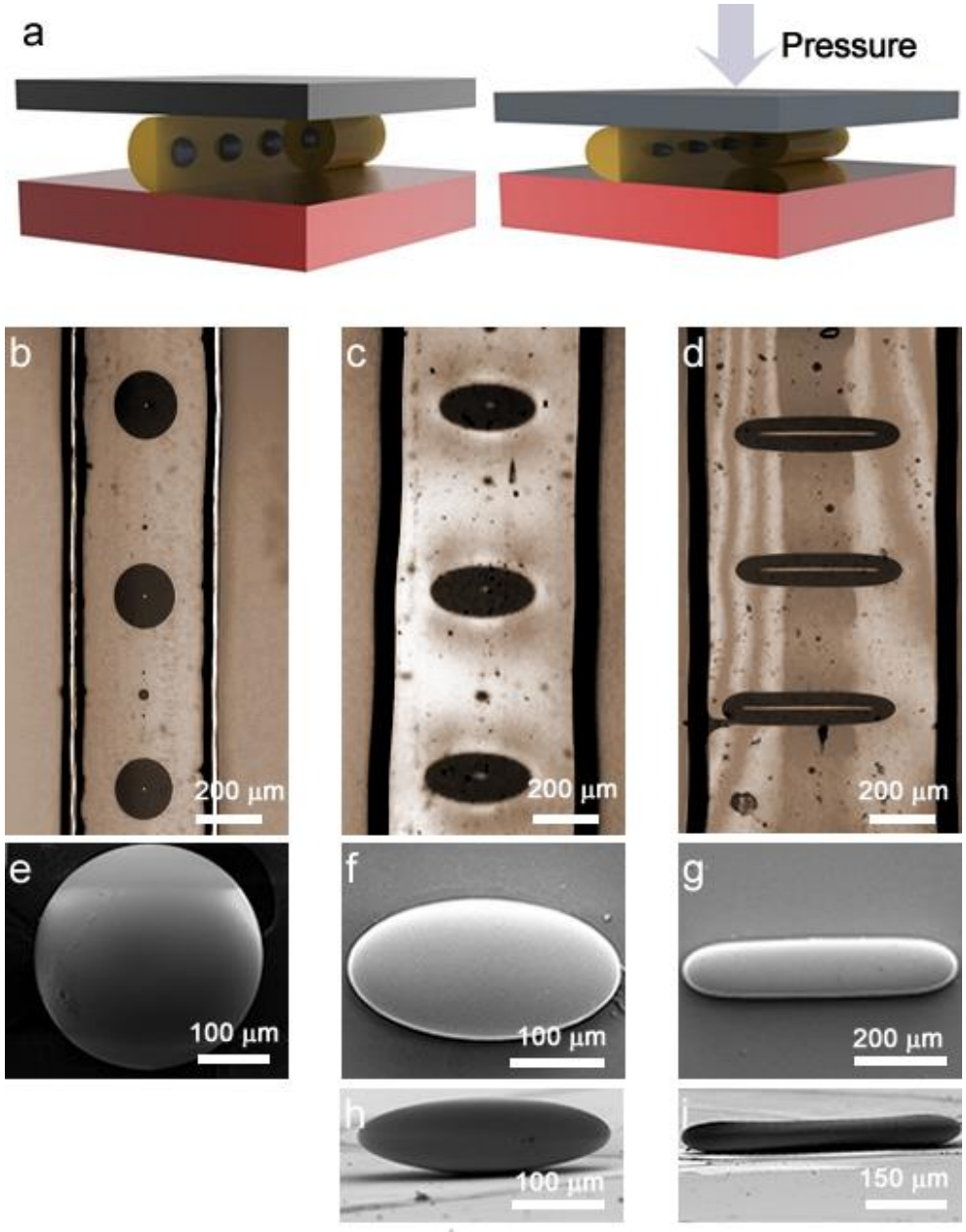

Figure 6.7: High yield production of 3D asymmetric microresonators via continuous volume preserving transformations induced by controlled plastic deformations. (a) Schematics of fiber deformation between two parallel glass plates in a high temperature furnace. Mechanical deformation of a PES polymer fiber enclosing an As_2Se_3 microsphere array at a temperature above the T_g of the both materials, transforms (b) the array of spheres into (c) an array of triaxial ellipsoids, then into (d) an array of "cigar-shaped" bodies globally oriented in perpendicular direction to the fiber axis. SEM micrographs show (e) spherical, (f) ellipsoidal and (g) "cigar-shape" cavities extracted out by dissolving the PES polymer cladding in DCM. SEM micrographs show (h) ellipsoidal and (i) "cigar-shape" resonators in profile view.

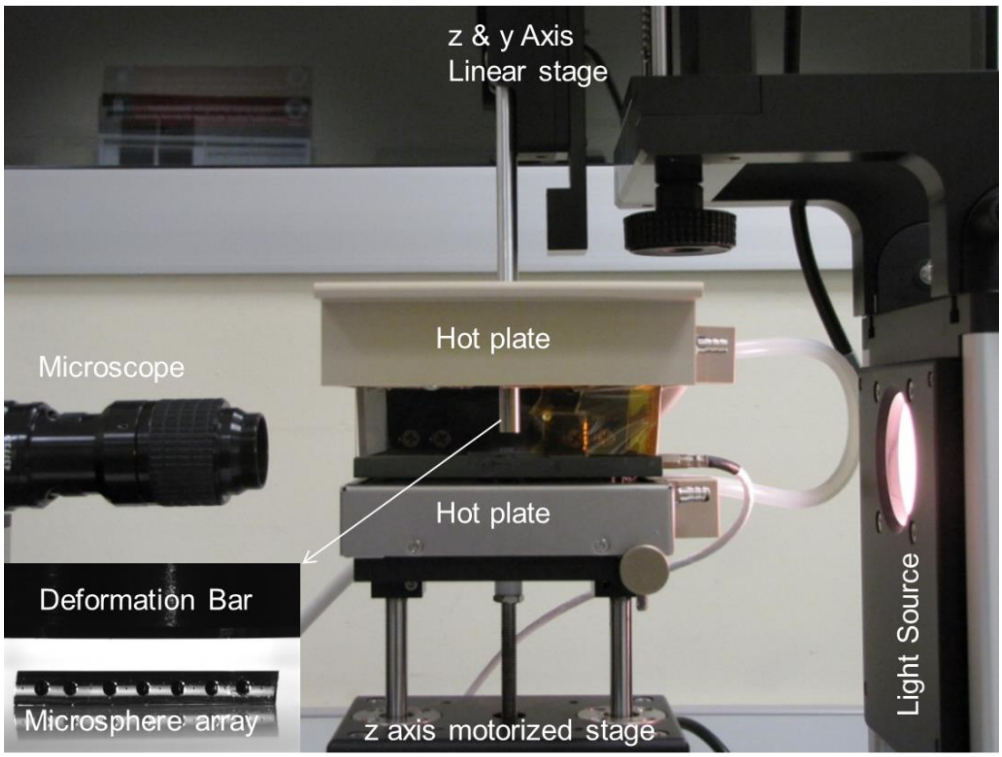

Figure 6.8: Microresonator array deformation setup. Experimental setup used for deformation and integration of microresonator arrays is actually a contact angle measuring system (DataPhysics OCA30) possessing a high temperature furnace (up to 400ºC) with temperature control. The system consists of a CCD camera, a long working distance microscope and a light source for process monitoring, an electrical furnace with two hotplates on top and bottom sides, and a z axis motorized stage under the furnace and a cylindrical bar attached to a z & y axis linear stage for alignment and deformation operations. Inset shows a fiber with embedded microspheres ready to be compressed.

6.3. On-chip Integration of Chalcogenide Microcavities

High yield production of spherical and ellipsoidal resonators inherently ordered in a polymer encapsulation can provide a unique advantage for multiple uses of these microresonators in photonics circuits, which is a critical barrier impeding their further development for relevant applications. Exploiting this advantage, we developed a method enabling on-chip integration of the chalcogenide microresonators with various shapes and sizes. Arrangements of cavities using conventional approaches for the integration are shown in Figure 6.9. In this new method (see Figure 6.10(a)), the integration process involves two steps, which are the preparation of the substrate and the fiber encapsulation of an array of microresonators. We used 100 μm thick glass coverslips as substrates, though there is no restriction for the substrate material. The substrates were spin coated with poly(vinylidenefluoride-co-trifluoroethylene) P(VDF- co -TrFE) solution for 45 s at 6500 rpm. The solution was prepared by sonification of P(VDF- co -TrFE) (30 g) in dimethylformamide (50 mL). Substrates were then placed on a hotplate at 100 °C for 1 h to accelerate solvent evaporation. After numerous trials with different polymers, P(VDF- co -TrFE) was found to be the most convenient as an adhesion layer regarding its low glass transition temperature (T_g = 80 °C), high adhesive forces towards chalcogenides, and chemical resistance against DCM. As for the preparation of the fiber, partial abrasion of the cladding was achieved by a simple sandpapering process, exposing the bottoms of the embedded microspheres as contact surfaces for adhesion. To facilitate sandpapering process, fibers were attached to glass plate with double sided bands, then exposed parts of the fibers were rubbed against sheets of SiC sandpapers with size of abrasive particles decreasing from 5 μm to 1 μm. After sandpapering process, fibers were released from the glass plate and cleaned by sonification in isopropyl alcohol for 10 min.

Optical micrographs of top, side, and bottom views of the fiber after sandpapering operation can be seen in Figure 6.10(b). The resulting fiber was transferred manually onto the substrate spin coated with a P(VDF-co-TrFE) polymer and then heated to promote adhesion up to a temperature of 210 °C, which is below the Tg of the PES cladding, but above the Tg of the As_2Se_3 core and the P(VDF-*co*-TrFE) coating. Finally, microresonators with their bottoms attached to the substrate surface were revealed by selective dissolution of the encapsulating PES polymer in DCM. In order to remove the PES encapsulation of the microresonators integrated onto a substrate,

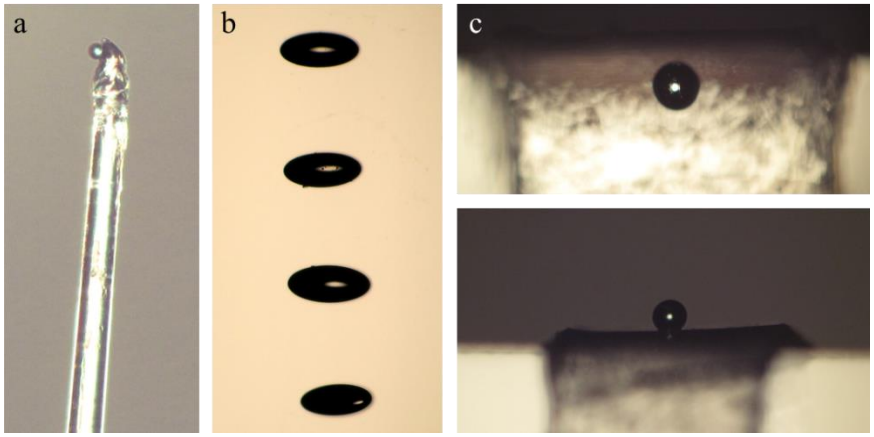

Figure 6.9: Conventional integration approaches: a) Microcavities attached to fibers. b) Manually arranged ellipsoidal cavities. c) Spherical cavity on a sticky tape.

we flushed the substrate with fresh DCM until most of the PES cladding dissolved away, then the substrate was placed in a fresh DCM solution for 1 h, and finally flushed over with fresh DCM again to remove dissolved polymer residues. As a final treatment, substrate with integrated microresonators was placed in a vacuum oven at 50 °C for 2 h to evaporate residual DCM. During the dissolution process all satellite cavities, which are smaller than the main cavities, are also flushed away spontaneously. This integration method enables the transfer of cavities on any substrate without any shape distortion, preserving the initial symmetry, due to protection by rigid PES encapsulation. An optical micrograph of on-chip well-ordered spherical chalcogenide WGM microresonator can be seen in Figure 6.10(c). Integration of spherical microresonators directly onto the metal surfaces is also possible (see Figure 6.10(d)); however, it requires temperatures higher than the Tg of PES, which is not suitable for non-spherical cavities due to the softening of PES encapsulation, and surface tension compromising the non-spherical symmetry at elevated temperatures. Ellipsoidal microresonators integrated on a P(VDF- co -TrFE) polymer coated surface can be also seen in Figure 6.10(e).

Another microcavity type with a different symmetry can be produced by compressing the on-chip microspheres upside down on a hot plate after their integration. Because of the different boundary conditions compared to those inside a polymer fiber, axisymmetric plastic deformation is favorable in this case and spheroidal microresonators with arbitrary elliptic cross sections can be easily produced. SEM micrographs of on-chip spherical/spheroidal/ellipsoidal chalcogenide WGM microresonator arrays are shown in Figure 6.11(a–c).

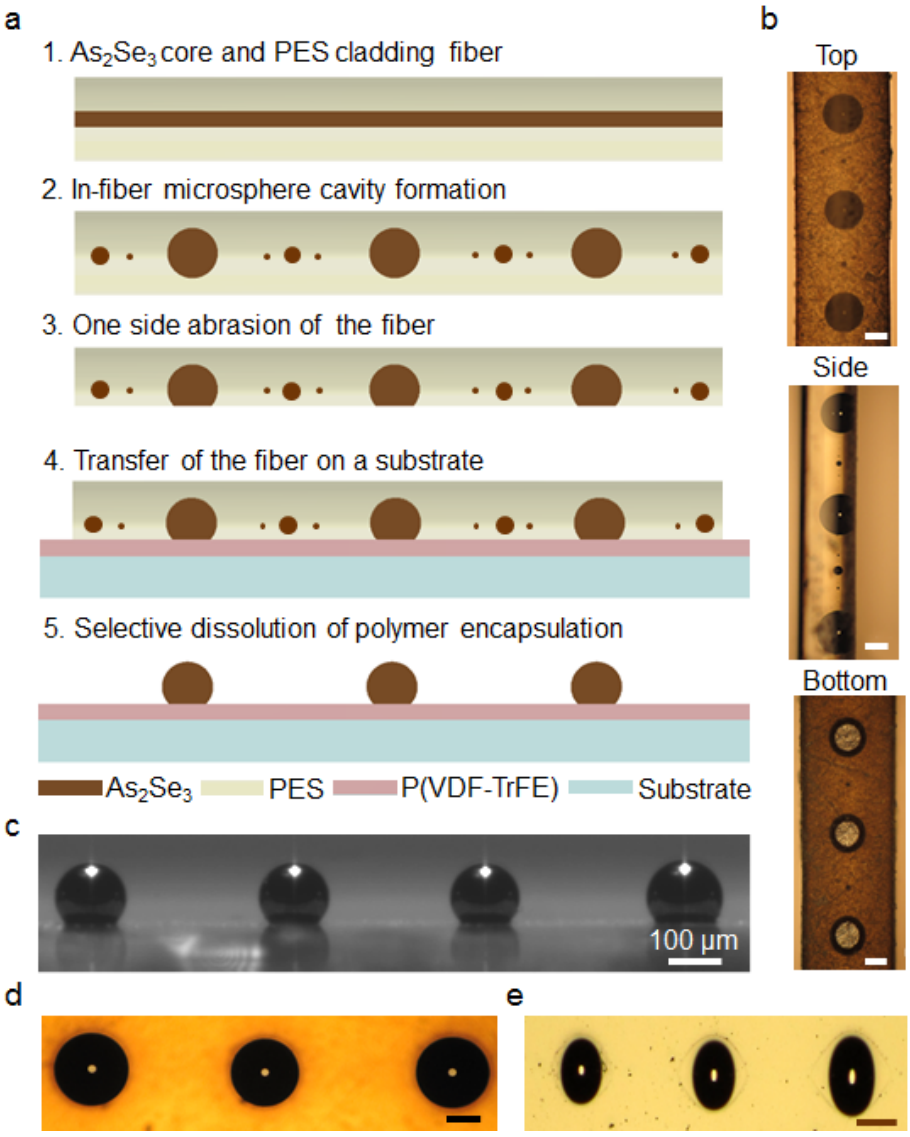

Figure 6.10: High yield production and on-chip integration of chalcogenide WGM microresonators on an arbitrary substrate. (a) The process starts with fabrication of As_2Se_3 core PES cladding fibers by thermal drawing. Then, in-fiber microsphere formation is induced by PR instability at elevated temperatures. As a third step, partial abrasion of the fiber cladding is achieved by a simple sandpapering process, exposing bottom sides of the spheres as contact surfaces for adhesion. In the fourth step, resulting fiber is transferred manually onto a substrate spin coated with P(VDF-TrFE) polymer and then heated to promote adhesion up to a temperature of 210 °C, which is below the T_g of PES cladding; however, above the T_g of both As_2Se_3 core and P(VDF-TrFE) coating. At the last step, the largest microcavities attached to the surface, can be released from the encapsulating PES polymer by selective dissolution in DCM, which has minimal effect on the substrate polymer coating. All satellite spheres are also flushed away spontaneously by the dissolution process. Optical micrographs show (b) top, side and bottom views of the fiber after sandpapering one of its sides, (c) on-chip spherical chalcogenide microresonator array, (d) spherical microresonators directly integrated on gold coated surface without any polymer coating, and (e) ellipsoidal microresonators integrated on P(VDF-TrFE) polymer coated surface. All scale bars are 100 µm.

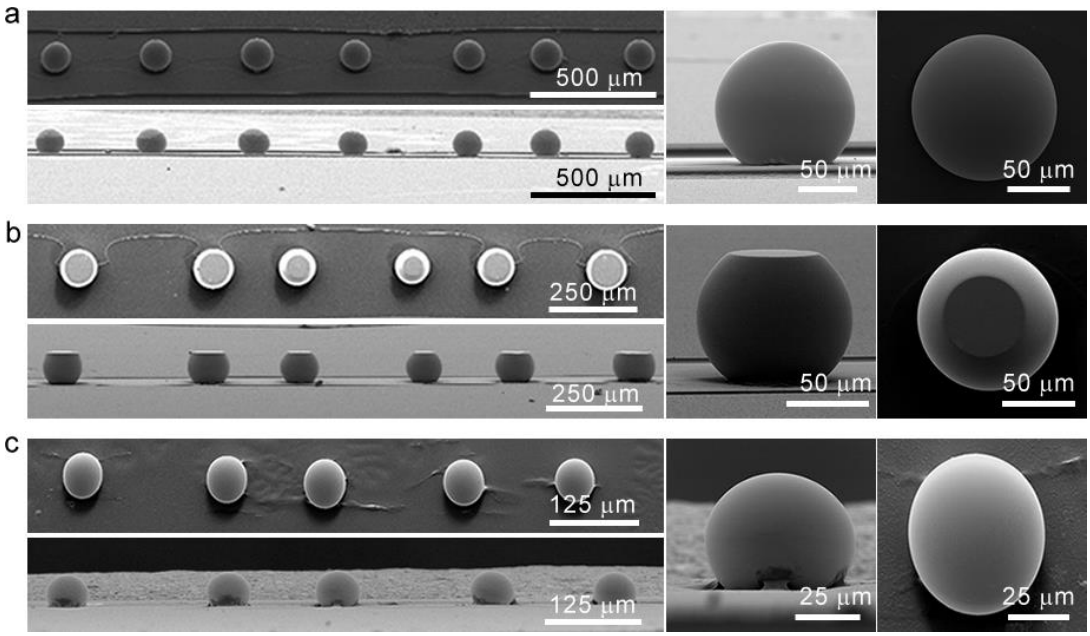

Figure 6.11: SEM micrographs of on-chip spherical/spheroidal/ellipsoidal chalcogenide microresonator arrays. Close-ups of some individual resonators in top and profile perspectives, show quality of production and on-chip integration such as the alignment of characteristic features (like equator plane), eccentricity, smoothness, and cleanliness of the resonator surfaces. (a) Top and profile SEM micrographs of spherical As_2Se_3 microresonator array and a single microsphere. Average diameter of spheres is d_{ave} = 124.4 μm with standard deviation σ = 3.4 μm (2.7%). As can be seen in the profile of the resonator, transfer and integration of the microsphere is accomplished with a very low aspherical deformation, and a good degree of parallel alignment of the equator plane with respect to the substrate surface. Top and profile SEM micrographs of (b) a spheroidal As_2Se_3 microresonator array and a single microspheroid, and (c) an ellipsoidal As_2Se_3 microresonator array and a single microellipsoid.

6.4. Optical, Material and Surface Characterizations

Energy dispersive X-ray spectroscopy (EDX) results obtained from the surfaces of on-chip microsphere resonators demonstrate the consistence of the atomic ratio of As_2Se_3 (see Figure 6.12), besides showing that no impurity or residual polymer exists on the surfaces of microspheres after the dissolution process. Furthermore, we conducted atomic force microscopy measurements for the quantitative surface characterization of the microresonators. Sub-nanometer rms surface roughness (σ <0.6 nm) was found from a 500 nm × 500 nm surface scan on top polar region of an ellipsoid (see Figure 6.13).

We used tapered silica fibers with submicrometer waist diameters (~700 nm) to evanescently couple light into these resonators and to capture transmission mode spectra (Figure 6.14(a–d)). Schematics of the experimental setup used for optical characterizations of microresonators and of tapered fiber coupling to WGMs of on-chip spherical cavity resonators are given in Figure 5.13 and Figure 6.15, respectively. In order to eliminate thermo-optic effects (see Figure 6.16), we used very low optical input powers (~100 nW). Wavelength scanning ranges of the external cavity laser were set as 12 nm and 50 pm for the acquisition of two free spectral range (FSR) wide spectra and single mode wide spectra, respectively. An adjustable polarization controller was used to maximize optical coupling into TE modes.

Despite the refractive index mismatch between the silica tapered fiber (n = 1.44) and the chalcogenide microresonators (n = 2.83) in the wavelength range of interest, it was possible to observe optical couplings to spherical and spheroidal microresonators, facilitated by a tapered silica fiber with sub-micro meter waist diameter, and resonators with small radii (~25 μm). The strength of the optical coupling critically depends on two parameters: the amount of field overlap, and phase matching between the fiber modes and the WGMs [73]. Excitation of modes with high radial mode numbers are more favorable than low order modes in our case, because high order radial modes have low propagation constants, reducing phase mismatch, and higher evanescent field fraction outside the cavity, enhancing the field overlap. Reducing the size of the cavities also enhances optical coupling, which is in accordance with our experiments on microresonators under 60 μm in diameter.

We observed a series of resonance dips corresponding to WGMs of a microsphere

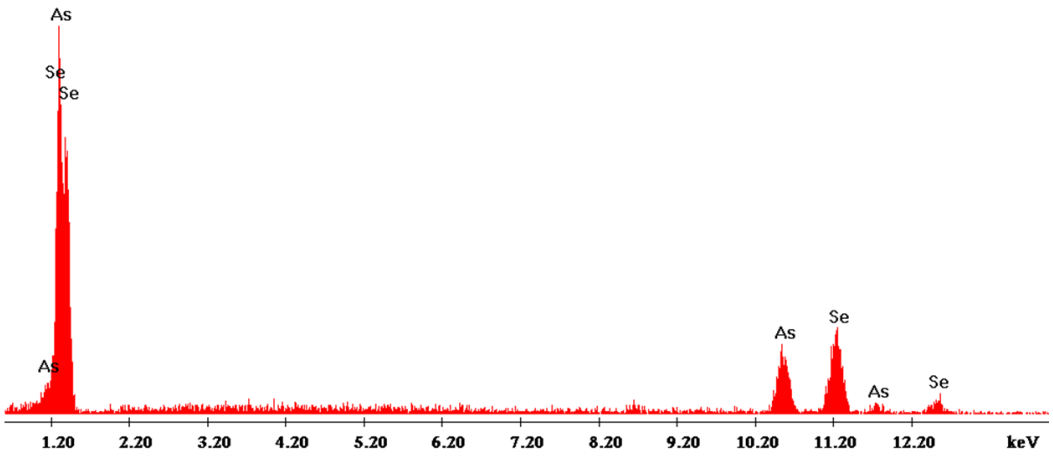

Material : As_2Se_3

Elem	Wt %	At %	K-Ratio	Z	A	F
AsK	38.24	39.49	0.3858	1.0152	0.9937	1.0000
SeK	61.76	60.51	0.6137	0.9905	1.0033	1.0000
Total	100.00	100.00				

Figure 6.12: Characterization of microresonator material composition. Energy dispersive X-ray spectroscopy (EDX) results obtained from on-chip microsphere resonators which were extracted out of their PES polymer encapsulation using DCM. EDX is attached to FEI Quanta 200 FEG SEM system. Peaks represent consistence of the atomic ratio of As_2Se_3. Besides, there was no impurity or residual polymer observed on the surface of microspheres after the dissolution process.

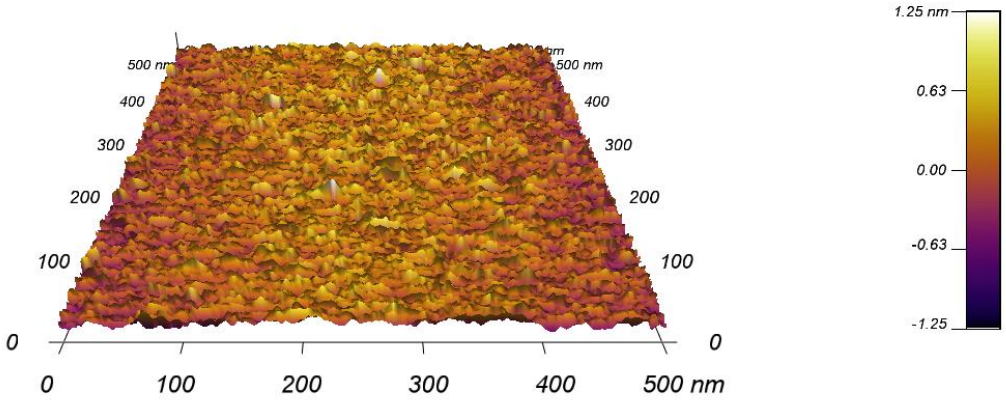

Figure 6.13: AFM surface characterization of an ellipsoidal microresonator on (500 nm×500 nm) top polar region shows sub-nanometer rms surface roughness ($\sigma < 0.6$ nm).

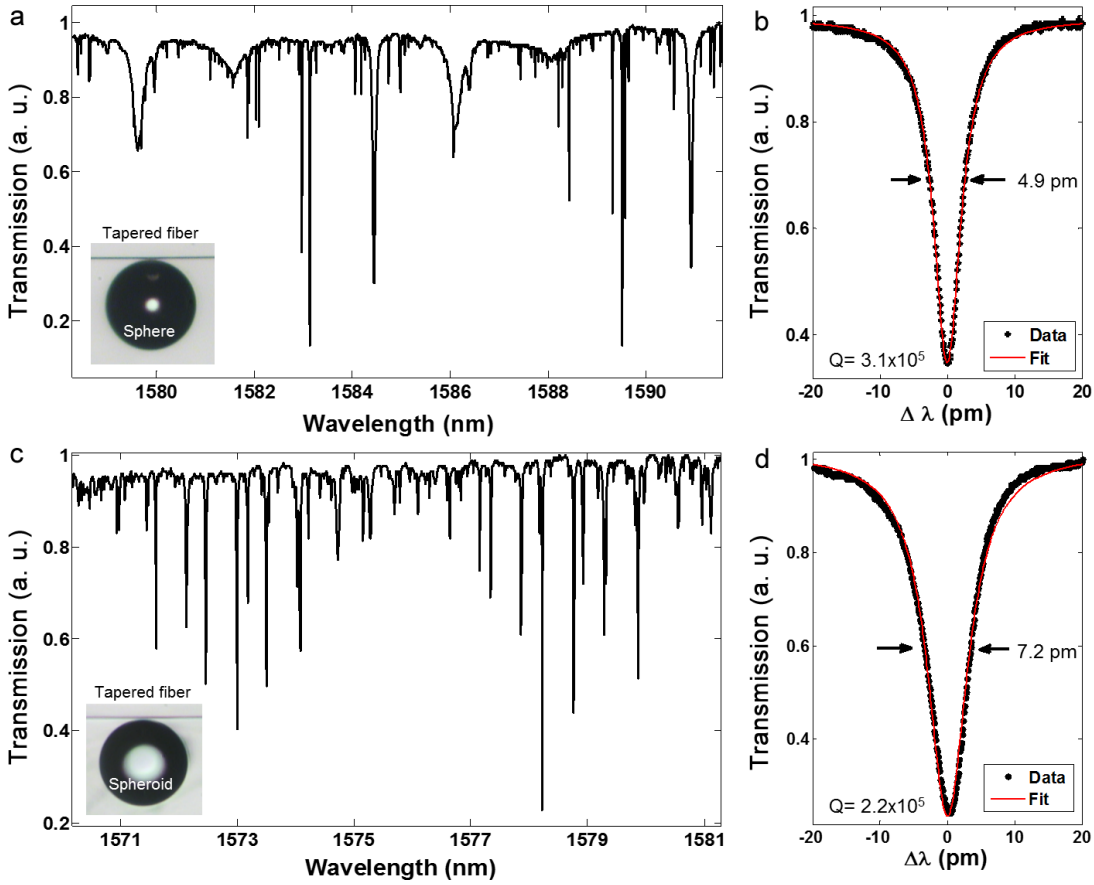

Figure 6.14: Optical characterizations of on-chip spherical and spheroidal chalcogenide microresonators. (a) Transmission spectra of an As_2Se_3 microsphere resonator of 50 μm in diameter. Coupling strength of resonance modes can be as high as 10 dB. FSR is 6.39 nm. (b) Lorentzian fit to a resonance dip at 1551.858 nm shows that the FWHM and loaded quality factor Q_L of the resonance mode are 4.9 pm and 3.1×10^5 , respectively. Inset shows evanescent coupling of light into the microsphere resonator using a tapered silica fiber with a sub-micrometer waist diameter. (c) Transmission spectra of an $AsSe_3$ microspheroid resonator of 57 μm in equator diameter. FSR is 5.22 nm. (d) Lorentzian fit to a resonance dip at 1571.589 nm shows that FWHM and loaded quality factor Q_L of resonance mode are 7.2 pm and 2.2×10^5, respectively. Inset shows evanescent coupling of light into the microspheroid resonator using a tapered silica fiber.

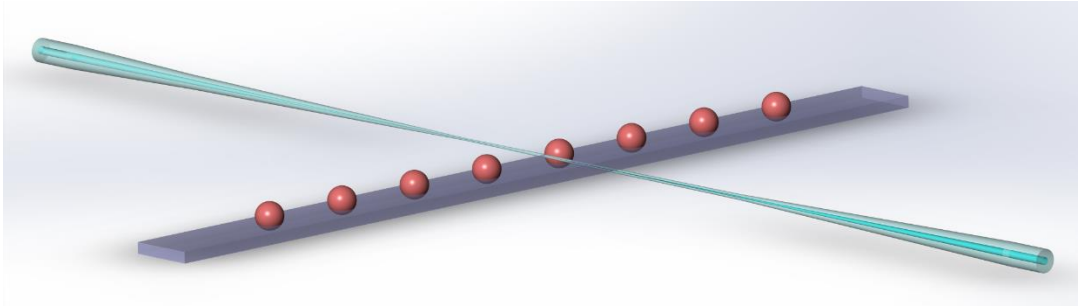

Figure 6.15: Schematic of the tapered fiber coupling to WGMs of on-chip spherical cavity resonators.

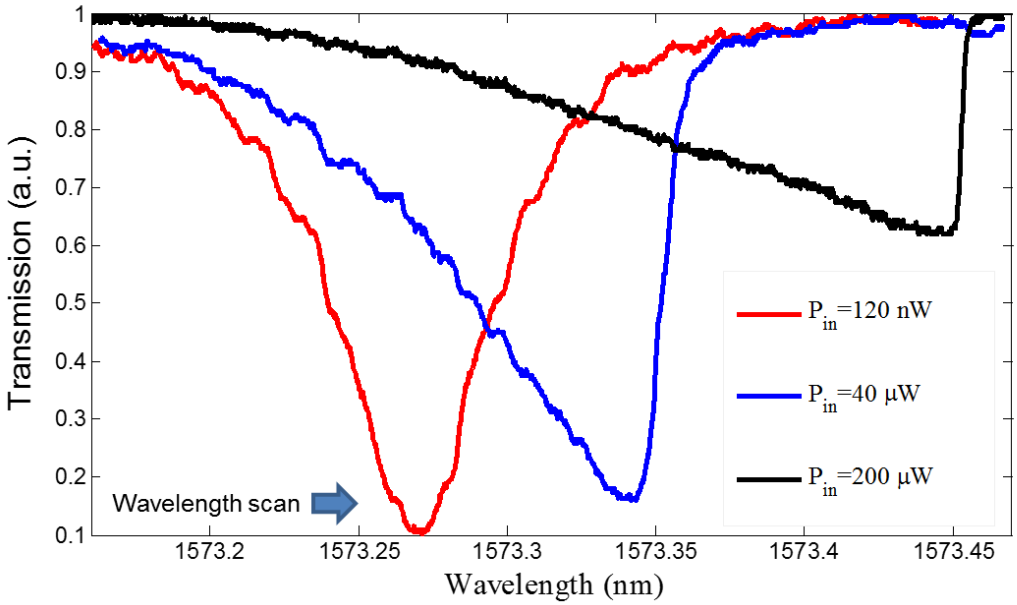

Figure 6.16: The resonance dips in the spectra of As_2Se_3 microresonators were observed to red-shift with increasing incident powers for both directions of wavelength scans. Although an un-shifted resonance dip (red), which was captured using very low optical powers with 300 pm scan range and 1 $nm.s^{-1}$ scan speed, has a regular Lorentzian shape, red-shifted versions of the resonance mode (blue, black) have characteristic "shark fin" shapes.[86] Since As_2Se_3 has relatively high absorption coefficients as compared to silica in this scan range, red-shifts of modes are expected, due to the heating of the resonator via absorption of the coupled light resulting in a thermal change of the refractive index and thermal expansion of resonator diameter. Reduction in the coupling strength is another manifestation of thermo-optic effect, caused by insufficient scan speed at some power levels for which wavelength shift can be more than line width of the resonance mode at some point during wavelength scanning [99].

(D = 50 μm) and an oblate microspheroid (D = 57 μm) with transmissions as low as 10 dB. Resonance mode splitting can also be seen in the spectra of a microspheroid (see Figure 6.14(c)), because of the broken degeneracy of azimuthal modes. In single mode spectra, a full width at half maximum value (FWHM) of 4.9 pm was obtained by a Lorentzian fit to the resonance mode of the microsphere at 1551.858 nm, corresponding to a loaded quality factor of $Q_L = 3.1 \times 10^5$ associated with a transmission depth of K = 4.6 dB (see Figure 6.14(b)). The average of the loaded quality factors we measured is $Q_{ave} = 2.9 \times 10^5$ with a standard deviation of $\sigma = 0.6 \times 10^5$. Similarly, a FWHM of 7.2 pm was obtained by a Lorentzian fit to the resonance mode of the microspheroid at 1571.589 nm, corresponding to a loaded quality factor of $Q_L = 2.2 \times 10^5$, associated with a transmission depth of K = 6.2 dB (see Figure 6.14(d)). The maximum Q-factor reported for As_2Se_3 WGM resonators is $Q_{max} = 2.3 \times 10^6$, which was measured using a phase matched silicon waveguide evanescently coupled to a microsphere produced on the tip of a fiber [99].

Experimentally measured quality factors Q_L are described by the expression

$$1/Q_L = 1/Q_{in} + 1/Q_{ext} \tag{6.1}$$

written in terms of intrinsic Q_{in} and extrinsic Q_{ext} quality factors, which are determined by resonator related losses and coupling losses, respectively. The intrinsic quality factor of WGM modes of microresonators are determined by several factors

$$1/Q_{in} = 1/Q_{rad} + 1/Q_{ss} + 1/Q_{mat} \tag{6.2}$$

such as radiative losses, scattering losses, due to surface roughness and contamination, and material absorption losses. For intermediate size resonators (D ~50 μm) with sub-nanometer surface roughness ($\sigma < 0.6$ nm) as in our case, and in the absence of surface contaminants, Q-factor is only limited by material losses and given as [61]

$$Q_{mat} = 2\pi n/\alpha\lambda \tag{6.3}$$

where α is absorption coefficient, n is refractive index and λ is wavelength. Using a material absorption coefficient $\alpha = 1.6\ m^{-1}$ of a commercially available As_2Se_3 glass at 1550 nm (see Figure 6.17(a)), the absorption limited intrinsic Q-factor was found to be $Q_{mat} = 7.2 \times 10^6$, which is the maximum limit for experimentally obtainable quality factors (see Figure 6.17(b)). In addition, all WGM modes of the cavity suffer from the optical coupling process as well. The amount of coupling loss depends on phase matching and the field overlap of modes determined by mode order, radius of the cavity, radius of the tapered fiber, and the air gap between them [76].

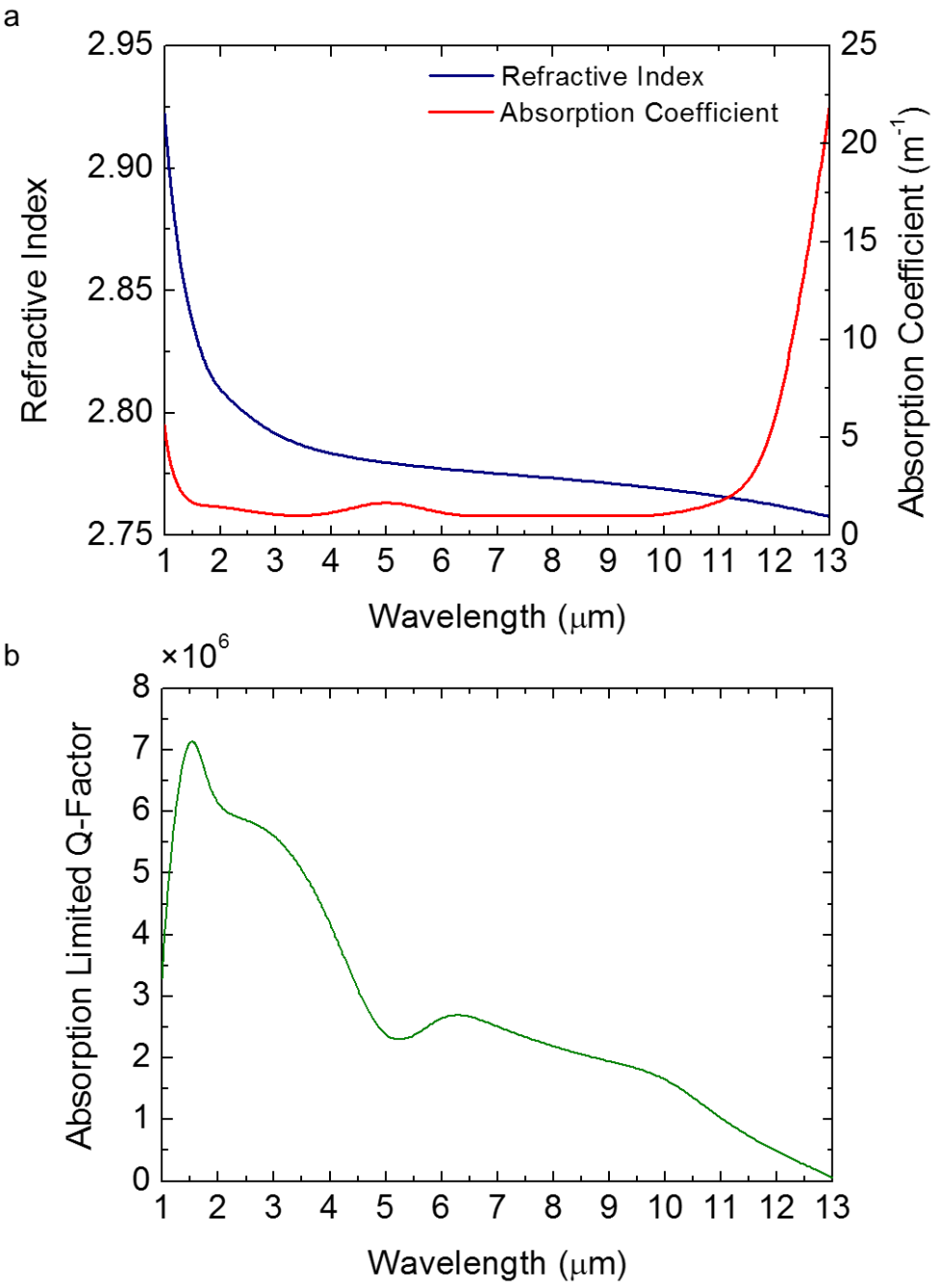

Figure 6.17: Optical properties of a commercial As_2Se_3 glass [100] are given in terms of (a) refractive index n and absorption α as function wavelength λ. Absorption is α = 1.6 m^{-1} at 1550 nm. (b) Absorption limited quality factor Q_{abs} can be calculated from (n, α) data, as $Q_{\mathrm{abs}} = 2\pi n/\lambda\alpha$. Q_{abs} for As_2Se_3 is found to be 7.2×10^6 for λ = 1550 nm and n = 2.83, which is an upper bound for intrinsic Q-factors in the case of ultra-smooth and clean resonator surface. Although As_2Se_3 has relatively high absorption compared to silica restricting its use as nonlinear optical material, it is a very promising material for microresonators in mid-IR applications, due to low absorption and high Kerr nonlinearity.

By adjusting the air gap, the quality factor Q_c set by coupling loss can be tuned to achieve different regimes of coupling, where transmission T drops to zero ($K = 1$) at critical coupling. Using the measured loaded quality factor $Q_L = 3.1 \times 10^5$ and the transmission depth $K = 0.65$ in the following derived expression [66],

$$Q_0 = 2Q_L\left[1 + \sqrt{1-K}\right]/K \tag{6.4}$$

we calculated the intrinsic quality factor as $Q_0 = 0.76 \times 10^6$, corresponding to an absorption coefficient $\alpha = 15\ m^{-1}$. It can be considered to be on the order of magnitude of absorption limited quality factor Q_{mat} of As_2Se_3. The discrepancy is assumed to be caused by a higher optical absorption in our synthesized chalcogenide glass or water condensing on cavity surfaces in lab conditions, at which we observed one order of magnitude degradation in the Q-factors of chalcogenide microresonators held three weeks in lab conditions. We could not detect any transmission dips in the mode spectrum of triaxial ellipsoids with tapered silica fibers favoring only coupling to high order modes; however, we can directly observe light coupling into the micro-ellipsoids by thermal imaging (see Figure 6.18). The reason for the absence of transmission dips in the spectrum of ellipsoids could be due to the expected complete suppression of high order modes in deformed resonators of high eccentricity [101] or some mechanisms similar to Arnold diffusion in the phase space of 3D ARCs, resulting in Q-spoiling with refractive escape of light [102], which require further theoretical studies of ARCs in 3D. Nevertheless, phase matched waveguides can be used to couple light evanescently into low order modes of ellipsoidal microresonators to observe transmission dips.

In summary, we have developed a simple, scalable, and lithography-free method for the production and on-chip integration of high-Q factor WGM chalcogenide microresonators with spherical, spheroidal, and ellipsoidal boundaries with subnanometer surface roughness. High yield, low cost production of hundreds of self-assembled chalcogenide microresonators was achieved inducing PR instability in extended lengths of a multimaterial fiber. Since PR instability is a well-established phenomenon, our production and on-chip integration scheme are not limited to As_2Se_3 and can be applied to other important optical materials including As_2S_3 , Si, Ge, and SiO_2 , which can be turned into microcavities inside suitable cladding materials [103-105].

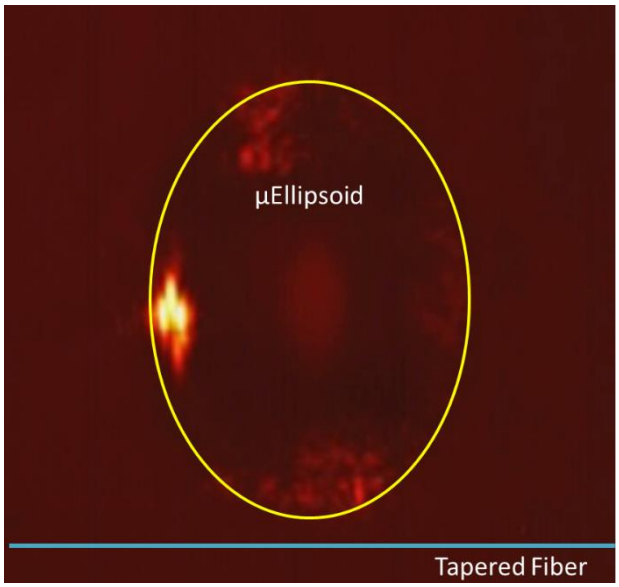

Figure 6.18: This snapshot of a movie recorded by a thermal camera, shows optical coupling to an ellipsoidal microcavity using a silica tapered fiber approaching from the bottom. Bright spot on the left in the middle is an ambient scattered light reflected from the surface, which is irrelevant to optical coupling with the tapered fiber.

Furthermore, active chalcogenide resonators can be made by doping with rare earth elements for on-chip laser applications. Utilizing the shape preserving protection of the polymer encapsulation, near-perfect transfer of the embedded microresonators onto any substrate in a globally oriented fashion is demonstrated. We observed loaded *Q*-factors as high as $Q_L = 3.1 \times 10^5$ in our on-chip microcavity resonators. To our knowledge, it is the highest *Q*-factor ever measured in As_2Se_3 microresonators with silica tapered fibers favoring optical coupling only to high order WGM modes. Easy on-chip integration of highly nonlinear high-*Q* microresonators can pave the way for new or extended exploitation of photonic devices in applications such as mid-IR sensors for the detection of molecular fingerprints, frequency comb generators for the generation of ultra-pure microwaves, ultra-low threshold microlasers with emission directionality, electro-optical tunable filters or modulators for optical communications, and optical logic gates for all-optical processors.

Chapter 7

Electro-Optic WGM Resonator Based Chalcogenide Photonic Devices

7.1. Introduction

Technological advances in recent years with ever increasing data requirements demands all optical circuits which can handle data communications well beyond the current capacity of electronics [106]. Such photonic solutions for data communication will be integrated on the top of electronic chips that can efficiently handle computation, therefore in addition to the all-optical capabilities, electro-optical materials are needed for a higher device functionality. Although linear electro-optic materials [107] such as $LiNbO_3$ are currently used in photonic circuits as modulators, they lack all-optical signal processing capability due to the second order nonlinear effect. On the other hand, the quadratic electro-optical effect is too weak to be useful or requires very high voltages to operate. One solution to this problem is to employ resonant cavities of highly nonlinear $\chi^{(3)}$ materials to enhance quadratic electro-optical Kerr effect .

Chalcogenides are already exploited for all-optical photonics applications [16], however, utilization of electro-optical Kerr effect in a chalcogenide cavity has not been shown before. Combining quadratic electro-optical capability with optical Kerr nonlinearity [108] in micron scale chalcogenide disk cavities is expected to pave the way for a myriad new applications such as tunable frequency comb generators [109], tunable sources of non-classical states of light for quantum optics [110], and cavity quantum electro optics [111] as well as tunable filters [112], ultra-fast modulators [113], microwave photonic receivers [114], optoelectronic oscillators [115].

7.2. Simulation of WGMs in an Electro-optic Cavity

We use COMSOL 4.4b Wave Optics Module (electromagnetic waves frequency domain and electrostatics stationary interface) to find WGMs in a microdisk cavity between two metal plates under an applied voltage *V*. Simulations are based on 2D axisymmetric finite element method (FEM). We use coupled physics property of COMSOL. Two simulations with different physics can be done concurrently or successively. In the electrostatics simulation, the electric potential *V* is first solved, electric vector field ***E*** is found by

$$\vec{E} = -\nabla V \tag{7.1}$$

Combining this equation with the constitutive relationship between dielectric displacement vector ***D*** and electric vector ***E***

$$\vec{D} = \varepsilon_0 \varepsilon_r \vec{E} \tag{7.2}$$

and using Gauss's Law, we obtain the following equation

$$-\nabla \cdot (\varepsilon_0 \varepsilon_r \nabla V) = \rho \tag{7.3}$$

where ε_0 is the permittivity of vacuum, ε_r is the relative permittivity of the medium, and ρ is space charge density. This equation, which describes the electrostatic problem in dielectric materials, is solved by COMSOL in axially symmetric geometry. In the electromagnetic wave simulation, ***E*** field is given by Equation 4.35 and the Equation 4.36 is solved for the axially symmetric geometry.

Simulation domain is a half circular area of 60 μm in radius and outer shell is perfectly match layer (PML) of thickness λ which is 1550 nm. The PML layer absorbs all radiated waves from the cavity. The disk cavity, as shown in the Figure 7.1(a), has a radius of 25 μm, height of 25 μm, refractive index *n* of 2.8, and nonlinear refractive index n_2 of 2.3×10^{-15} (m^2/W) [9]. Refractive index of air domain is taken as $n_{air} = 1$. The electrodes have 3 μm thickness. Size of the densest mesh is λ/7, which can be seen in Figure 7.1(b). The mesh size in the PML region is λ/10. In electrostatics simulation, zero charge boundary condition is applied to outer layer, and zero and V_{ext} electric potential boundary condition are applied to bottom and top electrodes, respectively. In electromagnetic wave simulation, perfect electric conductor (PEC) boundary condition is applied on the electrodes, and PML condition is applied to outer shell. Using parametric sweep property of COMSOL, we sweep the applied voltage V_{ext} parameter from 0 to 200 V. We first solve electrostatic problem and then the electromagnetic wave problem for each and every parameter.

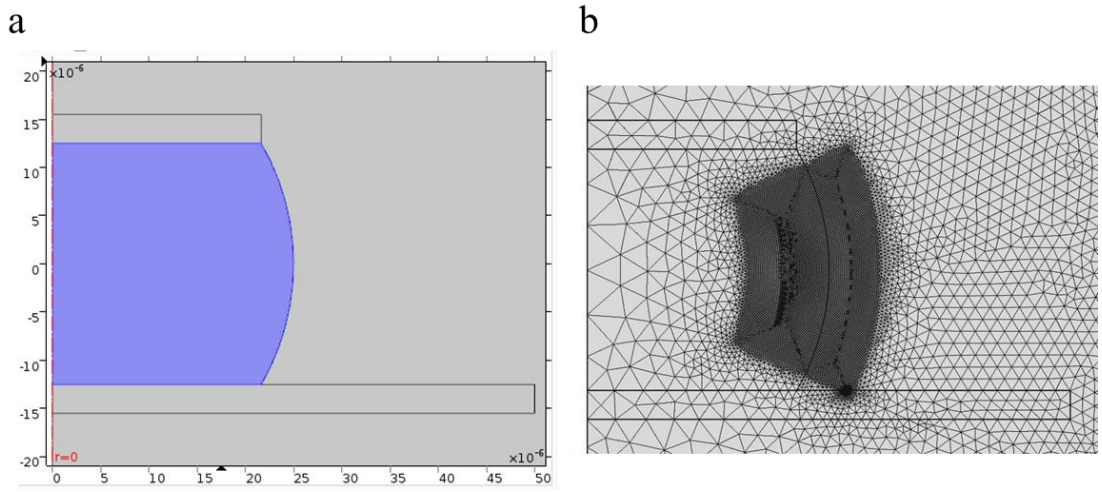

Figure 7.1: (a) A two dimensional axisymmetric simulation based on FEM is used to analyze WGMs in an electro-optic chalcogenide disk cavity, which is a sphere trimmed at both polar regions. (b) Different sizes for mesh elements are used in the simulation. The densest mesh is where WGMs are located, i.e., around equatorial region.

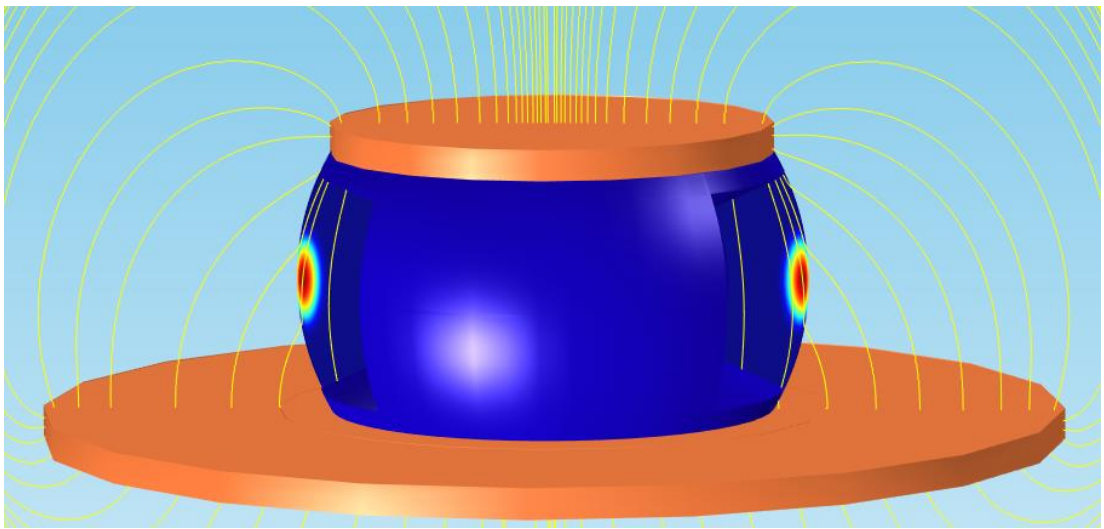

Figure 7.2: The result of the COMSOL simulation shows a fundamental WGM in an electro-optic disk cavity resonator under an applied voltage. First electric field distribution is found, which is caused by the potential difference between the gold electrode at the top and the infinite plane gold electrode at the bottom of the cavity. The electric field modifies the refractive index of the cavity due to electro-optic Kerr effect. Therefore, Maxwell Equations were solved by using refractive index $n(E_{ext})$ as a function of external electric field.

In electromagnetic wave user interface, relative permittivity ε_r is taken as user defined variable, which is actually a tensor whose matrix elements are written in terms of electric vector field $\boldsymbol{E}$ of the electrostatics problem. In order calculate relative dielectric tensor, we can start with electric displacement vector $\boldsymbol{D}$, which can be written in the presence of light wave electric field $\mathfrak{E}$ and applied field $\boldsymbol{E}$ as [116]:

$$D_i = \varepsilon_0 \sum_{j=1}^{3} \varepsilon_{i,j}(0)\, E_j + \varepsilon_0 \sum_{j=1}^{3} \varepsilon_{i,j}(\omega)\, \mathfrak{E}_j \tag{7.4}$$

where D_i is the ith component of dielectric vector $\boldsymbol{D}$ and $\varepsilon_{i,j}(\omega)$ the optical frequency relative permittivity in the presence of is applied field $\boldsymbol{E}$ and is given for a medium of third order nonlinearity by:

$$\varepsilon_{i,j}(\omega) = n_0^2(\omega)\delta_{ij} + \sum_{k=1}^{3}\sum_{l=1}^{3} \chi_{ijkl}^{(3)}(\omega) E_k E_l \tag{7.5}$$

where δ_{ij} is Kronecker delta, and third order electric susceptibility $\chi_{ijkl}^{(3)}(\omega)$ is

$$\chi_{ijkl}^{(3)} = \frac{\chi_{xxxx}^{(3)}}{3}\left[\delta_{ij}\delta_{kl} + \delta_{ik}\delta_{jl} + \delta_{il}\delta_{jk}\right] \tag{7.6}$$

for an isotropic and centrosymmetric medium [117] and $\chi_{xxxx}^{(3)} = (4/3)n_0^2\varepsilon_0 c_0 n_2$ in terms of nonlinear refractive index n_2 [118]. The term $\varepsilon_{i,j}(0)$ does not contribute to the wave Equation 4.36. Inserting Equation 7.6 into Equation 7.5, we obtain

$$\varepsilon_{i,j}(\omega) = n_0^2(\omega)\delta_{ij} + \frac{\chi_{xxxx}^{(3)}}{3}\left[\delta_{ij}\sum_{k=1}^{3} E_k^2 + 2E_i E_j\right] \tag{7.7}$$

which can also be written in matrix form as:

$$\varepsilon_{i,j}(\omega) = \tag{7.8}$$

$$= \begin{bmatrix} n_0^2 + \frac{\chi_{xxxx}^{(3)}\left[3E_x^3 + E_y^3 + E_z^3\right]}{3} & \frac{2}{3}\chi_{xxxx}^{(3)}E_xE_y & \frac{2}{3}\chi_{xxxx}^{(3)}E_xE_z \\ \frac{2}{3}\chi_{xxxx}^{(3)}E_xE_y & n_0^2 + \frac{\chi_{xxxx}^{(3)}\left[E_x^3 + 3E_y^3 + E_z^3\right]}{3} & \frac{2}{3}\chi_{xxxx}^{(3)}E_yE_z \\ \frac{2}{3}\chi_{xxxx}^{(3)}E_xE_z & \frac{2}{3}\chi_{xxxx}^{(3)}E_yE_z & n_0^2 + \frac{\chi_{xxxx}^{(3)}\left[3 + E_y^3 + 3E_z^3\right]}{3} \end{bmatrix}$$

For our case, E_y = 0. This matrix form is defined as a variable in COMSOL electromagnetic wave simulation to explicitly connect relative electric permittivity $\varepsilon_{i,j}(\omega, E)$ of the material to electric vector field $\boldsymbol{E}$ found in electrostatics simulation. Electromagnetic wave solutions are given in Figure 7.2 and Figure 7.3.

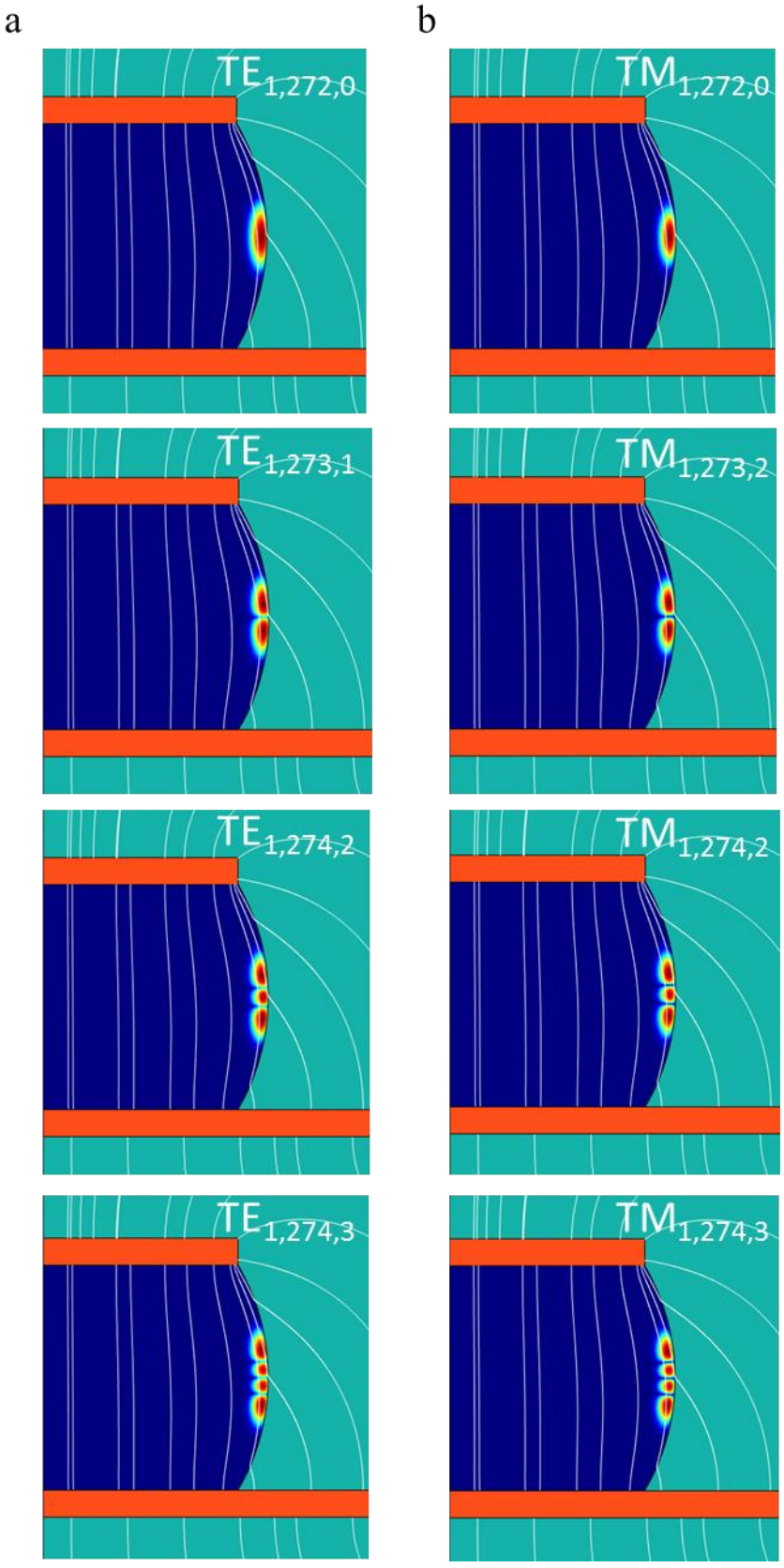

Figure 7.3: Figure shows WGMs of different mode order (*q*, *l*, *l*-*m*) for (a) TE and (b) TM polarizations inside the disk cavity under an applied electric field.

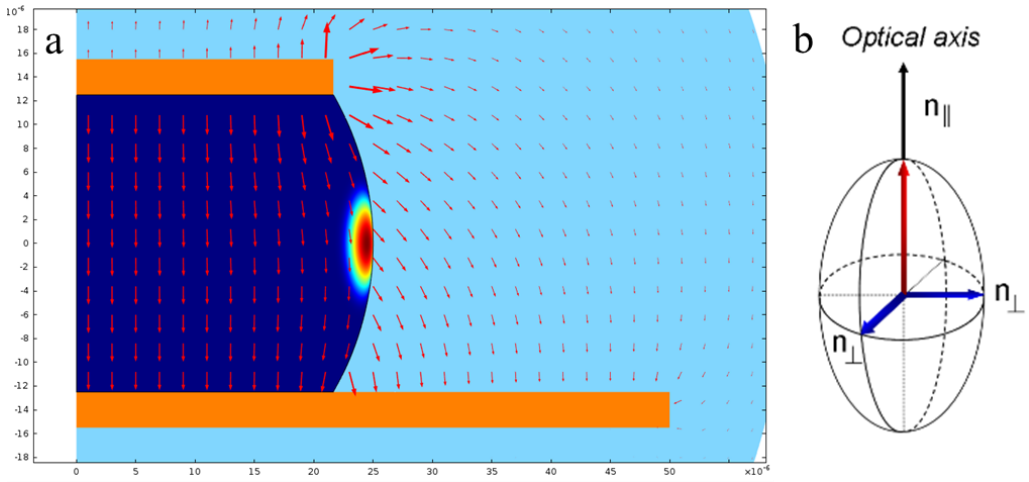

Figure 7.4: (a) Distribution of electric field vectors between gold electrodes and a fundamental WGM exposed to different refractive indices for TE and TM modes whose electric fields are parallel and perpendicular to the cavity surface, respectively. (b) An isotropic disk cavity under an electric field behaves as an anisotropic uniaxial crystal of extraordinary $n_{\parallel}$ and ordinary $n_{\perp}$ refractive indices.

Under an applied field (see Figure 7.4(a)), isotropic and centrosymmetric material behaves as an anisotropic uniaxial crystal whose extraordinary $n_{||}$ and ordinary refractive indices $n_{\perp}$ as shown in Figure 7.4(b) are:

$$n_{\parallel} \approx n_0 + \frac{\chi^{(3)}_{xxxx}}{2n_0}\left|\vec{E}\right|^2 \tag{7.9}$$

and

$$n_{\perp} \approx n_0 + \frac{\chi^{(3)}_{xxxx}}{6n_0}\left|\vec{E}\right|^2 \tag{7.10}$$

and optical axis is in the direction of electric field vector $\boldsymbol{E}$. Distribution of refractive index change $\Delta n_{||}$ at an applied voltage of 100 V is given in Figure 7.5 and relative resonance wavelength shift for TE and TM modes are given in Figure 7.6.

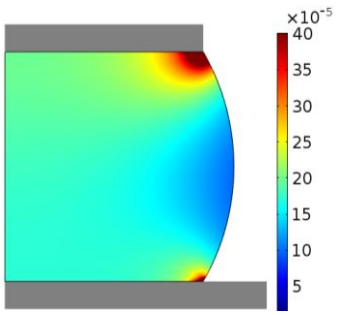

Figure 7.5: Distribution of extraordinary refractive index change $\Delta n_{||}$ at an external voltage of 100 V.

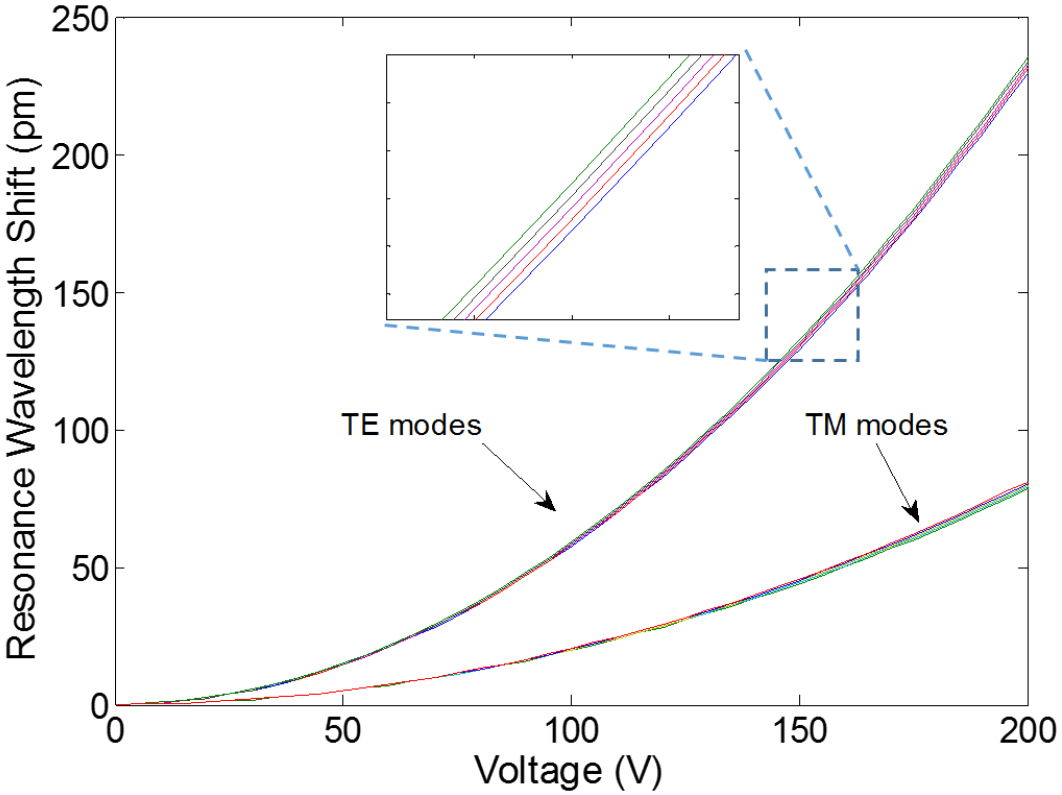

Figure 7.6: Results of COMSOL simulation show that the relative resonance wavelength shifts have different quadratic dependence on the applied DC voltage for TE and TM polarizations. As voltage increases, WGMs split due to their different spatial mode distributions and asymmetry of the electric field inside the cavity.

7.3. Fabrication of Electro-Optic Photonic Devices

Fabrication and integration of chalcogenide disk cavities with electrodes, as schematically given in Figure 7.7, starts with normal procedure of obtaining microspheres inside a chalcogenide core PES cladding fiber by triggering Plateau-Rayleigh Instability (see Chapter 6). After a simple sandpapering operation for the bottom part of the fiber and cleaning process with isopropyl alcohol in an ultrasonic bath, it is transferred onto a metal coated (5 nm Cr and 100 nm gold) substrate. Subsequently, substrate and fiber are exposed to a temperature of 260 °C in a temperature controlled oven to promote adhesion of chalcogenide cavities and fiber encapsulation to the gold coated surface of the substrate. After sample is cooled down, a protective organic layer of colorless nail polish, which actually consists of a film-forming polymer (nitrocellulose), is applied on the entire surface of fiber and the substrate. The reason behind this extra step is three advantages harnessed by the process. First of all, protective layer gives extra mechanical strength to the fiber attached on the surface against the following second sandpapering process, and keeps metal surface of the substrate from getting dirty due to sandpapering residues as well as it protects metal surface from getting scratched.

A second sandpapering operation can be now applied to the top of the integrated fiber for revealing the surface of the disk cavity (see Figure 7.8(a)). Later, protective nail polish and the polymer fiber can be removed by Tetrahydrofuran (THF) and DCM, respectively, to obtain integrated disk cavities on a gold coated surface as shown in Figure 7.8(b, c). Scanning Electron Microscope (SEM) micrographs in Figure 7.9 show that procedure up to this point is quite feasible, however extra steps are required to obtain circular metal electrodes on the disk cavities. So, after second sandpapering operation, gold metal can be deposited on the trimmed fiber surface and lift-off method can be used to create circular electrodes on the top of disk cavities by removing all polymer by organic solvents. Optical microscope images showing every step for a fiber with embedded microdisk cavities can be seen in Figure 7.10. However, during polymer dissolution in an organic solvent, it is observed that gold coating (even as thin as 10 nm) is not torn apart from the circular interfaces and instead falls on the disk cavities as a cover (see Figure 7.11) and it is not possible to achieve a successful lift-off which results into proper circular electrodes on disk surfaces only by this last step.

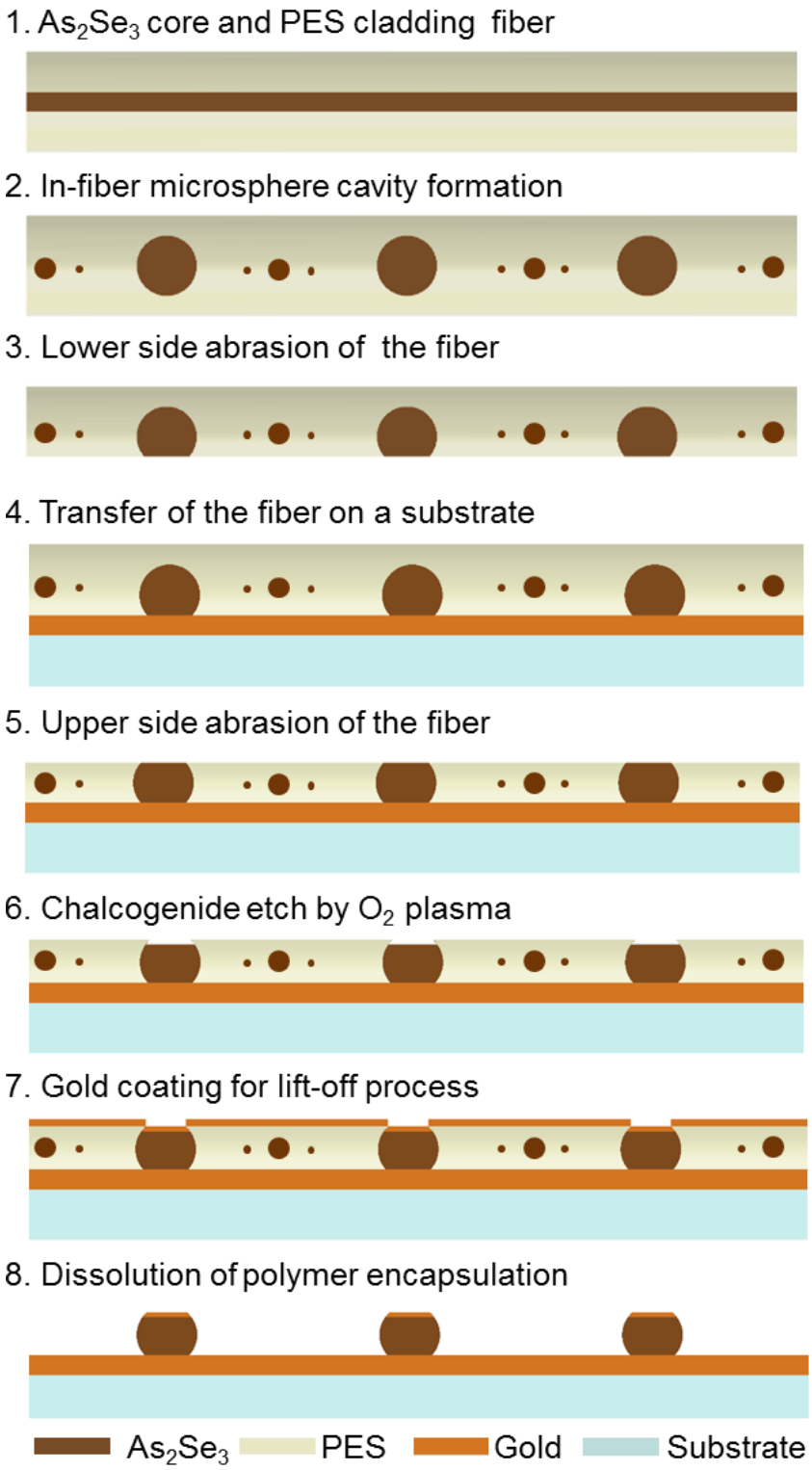

Figure 7.7: Fabrication and integration steps of an electro-optic photonic device based on chalcogenide WGM disk cavity. Process starts with a chalcogenide core polymer cladding fiber and ends with an electro-optic photonic device consists of WGM disk cavity resonator between two integrated electrodes.

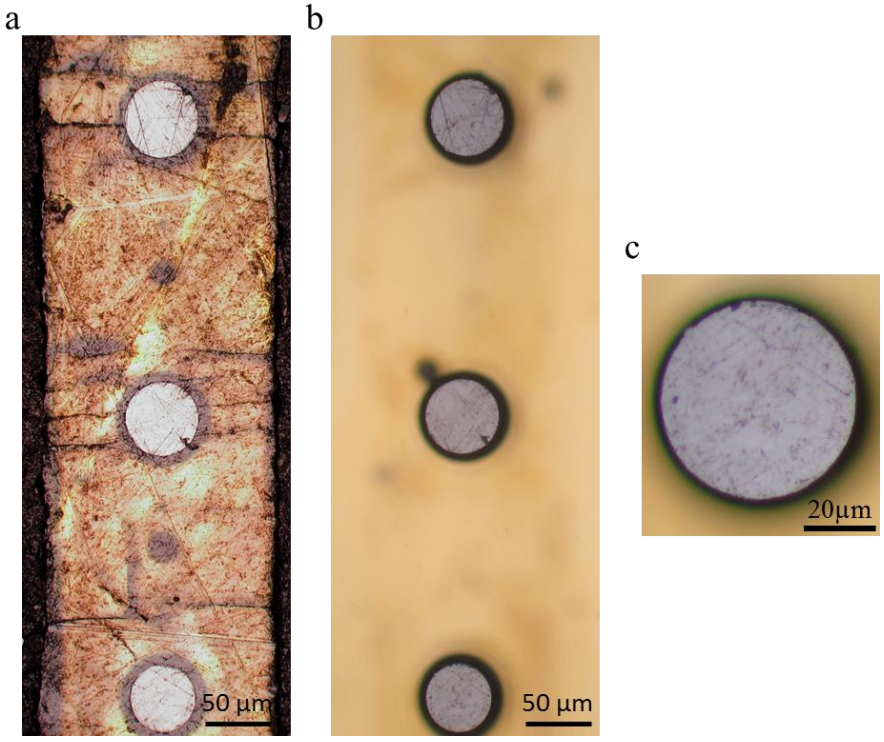

Figure 7.8: Optical microscope images of the disk cavities (a) before and (b) after PES polymer encapsulation is removed by DCM. (c) Close-up image of a single cavity from top.

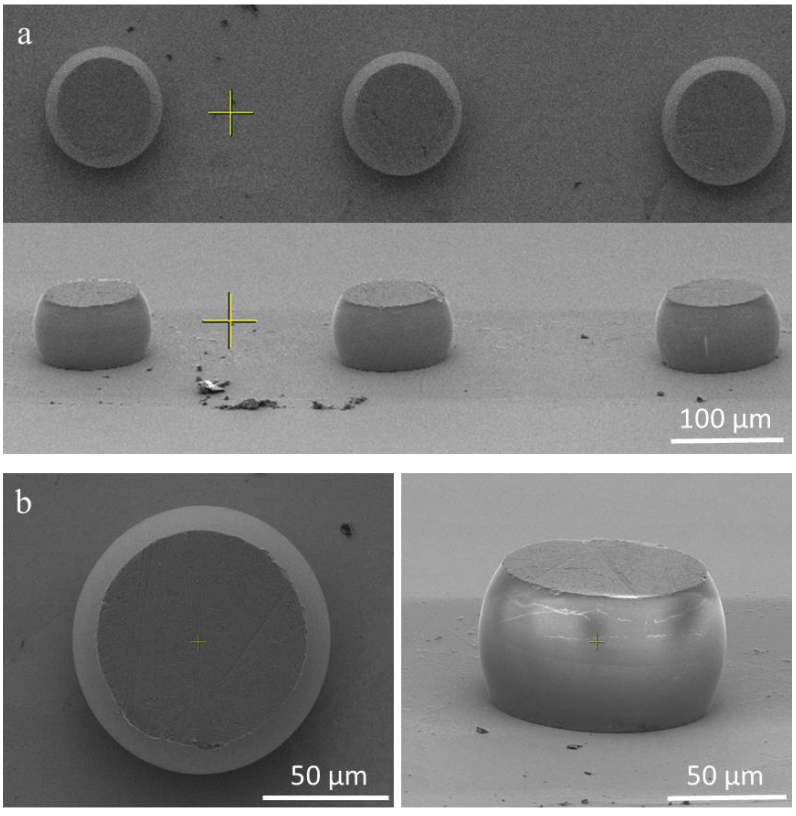

Figure 7.9: (a) SEM micrographs of (a) a disk cavity resonator array and (b) a single disk cavity from top and side views.

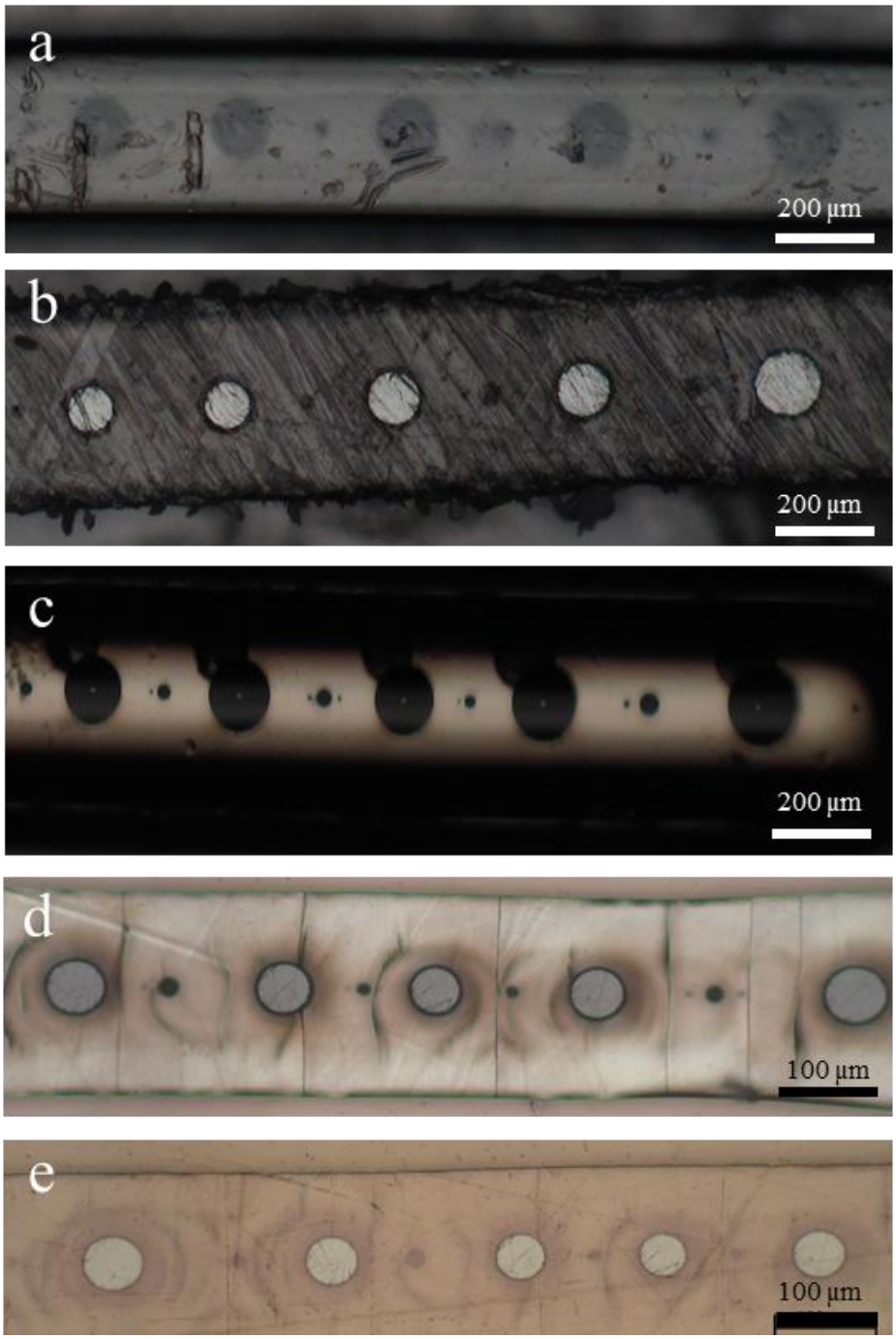

Figure 7.10: Fabrication and integration process of chalcogenide disk cavities on a gold coated substrate. (a) Process starts with a fiber encapsulating sphere cavities. (b) Lower side of the fiber is removed by a sandpapering process and then (c) attached onto a gold coated substrate by heating and pressing at a temperature of 260 °C in a hot oven. (d) Second sandpapering operation on the upper surface of the integrated fiber. (e) 5 nm Cr and 15 nm gold sputtering on the upper surface of the integrated fiber for lift-off process.

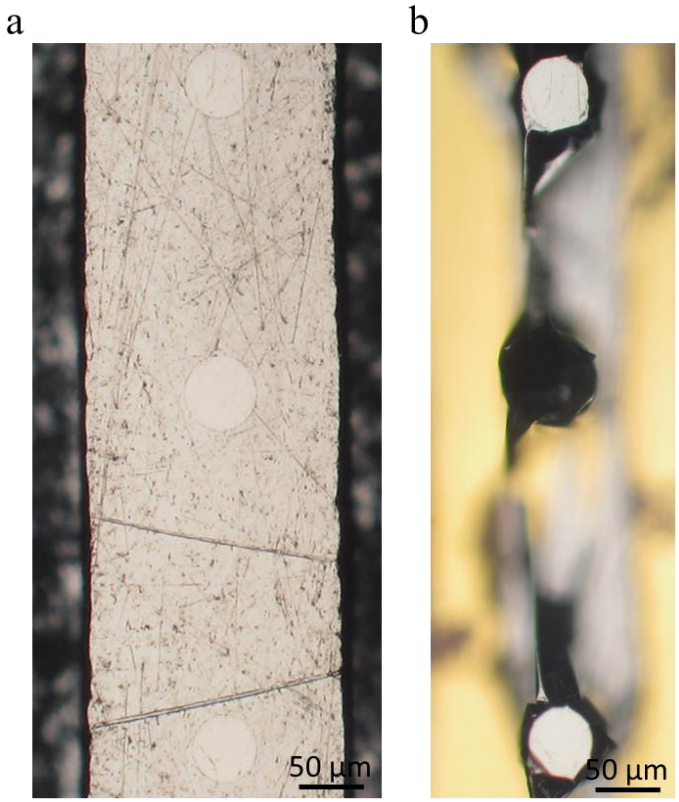

Figure 7.11: Optical microscope images show a metal coated fiber encapsulating disk cavities (a) before and (b) after the dissolution of polymer by organic solvents resulting into an unsuccessful lift of process.

We need to etch polymer encapsulation or chalcogenide disks to enable a successful lift-off process. We preferred to etch chalcogenides to ensure that there would be a level difference between disk surface and polymer fiber surface resulting into a shadowing effect due to the circular polymer edges with negative slope. The exposed part of As_2Se_3 microdisks were partially etched with O_2 plasma, in order to facilitate the lift-off process following the consequent metal deposition, using a plasma asher (Nanoplas DSB 6000). The power used was 200 W, produced by an inductively coupled plasma generator operating at 13.56 MHz. The O_2 flow rate was 30 sccm, chamber pressure was 50 mTorr, and the duration of the etching was 2 min. The Lift-off process was successful at this time, and results can be seen in Figure 7.12(a). Evolution of the surface of a single chalcogenide disk cavity from O_2 plasma etch to lift-off process in THF solution is presented in Figure 8.12(b-d). THF attacks aggressively on the nail polish polymer on contrary to the slow etching of the polymer fiber, which facilitates the lift-off process. SEM micrographs of disk cavities with circular gold electrodes on the top are given in Figure 7.13.

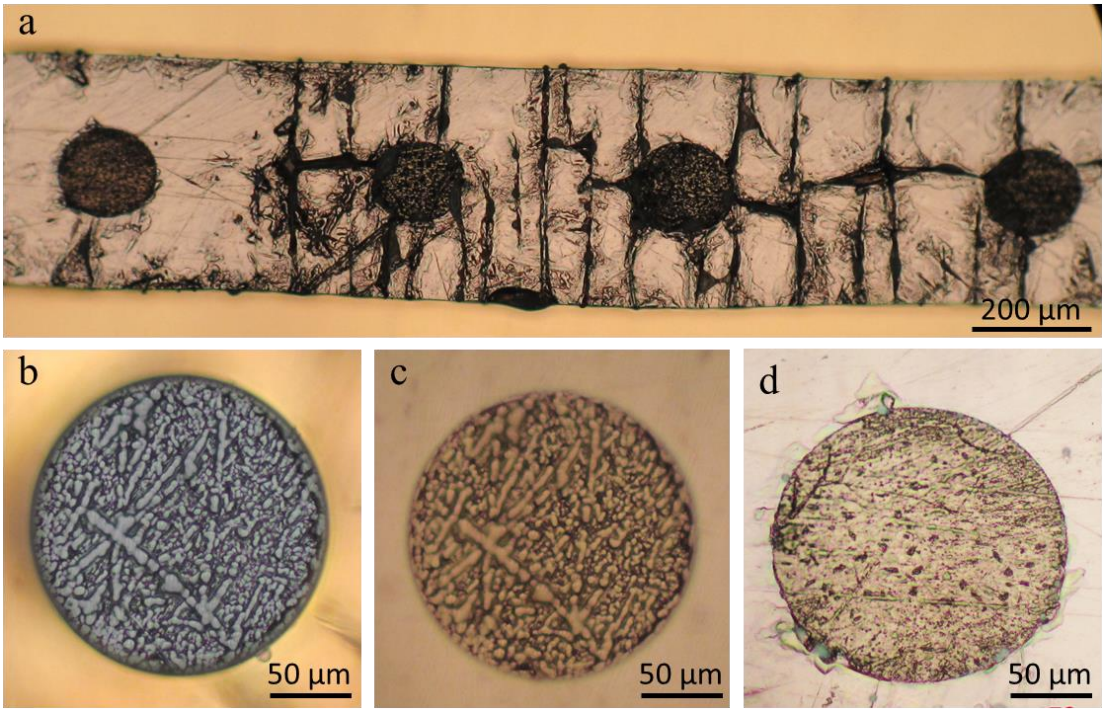

Figure 7.12: (a) Optical microscope image shows surface of a fiber with embedded disk cavities after the lift-off process. Sequential images show a top surface of a disk cavity after (b) O_2 plasma etch, (c) gold metal sputtering and (d) lift-off process by THF.

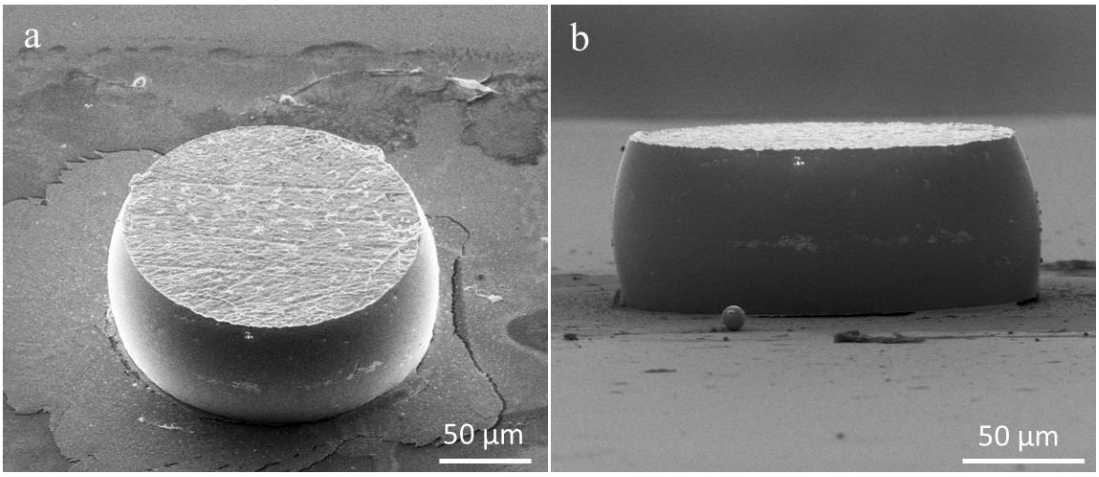

Figure 7.13: SEM micrographs of a disk cavity with a gold coating on the top surface from a (a) perspective and (b) side view.

Chapter 8
Tapered Chalcogenide Fibers as High Index Evanescent Optical Couplers

8.1. Introduction

Tapered silica fibers have been extensively exploited as ideal and efficient evanescent couplers for coupling light into WGMs of resonators. However, they are only applicable to resonators with refractive indices similar to silica. They cannot be used for WGM resonators made of higher index glass or crystalline material such as diamond [71], chalcogenides [86], and $LiNbO_3$ [119]. To solve this problem, fibers made of higher index glasses are drawn much interest since they can be tapered at lower temperatures using electrical heaters [120, 121] or photo-induced fluidity[122]. High index tapers have been utilized in nonlinear optical applications such as supercontinuum generation [11, 123] and multicolor up-conversion [124], taking advantage of their higher nonlinear refractive indices n_2 and reduced effective mode area A_{eff} due to the tapering. Unfortunately, unclad and unsupported fibers of chalcogenides are very fragile because of their inferior mechanical properties compared to silica. Therefore, chalcogenide fibers with thermoplastic polymer cladding have been fabricated and shown to be robust tapers [125-127].

Tapered chalcogenide fibers are promising candidates as evanescent couplers to couple light into WGMs of resonators with high index materials (n >1.44) unless some solutions are found to resolve their mechanical instability in tapered form and the difficulty of splicing them to silica fibers, which are usually external connectors. In this chapter, steps towards solving these issues have been taken and the ideal solution rising from the combinations of different tapering approaches is demonstrated at the end.

8.2. Tapering Chalcogenide Core Polymer Cladding Fibers

At first, we tried to taper chalcogenide core polymer cladding fibers we produced. We built a custom electrical heater, as shown in Figure 8.1(a), with longitudinal windings of nickel chrome wires around a glass tube. The glass tube clamped by a Teflon holder, enables the entrance of the as-drawn fiber and exit of the tapered fiber through a side opening. We can reach temperatures up to 220 °C by 210 Volt DC tunable power source. Set up used for tapering process, which is shown in Figure 8.1(b), is actually same set up we used for tapering silica fibers except the electrical heater. Tapered fiber has bumps on the sides as shown in Figure 8.1(c), due to built-in stress in polymer cladding released after heating.

We could not obtain continuous tapered fibers of Step 1, generally resulting into break-up of core as shown in Figure 8.2. It is expected to be due to the structural instability occurring at high tensile stress and low cladding core ratio [27]. However one side tapering is possible when core breaks up in the middle and makes contact with the hot surface of the heater, resulting in smooth tapers as can be seen in Figure 8.3(a). With single core fibers (Step 2) of relatively thicker cladding, a smaller amount of tapering is enough to taper the core down to 1 μm as shown in Figure 8.3(b). For this case, splicing to silica fiber is very challenging because of small core diameter and multimaterial nature of the fiber.

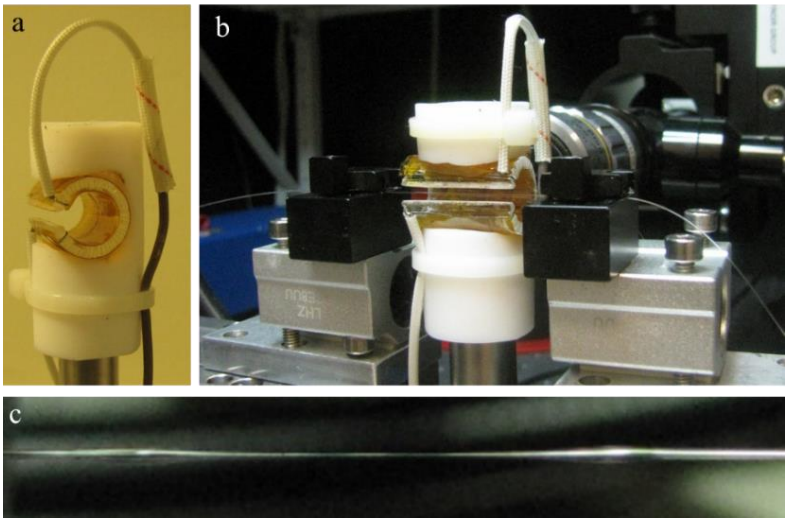

Figure 8.1: (a) Custom made electrical heater with side opening for entrance and exit of the fiber, and observation during tapering process. (b) Set up used for tapering chalcogenides. (c) Close-up picture of tapered chalcogenide core PES cladding fiber.

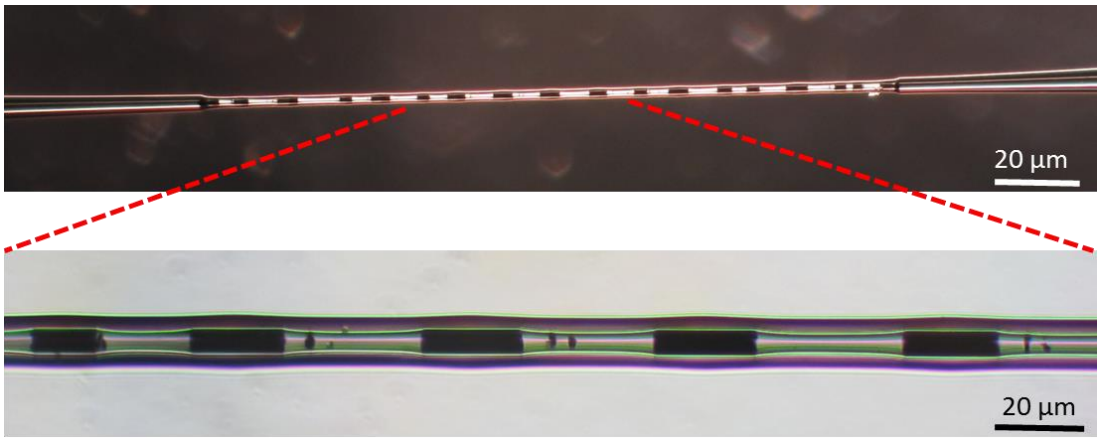

Figure 8.2: Formation of cylindrical chunks of matter inside the tapered region due to low temperature and tensile stress caused by tapering.

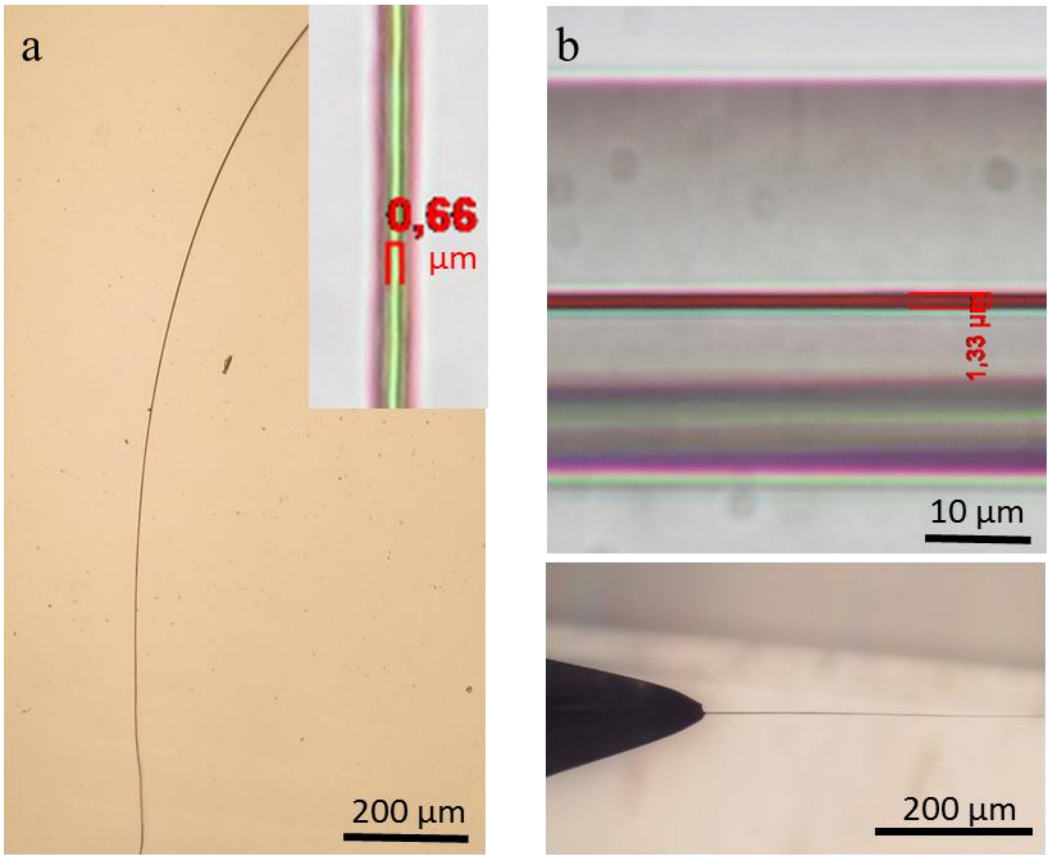

Figure 8.3: (a) Tapering of Step 1 chalcogenide fiber with thermoplastic polymer having one side contact with inner surface of heater, results in good tapering, but only for one side. (b) Tapering of a single core chalcogenide fiber (Step 2) with a thicker cladding and a free standing chalcogenide wire after removal of PES encapsulation by organic solvents.

8.3. Direct Drawing of Microwires from Bulk ChGs

Another approach we tried for obtaining tapered chalcogenide fibers is direct drawing from bulk glasses as shown for other materials before [128]. On the contrary to the expectations, we succeeded to obtain tapered chalcogenide fibers attached to silica un-tapered and tapered fibers, as shown in Figure 8.4 and Figure 8.5, respectively. Process starts with cleaving silica fiber to achieve a clean and flat surface. In an oven with a temperature of 260 °C, the cleaved silica fibers can adhere to the surface of a bulk chalcogenide glass quite easily and retraction of fiber results in chalcogenide tapers with super elastic mechanical properties. We observed good adhesion of chalcogenide to silica fibers, which is a requirement for good splicing. Maximum size of the taper correlates with the diameter of the silica fiber tip. Using this method, tapered chalcogenide fibers attached to a silica fiber can be easily produced, however, optical coupling necessitates biconical tapers to couple light in and out of the cavity for the most of the applications.

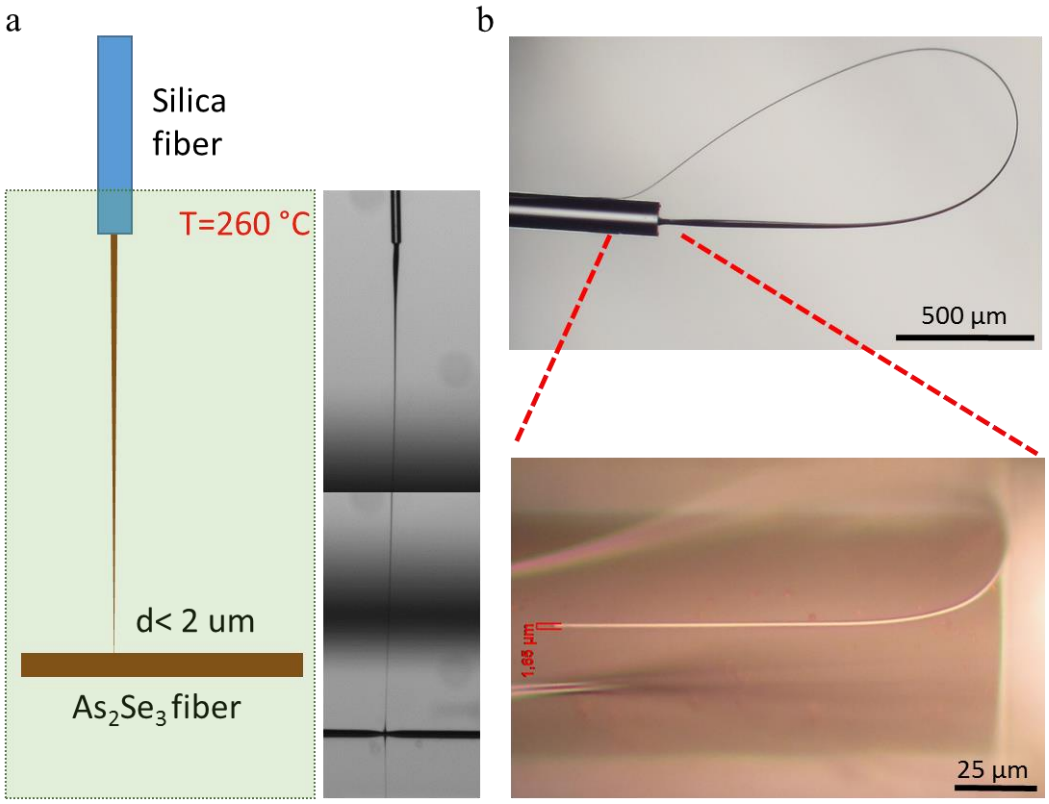

Figure 8.4: (a) Chalcogenide microwires can be easily directly drawn from bulk glass inside an oven at 260 °C being attached to a tip of cleaved silica fiber. (b) Tip of tapered wires is of order of 1 micron.

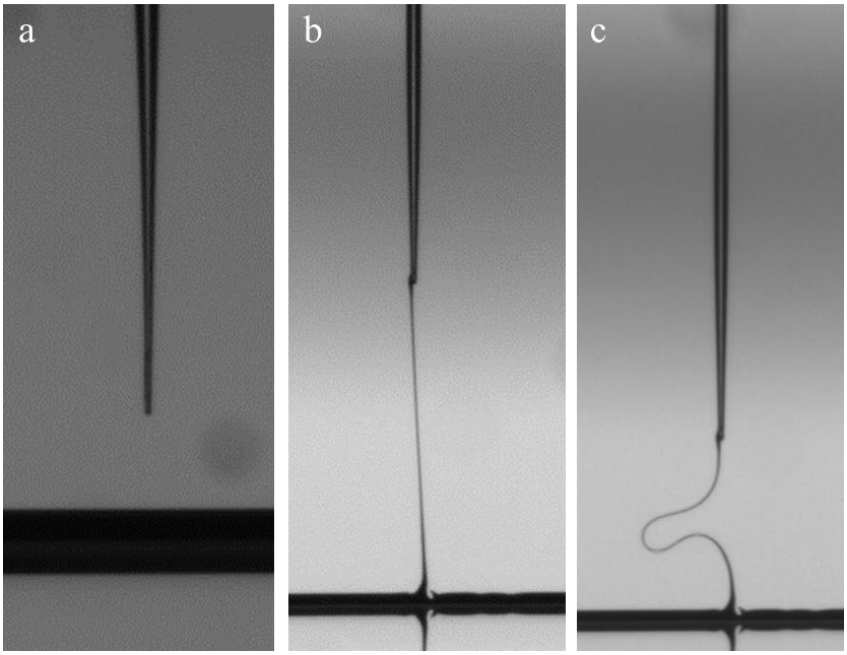

Figure 8.5: Production of microwires on the tip of a tapered silica fiber by direct drawing from bulk glass with steps of (a) approach and (b) retraction. (c) Chalcogenide tapered wire on the tip of a silica fiber tip shows super elastic properties.

8.4. Tapering ChGs between Silica Fibers Tips

An ideal solution for the chalcogenide tapering problem was found by combining the experiences learned from previous approaches and being inspired by a similar fabrication method used to bridge telluride glass between two tapered silica fibers [124]. This is accomplished by drawing chalcogenide glass bilaterally inside the custom made electrical heater by two tapered silica fibers already connected to a laser source at one end and power meter at the other end. Tapering processed is also monitored by transmission signal, and long range microscopes from the side opening of the heater. Splicing to silica fibers in the beginning of process are spontaneously made due to surface adhesion of chalcogenide glass in softened state. Tapering length is very short, which is on the order of 400 µm, so mechanical weakness is not a problem anymore since material can hang itself by tensile stress under the force of gravity. Actually, the best advantage of the process is its repeatability. Even any break-up occurs during tapering, loose ends with some chalcogenide glass left on both or either of them, reunite when they touch again forming an intact wire, so the process can continue from the tapering step. During process, inert gas atmosphere can also be used to prevent surface oxidation of chalcogenides.

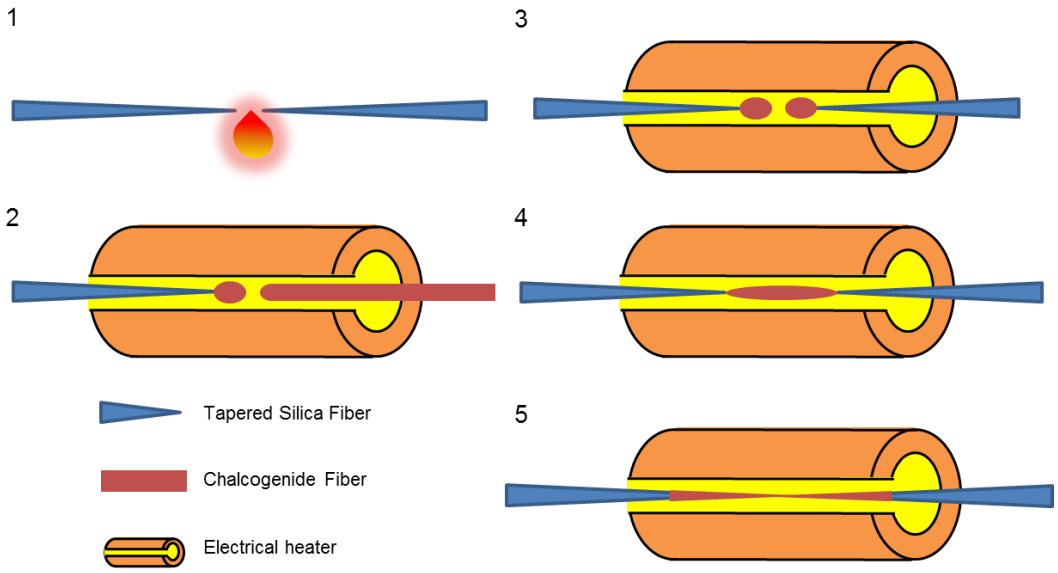

Figure 8.6: Schematic of tapering chalcogenide fibers between silica tapered fiber tips with five basic steps: 1. Tapering and cleaving silica fiber, 2. Attaching some amount of chalcogenide glass on the cleaved tips inside heater one by one, 3. Alignment of silica fibers inside the electrical heater, 4. Moving silica fiber closer and merging chalcogenide glasses between two fiber tips. 5. Tapering suspended material by drawing silica fibers away.

Chalcogenide tapering process as shown schematically in Figure 8.6, starts with conventional silica fiber tapering process as described in Chapter 5.4. In this step, connections of silica fiber ends to the laser source and to the optical power detector are established and can be preserved until the end of all process maintaining same insertion losses during the second tapering. After tapering the silica fiber with 6 mms of total tapering length, cleaving operation is accomplished by scoring the surface of the fiber under tensile stress in the thinnest part (20 µm in diameter) with a sharp blade positioned accordingly across the fiber as shown in Figure 8.7. Cleaved tips of tapered and un-tapered silica fibers can be seen in Figure 8.8. *In-situ* cleaving process is followed by attaching some amount of chalcogenide glass onto both cleaved tip surfaces, which can be done in a separate temperature controlled oven (see Figure 8.9(a)) or inside the electrical heater (see Figure 8.9(b)) which in this case there is no need to break silica fiber's optical couplings to external devices. We pursuit both methods, however, optical characterization was done with the second method allowing *in-situ* attaching of chalcogenide glass on tips inside electrical heater. Chalcogenide glasses attached to fiber tips are then moved closer to each other allowing merging of materials between fibers' cleaved facets.

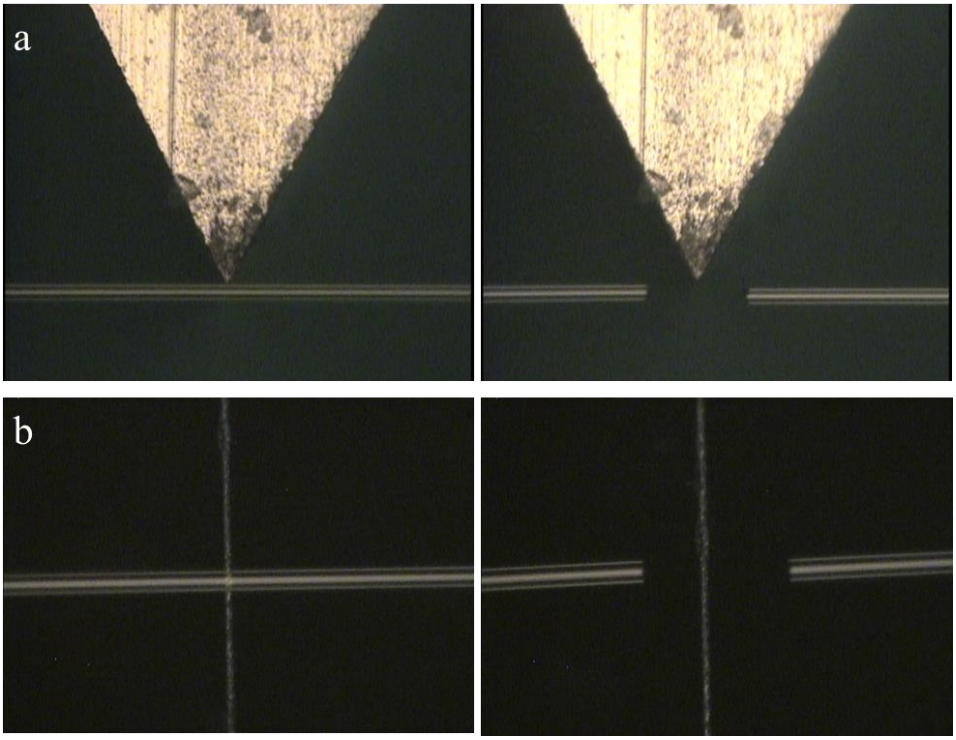

Figure 8.7: Cleaving tapered silica fibers. (a) Side view and (b) down view of cleaving process with a sharp blade. Scoring surface of fiber is enough to cleave tapered fibers under tensile stress.

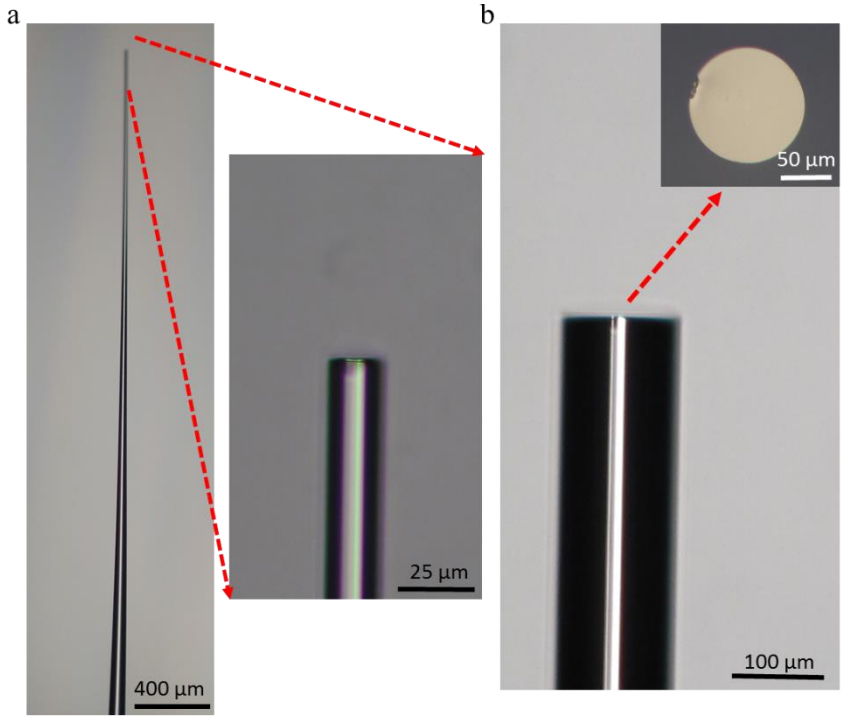

Figure 8.8: Cleaved tips of (a) tapered and (b) normal fiber before attachment of chalcogenide glass.

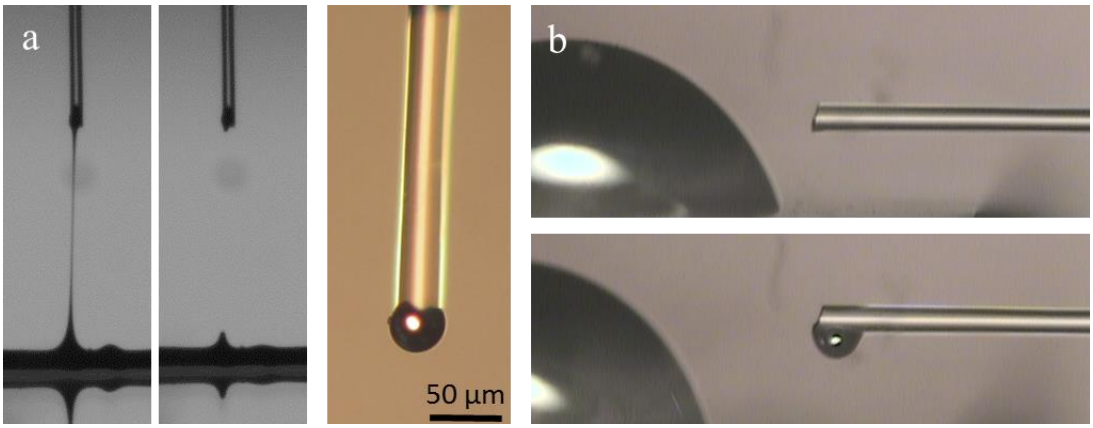

Figure 8.9: Two different ways of attaching chalcogenide glass on silica fiber tips can be realized a) in temperature controlled oven or b) inside the electrical heater, which is advantageous since there is no need to move tapered silica fibers already connected to laser source and power meter at the silica fiber tapering process.

Tapering can be now started by drawing silica fibers bilaterally, which transforms the suspended material into tapered chalcogenide fiber between silica tips. Two samples of chalcogenide fiber tapering process can be seen in Figure 8.10 and Figure 8.11. For the second case, we recorded both transmission spectra of silica tapering and chalcogenide tapering steps, which are given in Figure 8.12. Initially, there are only insertion losses (-4 dB) caused by butt-to-butt couplers and scattering losses through the silica fiber, and silica fiber tapering related loss (-2 dB) due to non-adiabatic tapering. After tapering chalcogenide fiber between cleaved flat surfaces of silica fiber, a maximum level of insertion loss (-15 dB) and some relative dips of extra 10 dB loss were observed. The excess loss of second tapering is believed to belong to Fresnel losses at both interfaces and chalcogenide tapering losses. Relative dips transmission (-10 dB) are caused by the interference of beating higher modes with fundamental mode, due to non-adiabaticity of second tapering. These beating of multi-modes can be eliminated by more adiabatic tapering and increasing the amount of material suspended between silica fiber tips.

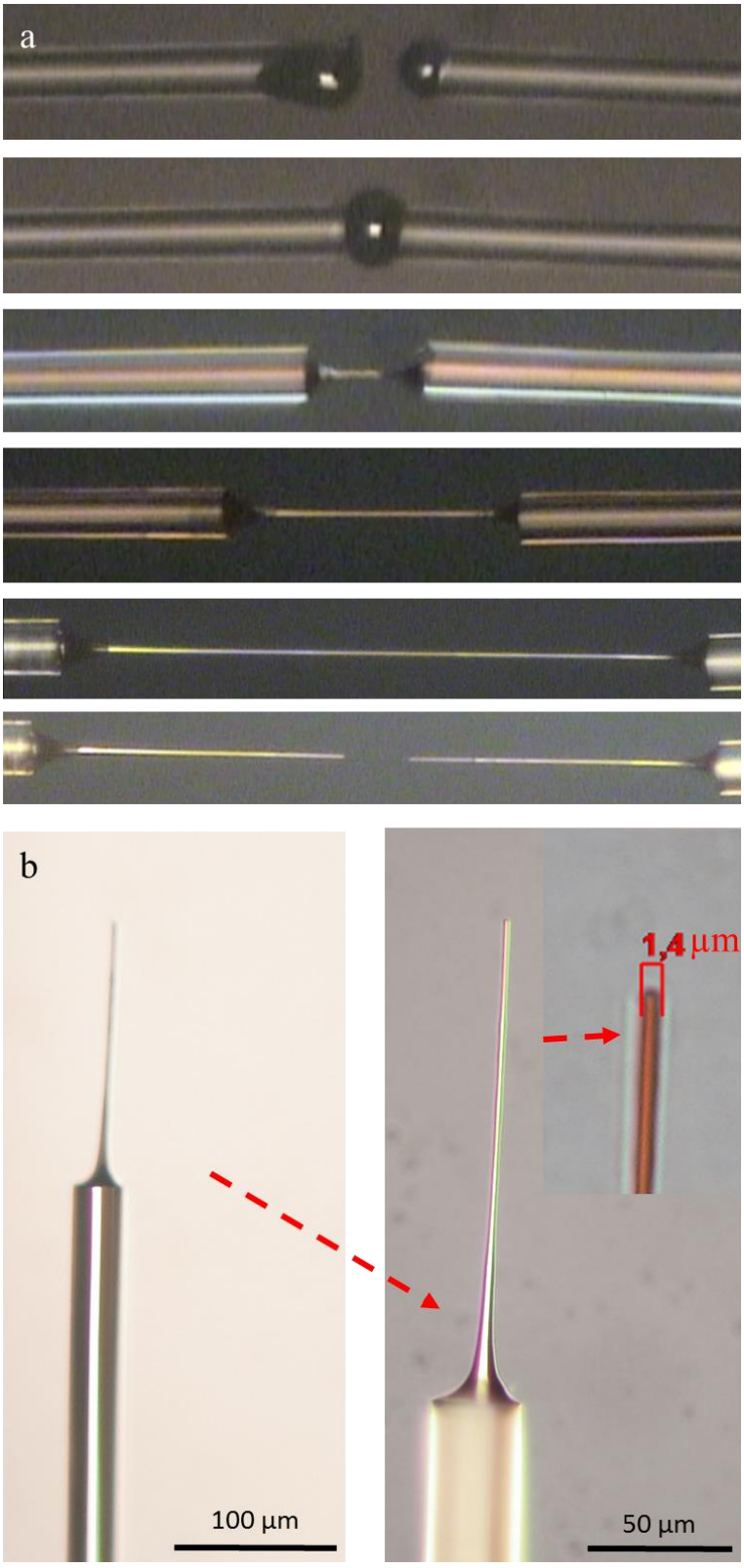

Figure 8.10: (a) Evolution of chalcogenide tapering process starts with two silica fibers with some chalcogenide glass on them and results into tapered chalcogenide fiber between two silica tips being apart. (b) Optical microscope image of intentionally broken tapered chalcogenide fiber spliced to a silica tapered fiber

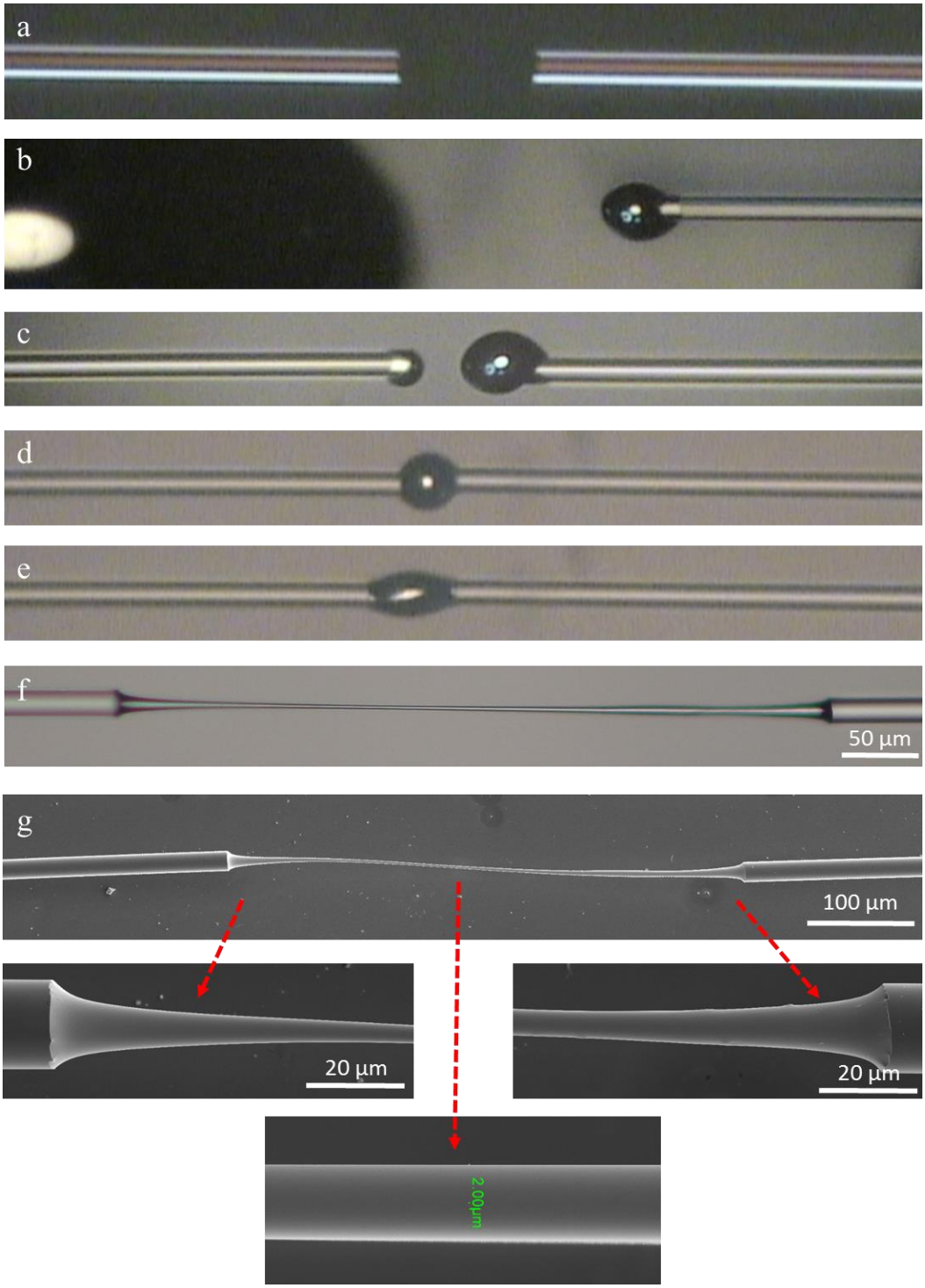

Figure 8.11: Steps of tapering chalcogenide between cleaved silica fiber tips. (a) Tapering and cleaving silica fibers. (b) Attaching chalcogenide glass by inserting silica tips into bulk chalcogenide glass. (c) Alignment of silica fiber tips inside the electrical heater. (d) Merging chalcogenide glasses between both tips moving closer to each other. (e) Initial stretch of the merged chalcogenide glass to ensure correct working temperature. (f) Stretching suspended chalcogenide glass which transforms into tapered fiber between silica tips being apart. (g) SEM micrograph of the produced chalcogenide fiber between silica tips showing smooth junction points and tapered region of 2 µm radius.

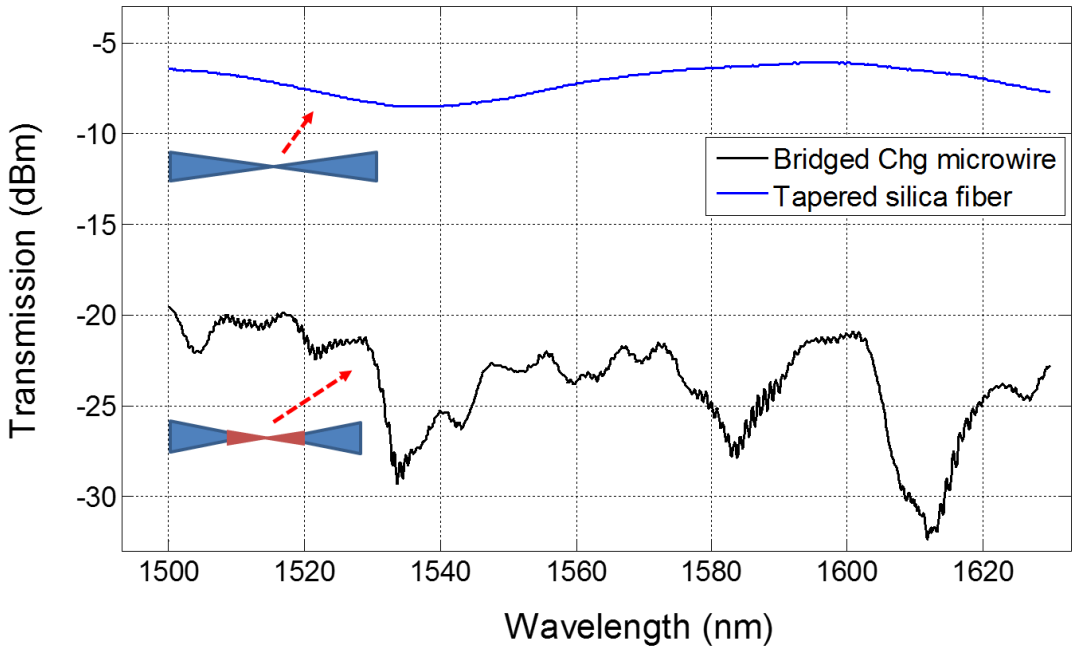

Figure 8.12: Transmission spectra of tapered silica fiber before in-situ cleaving (upper line) and of chalcogenide tapered fiber suspended between two tapered silica fibers (lower line). Large dips of transmission signal is caused by the interference of beating multi-modes.

Chapter 9

Conclusions and Future Work

We have demonstrated a photodetection device using chalcogenide nanowires, and a global integration methodology for large area applications. However, this work can be expanded to develop flexible devices based on nanowires. Enhanced optical properties of nanowires, due to the nanoscale effects, can be harnessed in this way by applications which are not feasible before.

Optical resonators will play a vital role in the miniaturization of future photonic integrated circuits. What we show in this thesis is a low cost and high throughput fabrication of on-chip chalcogenide optical resonators with various geometries. Optical properties of the cavities are satisfactory for photonics applications, although some optimization in the material synthesis can further lower the absorption related losses.

Combination of Wavelength Division Multiplexing (WDM) and Time Division Multiplexing (TDM) modulation methods can solve the data speed problem the world face today. A simple scenario is for example: as a photonic building block, a microresonators can select wavelength multiplexed data channel via tunable filtering using electro-optical effect and then demodulate time multiplexed data using all-optical processing. Electro-optical properties of chalcogenides, which are capable of all-optical processing, have been long ignored, therefore, we have investigated via simulations and demonstrated fabrication of electro-optical WGM resonator based chalcogenide photonic devices, which can utilized in novel applications such as tunable non-classical light source, millimeter wave RF receivers, optoelectronic oscillators, tunable frequency combs.

We also demonstrated an ideal solution for the fabrication of tapered chalcogenide fibers combining previous experiences gained through the two previous approaches followed. Tapered silica fibers have a lot of applications but they are not efficient for high index material cavities. Our solution is to use bridged chalcogenide tapers between silica fibers, where aforementioned problems will be circumvented. We expect that photonics community will take advantage of this new tapers using them in applications where high index prism couplers have been employed hitherto. These tapered fibers can also be used for the generation of supercontinuum.

Bibliography

[1] S. Kumar, B. R. Mehta, S. C. Kashyap, and K. L. Chopra, "Amorphous-Chalcogenide Thin-Film Schottky-Barrier (Bi/As2se3-Bi) Solar-Cell," *Applied Physics Letters*, vol. 52, no. 1, pp. 24-26, 1988.

[2] D. B. Talley, L. B. Shaw, J. S. Sanghera, I. D. Aggarwal, A. Cricenti, R. Generosi, M. Luce, G. Margaritondo, J. M. Gilligan, and N. H. Tolk, "Scanning near field infrared microscopy using chalcogenide fiber tips," *Materials Letters*, vol. 42, no. 5, pp. 339-344, 2000.

[3] S. Hudgens, and B. Johnson, "Overview of phase-change chalcogenide nonvolatile memory technology," *Mrs Bulletin*, vol. 29, no. 11, pp. 829-832, 2004.

[4] B. J. Eggleton, B. Luther-Davies, and K. Richardson, "Chalcogenide photonics," *Nature Photonics*, vol. 5, no. 3, pp. 141-148, 2011.

[5] S. R. Ovshinsky, "Optically Induced Phase-Changes in Amorphous Materials," *Journal of Non-Crystalline Solids*, vol. 141, no. 1-3, pp. 200-203, 1992.

[6] B. Yu, X. Sun, S. Ju, D. Janes, and M. Meyyappan, "Chalcogenide-nanowire-based phase change memory," *IEEE Transactions on Nanotechnology*, vol. 7, no. 4, pp. 496-502, 2008.

[7] V. Ta'eed, N. Baker, L. Fu, K. Finsterbusch, M. Lamont, D. Moss, H. Nguyen, B. Eggleton, D. Choi, S. Madden, and B. Luther-Davies, "Ultrafast all-optical chalcogenide glass photonic circuits," *Optics Express*, vol. 15, no. 15, pp. 9205-9221, 2007.

[8] B. J. Eggleton, V. G. Ta'eed, and B. Luther-Davies, "Chalcogenide glass - Advanced for all-optical processing," *Photonics Spectra*, vol. 41, no. 9, pp. 88-90, 2007.

[9] A. Zakery, and S. R. Elliott, "Optical properties and applications of chalcogenide glasses: a review," *Journal of Non-Crystalline Solids*, vol. 330, no. 1-3, pp. 1-12, 2003.

[10] G. Elliott, G. Murugan, J. Wilkinson, M. Zervas, and D. Hewak, "Chalcogenide glass microsphere laser," *Optics Express*, vol. 18, no. 25, pp. 26720-26727, 2010.

[11] E. Magi, L. Fu, H. Nguyen, M. Lamont, D. Yeom, and B. Eggleton, "Enhanced Kerr nonlinearity in sub-wavelength diameter As2Se3 chalcogenide fiber tapers," *Optics Express,* vol. 15, no. 16, pp. 10324-10329, 2007.

[12] F. Vanier, M. Rochette, N. Godbout, and Y. Peter, "Raman lasing in As2S3 high-Q whispering gallery mode resonators," *Optics Letters,* vol. 38, no. 23, pp. 4966-4969, 2013.

[13] A. R. Hilton, "Optical properties of chalcogenide glass," *Journal of Non-Crystalline Solids,* vol. 2, pp. 28-39, 1970.

[14] J. S. Sanghera, L. B. Shaw, L. E. Busse, V. Q. Nguyen, P. C. Pureza, B. C. Cole, B. B. Harbison, I. D. Aggarwal, R. Mossadegh, F. Kung, D. Talley, D. Roselle, and R. Miklos, "Development and infrared applications of chalcogenide glass optical fibers," *Fiber and Integrated Optics,* vol. 19, no. 3, pp. 251-274, 2000.

[15] V. G. Ta'eed, N. J. Baker, L. Fu, K. Finsterbusch, M. R. E. Lamont, D. J. Moss, H. C. Nguyen, B. J. Eggleton, D. Y. Choi, S. Madden, and B. Luther-Davies, "Ultrafast all-optical chalcogenide glass photonic circuits," *Optics Express,* vol. 15, no. 15, pp. 9205-9221, 2007.

[16] M. Pelusi, V. Ta'eed, L. Fu, E. Magi, M. Lamont, S. Madden, D. Choi, D. Bulla, B. Luther-Davies, and B. Eggleton, "Applications of highly-nonlinear chalcogenide glass devices tailored for high-speed all-optical signal processing," *IEEE Journal of Selected Topics in Quantum Electronics,* vol. 14, no. 3, pp. 529-539, 2008.

[17] E. C. Magi, L. B. Fu, H. C. Nguyen, M. R. E. Lamont, D. I. Yeom, and B. J. Eggleton, "Enhanced Kerr nonlinearity in sub-wavelength diameter As2Se3 chalcogenide fiber tapers," *Optics Express,* vol. 15, no. 16, pp. 10324-10329, 2007.

[18] R. Pant, C. Xiong, S. Madden, B. Davies, and B. Eggleton, "Investigation of all-optical analog-to-digital quantization using a chalcogenide waveguide: A step towards on-chip analog-to-digital conversion," *Optics Communications,* vol. 283, no. 10, pp. 2258-2262, 2010.

[19] A. B. Seddon, "Chalcogenide Glasses - a Review of Their Preparation, Properties and Applications," *Journal of Non-Crystalline Solids,* vol. 184, pp. 44-50, 1995.

[20] A. V. Rode, A. Zakery, M. Samoc, R. B. Charters, E. G. Gamaly, and B. Luther-Davies, "Laser-deposited As2S3 chalcogenide films for waveguide applications," *Applied Surface Science,* vol. 197, pp. 481-485, 2002.

[21] M. Bayindir, A. E. Abouraddy, J. Arnold, J. D. Joannopoulos, and Y. Fink, "Thermal-sensing fiber devices by multimaterial codrawing," *Advanced Materials,* vol. 18, no. 7, pp. 845-849, 2006.

[22] L. Brilland, F. Smektala, G. Renversez, T. Chartier, J. Troles, T. N. Nguyen, N. Traynor, and A. Monteville, “Fabrication of complex structures of Holey Fibers in chalcogenide glass,” *Optics Express,* vol. 14, no. 3, pp. 1280-1285, 2006.

[23] M. Yaman, T. Khudiyev, E. Ozgur, M. Kanik, O. Aktas, E. O. Ozgur, H. Deniz, E. Korkut, and M. Bayindir, “Arrays of indefinitely long uniform nanowires and nanotubes,” *Nature Materials*, vol. 10, no. 7, pp. 494-501, 2011.

[24] A. Abouraddy, O. Shapira, M. Bayindir, J. Arnold, F. Sorin, D. Hinczewski, J. Joannopoulos, and Y. Fink, “Large-scale optical-field measurements with geometric fibre constructs,” *Nature Materials*, vol. 5, no. 7, pp. 532-536, 2006.

[25] E. Ozgur, O. Aktas, M. Kanik, M. Yaman, and M. Bayindir, “Macroscopic assembly of indefinitely long and parallel nanowires into large area photodetection circuitry,” *Nano Letters,* vol. 12, no. 5, pp. 2483-2487, 2012.

[26] O. Aktas, E. Ozgur, O. Tobail, M. Kanik, E. Huseyinoglu, and M. Bayindir, “A new route for fabricating on-chip chalcogenide microcavity resonator arrays,” *Advanced Optical Materials*, vol. 2, no. 7, pp. 618-625, 2014.

[27] T. Khudiyev, O. Tobail, and M. Bayindir, “Tailoring self-organized nanostructured morphologies in kilometer-long polymer fiber,” *Scientific Reports*, vol. 4, 2014.

[28] D. Whang, S. Jin, Y. Wu, and C. M. Lieber, “Large-scale hierarchical organization of nanowire arrays for integrated nanosystems,” *Nano Letters,* vol. 3, no. 9, pp. 1255-1259, 2003.

[29] A. Javey, S. Nam, R. S. Friedman, H. Yan, and C. M. Lieber, “Layer-by-layer assembly of nanowires for three-dimensional, multifunctional electronics,” *Nano Letters,* vol. 7, no. 3, pp. 773-777, 2007.

[30] E. M. Freer, O. Grachev, X. F. Duan, S. Martin, and D. P. Stumbo, “High-yield self-limiting single-nanowire assembly with dielectrophoresis,” *Nature Nanotechnology*, vol. 5, no. 7, pp. 525-530, 2010.

[31] T. Khudiyev, E. Ozgur, M. Yaman, and M. Bayindir, “Structural coloring in large scale core-shell nanowires,” *Nano Letters*, vol. 11, no. 11, pp. 4661-4665, 2011.

[32] B. Gates, B. Mayers, B. Cattle, and Y. N. Xia, “Synthesis and characterization of uniform nanowires of trigonal selenium,” *Advance Functional Materials,* vol. 12, no. 3, pp. 219-227, 2002.

[33] M. A. Popescu, "Non-crystalline chalcogenides," *Kluwer Academic Publishers*, 2002.

[34] D. S. Deng, N. D. Orf, S. Danto, A. F. Abouraddy, J. D. Joannopoulos, and Y. Fink, "Processing and properties of centimeter-long, in-fiber, crystalline-selenium filaments," *Applied Physics Letters*, vol. 96, no. 2, pp. 3, 2010.
[35] A. P. Saunders, "The allotropic forms of selenium," *Journal of Physical Chemistry*, vol. 4, no. 6, pp. 423–513, 1900.
[36] K. J. Vahala, "Optical microcavities," *Nature*, vol. 424, no. 6950, pp. 839-846, 2003.
[37] L. Rayleigh, "The problem of the whispering gallery," *Philosophical Magazine*, vol. 20, pp. 1001-1004, 1910.
[38] G. Mie, "Beitrage zur optik truber medien," *Annals of Physics*, vol. 25, pp. 377-445, 1908.
[39] P. Debye, "Der lichtdruck auf kugeln von beliebigem material," *Annals of Physics*, vol. 30, pp. 57-136, 1909.
[40] R. D. Richtmyer, "Dielectric resonators," *Journal of Applied Physics*, vol. 10, pp. 391-398, 1939.
[41] L. C. M. Gastine, J. L. Dormann "Electromagnetic resonances in free dielectric spheres," *IEEEE Transactions on Microwave Theory Techniques*, vol. MTT-15, no. 12, pp. 694-700, 1967.
[42] W. K. C. G. B. Garret, and W. L. Bond, "Stimulated emission into optical whsipering gallery modes of spheres," *Physical Review*, vol. 124, pp. 1807-1809, 1961.
[43] A. Ashkin, and J. M. Dziedzic, "Observation of Optical Resonances of Dielectric Spheres by Light-Scattering," *Applied Optics*, vol. 20, no. 10, pp. 1803-1814, 1981.
[44] P. Chylek, V. Ramaswamy, A. Ashkin, and J. M. Dziedzic, "Simultaneous determination of refractive index and size of spherical dielectric particles from light scattering data," *Applied Optics*, vol. 22, no. 15, pp. 2302-7, 1983.
[45] A. Oraevsky, "Whispering-gallery waves," *Quantum Electronics*, vol. 32, no. 5, pp. 377-400, 2002.
[46] A. Matsko, and V. Ilchenko, "Optical resonators with whispering-gallery modes - Part I: Basics," *IEEE Journal of Selected Topics in Quantum Electronics*, vol. 12, no. 1, pp. 3-14, 2006.
[47] V. Ilchenko, and A. Matsko, "Optical resonators with whispering-gallery modes - Part II: Applications," *IEEE Journal of Selected Topics in Quantum Electronics*, vol. 12, no. 1, pp. 15-32, 2006.
[48] A. Chiasera, Y. Dumeige, P. Feron, M. Ferrari, Y. Jestin, G. Conti, S. Pelli, S. Soria, and G. Righini, "Spherical whispering-gallery-mode microresonators," *Laser & Photonics Reviews*, vol. 4, no. 3, pp. 457-482, 2010.

[49] T. Carmon, and K. J. Vahala, "Visible continuous emission from a silica microphotonic device by third-harmonic generation," *Nature Physics,* vol. 3, no. 6, pp. 430-435, 2007.
[50] P. Del'Haye, A. Schliesser, O. Arcizet, T. Wilken, R. Holzwarth, and T. Kippenberg, "Optical frequency comb generation from a monolithic microresonator," *Nature,* vol. 450, no. 7173, pp. 1214-1217, 2007.
[51] S. M. Spillane, T. J. Kippenberg, and K. J. Vahala, "Ultralow-threshold Raman laser using a spherical dielectric microcavity," *Nature,* vol. 415, no. 6872, pp. 621-623, 2002.
[52] F. Vollmer, S. Arnold, and D. Keng, "Single virus detection from the reactive shift of a whispering-gallery mode," *Proceedings of the National Academy of Sciences of the United States of America,* vol. 105, no. 52, pp. 20701-20704, 2008.
[53] V. Sandoghdar, F. Treussart, J. Hare, V. LefevreSeguin, J. M. Raimond, and S. Haroche, "Very low threshold whispering-gallery-mode microsphere laser," *Physical Review A,* vol. 54, no. 3, pp. R1777-R1780, 1996.
[54] T. J. Kippenberg, R. Holzwarth, and S. A. Diddams, "Microresonator-Based Optical Frequency Combs," *Science,* vol. 332, no. 6029, pp. 555-559, 2011.
[55] M. Cai, G. Hunziker, and K. Vahala, "Fiber-optic add-drop device based on a silica microsphere-whispering gallery mode system," *IEEE Photonics Technology Letters,* vol. 11, no. 6, pp. 686-687, 1999.
[56] V. B. Braginsky, M. L. Goorodetsky, and V. S. Ilchenko, "Quality-factor and nonlinear properties of optical whispering-gallery modes," *Physics Letters A,* vol. 137, no. 7-8, pp. 393-397, 1989.
[57] D. K. Armani, T. J. Kippenberg, S. M. Spillane, and K. J. Vahala, "Ultra-high-Q toroid microcavity on a chip," *Nature,* vol. 421, no. 6926, pp. 925-928, 2003.
[58] L. Zhang, Y. Wang, F. Zhang, and R. Claus, "Observation of whispering-gallery and directional resonant laser emission in ellipsoidal microcavities," *Journal of the Optical Society of America B-Optical Physics,* vol. 23, no. 9, pp. 1793-1800, 2006.
[59] J. Nockel, and A. Stone, "Ray and wave chaos in asymmetric resonant optical cavities," *Nature,* vol. 385, no. 6611, pp. 45-47, 1997.
[60] C. C. Lam, P. T. Leung, and K. Young, "Explicit asymtotic formulas for the positions , widths, and strengths of resonances im Mie scattering," *Journal of the Optical Society of America B-Optical Physics,* vol. 9, no. 9, pp. 1585-1592, 1992.

[61] M. Gorodetsky, A. Savchenkov, and V. Ilchenko, "Ultimate Q of optical microsphere resonators," *Optics Letters,* vol. 21, no. 7, pp. 453-455, 1996.
[62] J. Buck, and H. Kimble, "Optimal sizes of dielectric microspheres for cavity QED with strong coupling," *Physical Review A,* vol. 67, no. 3, 2003.
[63] V. V. Datsyuk, "Some Characteristics of Resonant Electromagnetic Modes in a Dielectric Sphere," *Applied Physics B-Photophysics and Laser Chemistry,* vol. 54, no. 2, pp. 184-187, 1992.
[64] C. L. Zou, F. J. Shu, F. W. Sun, Z. J. Gong, Z. F. Han, and G. C. Guo, "Theory of free space coupling to high-Q whispering gallery modes," *Opt. Express,* vol. 21, no. 8, pp. 9982-9995, 2013.
[65] M. L. Gorodetsky, and V. S. Ilchenko, "High-Q optical whispering-gallery microresonators - precession approach for spherical mode analysis and emission patterns with prism couplers," *Optics Communications,* vol. 113, no. 1-3, pp. 133-143, 1994.
[66] M. Gorodetsky, and V. Ilchenko, "Optical microsphere resonators: optimal coupling to high-Q whispering-gallery modes," *Journal of the Optical Society of America B-Optical Physics,* vol. 16, no. 1, pp. 147-154, 1999.
[67] Y. Panitchob, G. Murugan, M. Zervas, P. Horak, S. Berneschi, S. Pelli, G. Conti, and J. Wilkinson, "Whispering gallery mode spectra of channel waveguide coupled microspheres," *Optics Express,* vol. 16, no. 15, pp. 11066-11076, 2008.
[68] V. S. Ilchenko, X. S. Yao, and L. Maleki, "Pigtailing the high-Q microsphere cavity: a simple fiber coupler for optical whispering-gallery modes," *Optics Letters,* vol. 24, no. 11, pp. 723-725, 1999.
[69] M. Cai, O. Painter, and K. Vahala, "Observation of critical coupling in a fiber taper to a silica-microsphere whispering-gallery mode system," *Physical Review Letters,* vol. 85, no. 1, pp. 74-77, 2000.
[70] S. M. Spillane, T. J. Kippenberg, O. J. Painter, and K. J. Vahala, "Ideality in a fiber-taper-coupled microresonator system for application to cavity quantum electrodynamics," *Physical Review Letters,* vol. 91, no. 4, pp. 4, 2003.
[71] V. S. Ilchenko, A. M. Bennett, P. Santini, A. A. Savchenkov, A. B. Matsko, and L. Maleki, "Whispering gallery mode diamond resonator," *Optics Letters,* vol. 38, no. 21, pp. 4320-4323, 2013.
[72] A. Yariv, *Optical Electronics*: CBS College Publishing, 1985.
[73] M. Humphrey, E. Dale, A. Rosenberger, and D. Bandy, "Calculation of optimal fiber radius and whispering-gallery mode spectra for a fiber-coupled microsphere," *Optics Communications,* vol. 271, no. 1, pp. 124-131, 2007.

[74] J. C. Knight, G. Cheung, F. Jacques, and T. A. Birks, "Phase-matched excitation of whispering-gallery-mode resonances by a fiber taper," *Optics Letters*, vol. 22, no. 15, pp. 1129-1131, 1997.
[75] A. Yariv, "Universal relations for coupling of optical power between microresonators and dielectric waveguides," *Electronics Letters*, vol. 36, no. 4, pp. 321-322, 2000.
[76] C. Zou, Y. Yang, C. Dong, Y. Xiao, X. Wu, Z. Han, and G. Guo, "Taper-microsphere coupling with numerical calculation of coupled-mode theory," *Journal of the Optical Society of America B-Optical Physics*, vol. 25, no. 11, pp. 1895-1898, 2008.
[77] H. S. Haddock, P. M. Shankar, and R. Mutharasan, "Fabrication of biconical tapered optical fibers using hydrofluoric acid," *Material Science and Engineering B-Solid*, vol. 97, no. 1, pp. 87-93, 2003.
[78] T. A. Birks, and Y. W. Li, "The shape of fiber tapers," *Journal of Lightwave Technology*, vol. 10, no. 4, pp. 432-438, 1992.
[79] F. Orucevic, V. Lefevre-Seguin, and J. Hare, "Transmittance and near-field characterization of sub-wavelength tapered optical fibers," *Optics Express*, vol. 15, no. 21, pp. 13624-13629, 2007.
[80] S. Harun, K. Lim, C. Tio, K. Dimyati, and H. Ahmad, "Theoretical analysis and fabrication of tapered fiber," *Optik*, vol. 124, no. 6, pp. 538-543, 2013, 2013.
[81] L. Ding, C. Belacel, S. Ducci, G. Leo, and I. Favero, "Ultralow loss single-mode silica tapers manufactured by a microheater," *Applied Optics*, vol. 49, no. 13, pp. 2441-2445, 2010.
[82] G. S. Murugan, J. S. Wilkinson, and M. N. Zervas, "Optical microdiscus resonators by flattening microspheres," *Applied Physics Letters*, vol. 101, no. 7, 2012.
[83] M. Hossein-Zadeh, and K. J. Vahala, "Free ultra-high-Q microtoroid: a tool for designing photonic devices," *Optics Express*, vol. 15, no. 1, pp. 166-175, 2007.
[84] G. Elliott, D. Hewak, G. Murugan, and J. Wilkinson, "Chalcogenide glass microspheres; their production, characterization and potential," *Optics Express*, vol. 15, no. 26, pp. 17542-17553, 2007.
[85] C. Grillet, S. Bian, E. Magi, and B. Eggleton, "Fiber taper coupling to chalcogenide microsphere modes," *Applied Physics Letters*, vol. 92, no. 17, 2008.
[86] D. Broaddus, M. Foster, I. Agha, J. Robinson, M. Lipson, and A. Gaeta, "Silicon-waveguide-coupled high-Q chalcogenide microspheres," *Optics Express*, vol. 17, no. 8, pp. 5998-6003, 2009.
[87] A. Mazzei, S. Gotzinger, L. Menezes, V. Sandoghdar, and O. Benson, "Optimization of prism coupling to high-Q modes in a

microsphere resonator using a near-field probe," *Optics Communications*, vol. 250, no. 4-6, pp. 428-433, 2005.
[88] A. Watts, N. Singh, C. Poulton, E. Magi, I. Kabakova, D. Hudson, and B. Eggleton, "Photoinduced axial quantization in chalcogenide microfiber resonators," *Journal of the Optical Society of America B-Optical Physics*, vol. 30, no. 12, pp. 3249-3253, 2013.
[89] F. Luan, E. Magi, T. Gong, I. Kabakova, and B. Eggleton, "Photoinduced whispering gallery mode microcavity resonator in a chalcogenide microfiber," *Optics Letters*, vol. 36, no. 24, pp. 4761-4763, 2011.
[90] P. Wang, M. Ding, T. Lee, G. Murugan, L. Bo, Y. Semenova, Q. Wu, D. Hewak, G. Brambilla, and G. Farrell, "Packaged chalcogenide microsphere resonator with high Q-factor," *Applied Physics Letters*, vol. 102, no. 13, 2013.
[91] S. Tomotika, "On the Instability of a Cylindrical Thread of a Viscous Liquid Surrounded by Another Viscous Fluid," *Proceedings of the Royal Society of London A*, vol. 150, pp. 322-337, 1935.
[92] L. Rayleigh, "On the Capillary Phenomena of Jets," *Proceedings of Royal Society of London*, vol. 29, pp. 71, 1879.
[93] S. Shabahang, J. Kaufman, D. Deng, and A. Abouraddy, "Observation of the Plateau-Rayleigh capillary instability in multi-material optical fibers," *Applied Physics Letters*, vol. 99, no. 16, 2011.
[94] J. Kaufman, G. Tao, S. Shabahang, E. Banaei, D. Deng, X. Liang, S. Johnson, Y. Fink, and A. Abouraddy, "Structured spheres generated by an in-fibre fluid instability (vol 487, pg 463, 2012)," *Nature*, vol. 489, no. 7416, 2012.
[95] A. S. Tverjanovich, "Temperature dependence of the viscosity of chalcogenide glass-forming melts," *Glass Physics and Chemistry*, vol. 29, no. 6, pp. 532-536, 2003.
[96] C.-Y. Liu, J. He, R. Keunings, and C. Bailly, "New linearized relation for the universal viscosity-temperature behavior of polymer melts," *Macromolecules*, vol. 39, no. 25, pp. 8867-8869, 2006.
[97] X. Jiang, Y. Xiao, C. Zou, L. He, C. Dong, B. Li, Y. Li, F. Sun, L. Yang, and Q. Gong, "Highly Unidirectional Emission and Ultralow-Threshold Lasing from On-Chip Ultrahigh-Q Microcavities," *Advanced Materials*, vol. 24, no. 35, pp. OP260-OP264, 2012.
[98] C. Liu, A. Di Falco, D. Molinari, Y. Khan, B. Ooi, T. Krauss, and A. Fratalocchi, "Enhanced energy storage in chaotic optical resonators," *Nature Photonics*, vol. 7, no. 6, pp. 474-479, 2013.

[99] M. Borselli, T. Johnson, and O. Painter, "Beyond the Rayleigh scattering limit in high-Q silicon microdisks: theory and experiment," *Optics Express,* vol. 13, no. 5, pp. 1515-1530, 2005.
[100] B. Ung, and M. Skorobogatiy, "Chalcogenide microporous fibers for linear and nonlinear applications in the mid-infrared," *Optics Express,* vol. 18, no. 8, pp. 8647-8659, 2010.
[101] V. Ilchenko, M. Gorodetsky, X. Yao, and L. Maleki, "Microtorus: a high-finesse microcavity with whispering-gallery modes," *Optics Letters,* vol. 26, no. 5, pp. 256-258, 2001.
[102] S. Lacey, H. Wang, D. Foster, and J. Nockel, "Directional tunneling escape from nearly spherical optical resonators," *Physical Review Letters,* vol. 91, no. 3, 2003.
[103] J. Ballato, T. Hawkins, P. Foy, R. Stolen, B. Kokuoz, M. Ellison, C. McMillen, J. Reppert, A. Rao, M. Daw, S. Sharma, R. Shori, O. Stafsudd, R. Rice, and D. Powers, "Silicon optical fiber," *Optics Express,* vol. 16, no. 23, pp. 18675-18683, NOV 10 2008, 2008.
[104] P. Wang, T. Lee, M. Ding, A. Dhar, T. Hawkins, P. Foy, Y. Semenova, Q. Wu, J. Sahu, G. Farrell, J. Ballato, and G. Brambilla, "Germanium microsphere high-Q resonator," *Optics Letters,* vol. 37, no. 4, pp. 728-730, 2012.
[105] A. Gumennik, L. Wei, G. Lestoquoy, A. Stolyarov, X. Jia, P. Rekemeyer, M. Smith, X. Liang, B. Grena, S. Johnson, S. Gradecak, A. Abouraddy, J. Joannopoulos, and Y. Fink, "Silicon-in-silica spheres via axial thermal gradient in-fibre capillary instabilities," *Nature Communications,* vol. 4, 2013.
[106] A. Biberman, and K. Bergman, "Optical interconnection networks for high-performance computing systems," *Reports on Progress in Physics,* vol. 75, no. 4, 2012.
[107] A. Guarino, G. Poberaj, D. Rezzonico, R. Degl'Innocenti, and P. Gunter, "Electro-optically tunable microring resonators in lithium niobate," *Nature Photonics,* vol. 1, no. 7, pp. 407-410, 2007.
[108] M. Qasymeh, M. Cada, and S. Ponomarenko, "Quadratic electro-optic Kerr effect: Applications to photonic devices," *IEEE Journal of Quantum Electronics,* vol. 44, no. 7-8, pp. 740-746, 2008.
[109] H. Jung, K. Fong, C. Xiong, and H. Tang, "Electrical tuning and switching of an optical frequency comb generated in aluminum nitride microring resonators," *Optics Letters,* vol. 39, no. 1, pp. 84-87, 2014.
[110] M. Fortsch, J. Furst, C. Wittmann, D. Strekalov, A. Aiello, M. Chekhova, C. Silberhorn, G. Leuchs, and C. Marquardt, "A versatile source of single photons for quantum information processing," *Nature Communications,* vol. 4, 2013.

[111] M. Tsang, "Cavity quantum electro-optics," *Physical Review A*, vol. 81, no. 6, 2010.
[112] A. Savchenkov, V. Ilchenko, A. Matsko, and L. Maleki, "Tunable filter based on whispering gallery modes," *Electronics Letters*, vol. 39, no. 4, pp. 389-391, 2003.
[113] Q. Xu, B. Schmidt, S. Pradhan, and M. Lipson, "Micrometre-scale silicon electro-optic modulator," *Nature*, vol. 435, no. 7040, pp. 325-327, 2005.
[114] A. Savchenkov, A. Matsko, W. Liang, V. Ilchenko, D. Seidel, and L. Maleki, "Single-Sideband Electro-Optical Modulator and Tunable Microwave Photonic Receiver," *IEEE Transactions on Microwave Theory and Techniques*, vol. 58, no. 11, pp. 3167-3174, 2010.
[115] A. B. Matsko, L. Maleki, A. A. Savchenkov, and V. S. Ilchenko, "Whispering gallery mode based optoelectronic microwave oscillator," *Journal of Modern Optics*, vol. 50, no. 15-17, pp. 2523-2542, 2003.
[116] M. Izdebski, W. Kucharczyk, and R. Raab, "On relationships between electro-optic coefficients for impermeability and nonlinear electric susceptibilities," *Journal of Optics A-Pure and Applied Optics*, vol. 6, no. 4, pp. 421-424, 2004.
[117] R. Boyd, *Nonlinear Optics*, 3 ed.: Academic Press, 2007.
[118] R. del Coso, and J. Solis, "Relation between nonlinear refractive index and third-order susceptibility in absorbing media," *Journal of the Optical Society of America B-Optical Physics*, vol. 21, no. 3, pp. 640-644, 2004.
[119] K. Sasagawa, and M. Tsuchiya, "Lithium Nibate Disk Sensor Using Photonic Heterodyning," *Applied Physics Express*, vol. 2, no. 8, 2009.
[120] C. W. Rudy, A. Marandi, K. L. Vodopyanov, and R. L. Byer, "In-situ tapering of chalcogenide fiber for mid-infrared supercontinuum generation," *Journal of Visualized Experiments*, no. 75, pp. e50518, 2013.
[121] D. T. Schaafsma, J. A. Moon, J. S. Sanghera, and I. D. Aggarwal, "Fused taper infrared optical fiber couplers in chalcogenide glass," *Journal of Lightwave Technology*, vol. 15, no. 12, pp. 2242-2245, 1997.
[122] E. Lepine, Z. Y. Yang, Y. Gueguen, J. Troles, X. H. Zhang, B. Bureau, C. Boussard-Pledel, J. C. Sangleboeuf, and P. Lucas, "Optical microfabrication of tapers in low-loss chalcogenide fibers," *Journal of the Optical Society of America B-Optical Physics*, vol. 27, no. 5, pp. 966-971, 2010.

[123] C. W. Rudy, A. Marandi, K. L. Vodopyanov, and R. L. Byer, "Octave-spanning supercontinuum generation in in situ tapered As(2)S(3) fiber pumped by a thulium-doped fiber laser," *Optics Letters*, vol. 38, no. 15, pp. 2865-8, 2013.
[124] N. K. Chen, P. W. Kuan, J. J. Zhang, L. Y. Zhang, L. L. Hu, C. L. Lin, and L. M. Tong, "Multicolor upconversion emissions in Tm3+/Er3+ codoped tellurite photonic microwire between silica fiber tapers," *Optics Express*, vol. 18, no. 25, pp. 25615-25626, 2010.
[125] S. Shabahang, G. Tao, J. J. Kaufman, and A. F. Abouraddy, "Dispersion characterization of chalcogenide bulk glass, composite fibers, and robust nanotapers," *Journal of the Optical Society of America B*, vol. 30, no. 9, pp. 2498, 2013.
[126] S. Shabahang, G. Tao, M. P. Marquez, H. Hu, T. R. Ensley, P. J. Delfyett, and A. F. Abouraddy, "Nonlinear characterization of robust multimaterial chalcogenide nanotapers for infrared supercontinuum generation," *Journal of the Optical Society of America B*, vol. 31, no. 3, pp. 450, 2014.
[127] C. Baker, and M. Rochette, "Highly nonlinear hybrid AsSe-PMMA microtapers," *Optics Express*, vol. 18, no. 12, pp. 12391-12398, 2010.
[128] L. Tong, L. Hu, J. Zhang, J. Qiu, Q. Yang, J. Lou, Y. Shen, J. He, and Z. Ye, "Photonic nanowires directly drawn from bulk glasses," *Optics Express*, vol. 14, no. 1, pp. 82-87, 2006.

Appendix A

Matlab Codes

A.1. WGMs of Sphere Cavity Resonator

```
function [  ] = sphereModes_with_Lorentz_Shape(ns,na,r ,wmin,wmax)

%Calculation of WGM sphere resonances
% i radial order
% ns=index of sphere 2.797557 for TE, 2.79549 for TM
% r=radius of sphere in micron 17.9/2
% na= index of medium
% TE=1, TM=2
%format shortG
%sphereModes_with_Lorentz_Shape(2.79,1,25,1530,1548);

Qi1=1e5;
Qc1=4e4;
K1=4*Qi1*Qc1/(Qi1+Qc1)^2;
Q1=Qi1*Qc1/Qi1+Qc1;

Qi2=1e5;
Qc2=1e4;
K2=4*Qi2*Qc2/(Qi2+Qc2)^2;
Q2=Qi2*Qc2/Qi2+Qc2;
```

```
Qi3=1e5;
Qc3=3e3;
K3=4*Qi3*Qc3/(Qi3+Qc3)^2;
Q3=Qi3*Qc3/Qi3+Qc3;

w=[wmin:0.00001:wmax];
T=ones(size(w));

Ai=[2.338 4.088 5.521 6.787 7.944 9.023 10.040 11.009 11.936 12.829 13.692
    14.528 15.341 16.133 16.906];

nsxMax=ns*2*pi*r*1000/wmin;
nsxMin=ns*2*pi*r*1000/wmax;

lmin=ceil(2*pi*r*1000/wmax -0.5);
lmax=floor(2*pi*r*ns*1*1000/wmin -0.5);

n=ns/na;
wTE=zeros(1,3*(lmax-lmin+1));

P=n;%TE
%P=1/n;%TM
t=1;

%%%%%%%%%%%%%%%%%%%%%%%%%%%%%%%%%%%%%%%%%%%%%%%%%%%%%%%%%%%%%%%%%%%%%%%%%%%%
i=1;
for j=lmax:-1:lmin;
   v =j+0.5;
   nsx = v + Ai(i)*(v/2)^(1/3)- P/(n^2-1)^(1/2)...
      + 0.3*2^(-2/3)*Ai(i)^2*v^(-1/3)...
      - 2^(-1/3)*P*(n^2-2*P^2/3)*Ai(i)*v^(-2/3)/(n^2-1)^(3/2);
   if(nsx <nsxMin)
      break;
   end
```

```
    if ( nsx <nsxMax )
        x = nsx/ns;
        if(abs(nsx/ns-x)>0.5)
            warning('Size parameter mismatch!');
            break;
        end
        wTE(t)=1000*2*pi*(r)/x;
        t=t+1;
    end
end
for ii=1:1:(t-1);
    T =T - K1./((2*Q1*(wTE(ii)./w -1)).^2+1);
end
%%%%%%%%%%%%%%%%%%%%%%%%%%%%%%%%%%%%%%%
i=2;
t1=t;
for j=lmax:-1:lmin;
    v =j+0.5;
    nsx = v + Ai(i)*(v/2)^(1/3)- P/(n^2-1)^(1/2)...
        + 0.3*2^(-2/3)*Ai(i)^2*v^(-1/3)...
        - 2^(-1/3)*P*(n^2-2*P^2/3)*Ai(i)*v^(-2/3)/(n^2-1)^(3/2);
    if(nsx <nsxMin)
        break;
    end
    if ( nsx <nsxMax )
        x = nsx/ns
        if(abs(nsx/ns-x)>0.5)
            warning('Size parameter mismatch!');
            break;
        end
        wTE(t)=1000*2*pi*(r)/x;
        t=t+1;
    end
end
```

```
for ii=t1:1:(t-1);
    T =T - K2./((2*Q2*(wTE(ii)./w -1)).^2+1);
end
%%%%%%%%%%%%%%%%%%%%%%%%%%%%%%%%%%%%
i=3;
t2=t;
for j=lmax:-1:lmin;
    v =j+0.5;
    nsx = v + Ai(i)*(v/2)^(1/3)- P/(n^2-1)^(1/2)...
        + 0.3*2^(-2/3)*Ai(i)^2*v^(-1/3)...
        - 2^(-1/3)*P*(n^2-2*P^2/3)*Ai(i)*v^(-2/3)/(n^2-1)^(3/2);
    if(nsx <nsxMin)
        break;
    end
    if ( nsx <nsxMax )
        x = nsx/ns;
        if(abs(nsx/ns-x)>0.5)
            warning('Size parameter mismatch!');
            break;
        end
        wTE(t)=1000*2*pi*(r)/x;
        t=t+1;
    end
end
for ii=t2:1:(t-1);
    T =T - K3./((2*Q3*(wTE(ii)./w -1)).^2+1);
end
%%%%%%%%%%%%%%%%%%%%%%%%%%%%%%%%%%%%%%%

plot(w,T,'r');

end
```

A.2. Ray Optics Simulation in 3D Toroid Cavity

```
function [  ] = rayTorus( )
close;
clear all;
clc;

R=10*1e-6;
r=2*1e-6;

x0=R+0*r;
y0=0;
z0=0;

phi0=75;
theta0=90;

timeNum=100;

n1=2.4;
n2=1;
cos2C=1-(n2/n1)^2;

[phi,theta]=meshgrid(0:10:360);
x=(R+r*cosd(phi)).*cosd(theta);
y=(R+r*cosd(phi)).*sind(theta);
z=r*sind(phi);

m=[cosd(phi0)*sind(theta0), sind(phi0)*sind(theta0), cosd(theta0)];

index=1;
p=zeros(timeNum,3);
p(index,:)=[x0 ,y0 ,z0];
```

```
figure;
colormap(bone);

inReflection=1;

while(index <length(p) && inReflection==1)
p0=p(index,:);
k=1;
error=1;

while(k>1e-16 && error>1e-30)
   p1=p0+k*m;
   S=(p1*p1'+R^2-r^2)^2-4*R^2*(p1(1)^2+p1(2)^2);
   if(S<=0)
      p0=p1;
      error=abs(S);
   else
      k =k/2;
   end;
end;

index =index +1;
p(index,:)=p1;

N=[4*(p1*p1'-R^2-r^2)*p1(1) 4*(p1*p1'-R^2-r^2)*p1(2)
4*(p1*p1'+R^2-    r^2)*p1(3) ];
n=N/sqrt(N*N');

d=m*n';
cos2Theta1=d^2;
if(cos2Theta1<cos2C)
   m = m-2*(d)*n;

else
```

```
    a = n1*d-sqrt(n2^2-n1^2*(1-cos2Theta1));
    m = n1*m-a*n;
    index =index +1;
    p(index,:)=p1+10*m;
    inReflection=0;
end

%surfl(x,y,z);
%alpha(0.5);
surf(x,y,z,'LineStyle','none','FaceAlpha',0.6);
shading interp

hold on;
plot3(p(1:index,1),p(1:index,2),p(1:index,3),'LineWidth',1.5,'Color',[1 0 0]);
hold off;
axis equal;

pause(0.1);

end;

end
```